
NOVEL CONCEPTS IN LASER DETECTION TECHNOLOGY

MARIE AIMÉE ZANDI
Doctor of Philosophy

ASTON UNIVERSITY
June 2021

© Marie Zandi, 2021

Marie Zandi asserts their moral right to be identified as the author of this thesis. This copy of the thesis has been supplied on condition that anyone who consults it is understood to recognise that its copyright belongs to its author and that no quotation from the thesis and no information derived from it may be published without appropriate permission or acknowledgement.

Aston University

NOVEL CONCEPTS IN LASER DETECTION TECHNOLOGY

Marie Aimée Zandi

Doctor of Philosophy

2021

Thesis summary

The objective of this thesis is to design and develop a low-cost sensing device capable of detecting Continuous Wave (CW) visible lasers. As lasers are widely used and potentially harmful in military and civilian contexts, such a device would be used to both detect lasers and gather laser characteristics before proper countermeasures can be taken.

This thesis has two experimental approaches. The first approach aims at improving the field of view of an already researched technology - a modified Mach-Zehnder (MZ) interferometer - in order to extend the practicability of the system. The second approach is the design of a novel concept of laser detection with the purpose of discriminating lasers from background light and characterizing the laser wavelength.

In the case of the MZ system, a cone mirror is added to widen the initial horizontal field of view of $\pm 3^\circ$ while the additional use of a camera allows the direction of the incoming laser beam to be studied. The preliminary results demonstrate that a 360° horizontal field of view can be achieved, and that the direction of the laser beam can be determined with an estimated angular precision of $\pm 5^\circ$. The system trades sensitivity for a larger field of view with the resultant detection sensitivity equal to 70 nW (or $1 \mu\text{W}\cdot\text{cm}^{-2}$) at 635 nm.

The second system is composed of Fresnel Zone Plates (FZP) digitally written on a Digital Micromirror Device (DMD) with the use of Zernike polynomials. The polynomials are also used to correct optical aberrations inherent to the system with the use of a camera for optical feedback. Four laser wavelengths have been characterized and the system reaches a relative wavelength resolution of 10^{-3} , better than most of the detection systems using diffraction gratings. Additionally, the structure of the system creates a strong coherence difference and helps discriminate high coherent sources against low coherent sources. This technology allows for a low-cost approach for CW visible laser detection and the detection is almost instantaneous. Additionally, there are possibilities to extend the current detection system to NIR detection and pulsed lasers.

Keywords: Fresnel zone plate, digital micromirror device, coherence detection, continuous wave lasers, wavelength characterisation.

Acknowledgements

This journey would not have been possible without the help of many people around me. I am grateful for the work environment I have had and I would like to thank my supervisors, Kate and David, who were both highly supportive of my work. Kate, on whom I could always count for her help and advice on my PhD and David who was always available to answer my questions or help me in my experimental work.

This 3-year PhD is fully-funded by the Defence Science and Technology Laboratory (Dstl), an executive agency of the Ministry of Defense of the United Kingdom and I am grateful for their financial support during the last three years. I would also like to thank Sean and Rhys at Dstl for their support and for the ease of discussion with them.

I would also like to thank my colleagues, Paulami, Nasir, Karina, Yang, Namita, Mahmood, Faduma, Shirin and Gabriella. They gave me lots of comfort and laughs in the days I needed it the most.

I would also like to thank my family. Although they might not know it, I would not be the researcher I am today without them.

Finally, I would like to thank my best friend and dear partner Martti, who was present for me at every step of this PhD.

List of publications

1. M. Zandi, S. Sugden, and D.M. Benton. “Low-cost laser detection system with a 360-degree horizontal field of view”. In: *Optical Engineering* 60.2 (2021), pp. 1–11.
2. M. Zandi, D.M. Benton, and K. Sugden. “Developments in low-cost laser detection: wide field of view implementation and direction determination”. In: *Technologies for Optical Countermeasures XVI*. Vol. 11161. SPIE, 2019, pp. 145–151.
3. D.M. Benton, S. Sugden, and M. Zandi. “Coherence imaging for laser detection”. In: *Electro-Optical and Infrared Systems: Technology and Applications XVII*. Ed. by Duncan L. Hickman and Helge Bürsing. Vol. 11537. International Society for Optics and Photonics. SPIE, 2020, pp. 131–138.
4. D.M Benton, M. Zandi, and K. Sugden. “Laser detection utilizing coherence”. In: *Technologies for Optical Countermeasures XVI*. Ed. by David H. Titterton, Robert J. Grasso, and Mark A. Richardson. Vol. 11161. International Society for Optics and Photonics. SPIE, 2019, pp. 139–144.

Contents

Acronyms	9
List of Figures	10
List of Tables	14
1 Introduction	15
1.1 Thesis topic and motivation	15
1.2 Challenges and thesis objectives	16
1.3 Thesis structure	17
2 Lasers and laser detection systems	19
2.1 General theory on lasers	19
2.1.1 Laser fundamentals	19
2.1.2 Amplification of light in the medium	20
2.1.3 Characteristics of the laser output	22
2.1.4 Laser classification, danger and safety	27
2.1.5 Coherence principle - Interferences	29
2.1.6 Laser beam mechanisms	32
2.2 Applications of laser detection technology	33
2.2.1 Laser pointers	33
2.2.2 Military requirement	34
2.2.3 Optical Wireless Communication system	35
2.2.4 Laser guide star	36
2.3 Summary: requirements for our laser detection system	37
2.4 Review of existing laser detection systems	38
2.4.1 Coherent recognition	39

2.4.2	Spectral recognition	44
2.4.3	Imaging recognition	45
2.5	Discussion	49
3	Low cost laser detection system with a 360 degree azimuthal field of view	51
3.1	Background study	51
3.1.1	Field of view of existing laser detection systems	51
3.1.2	Typical coherence properties among light sources	53
3.2	Configuration of the laser detection system	53
3.2.1	Principle of detection - coherence modulation	53
3.2.2	Laser detection theory	55
3.2.3	Implementation of a wider field of view with a cone mirror	57
3.3	Experimental results	58
3.3.1	Determination of the direction of irradiation	58
3.3.2	Transmission efficiency measurements for original and cone mirror systems	60
3.3.3	Sensitivity measurements for original and cone mirror systems	61
3.3.4	Confirmation of laser detection system principle	62
3.4	Conclusion	63
4	Optical characterization and correction of a DMD based detection system	65
4.1	Background study	66
4.1.1	Basic of optical aberrations	66
4.1.2	Adaptive optics and introduction to Zernike polynomials	71
4.1.3	Fresnel Zone Plates	72
4.1.4	Modeling a FZP on a DMD	78
4.2	Analysis of DMD aberrations	83
4.2.1	Aberrations created by DMD properties	85
4.2.2	Aberrations created by DMD orientation: astigmatism	87
4.3	Experimental beam optimization	87
4.3.1	Step 1: Determination of defocus Zernike term	87
4.3.2	Step 2: determination of R5 to R15 amplitudes	88
4.3.3	Step 3: determination of R5 and R6 amplitudes	90

4.4	Results - wavelength characterization	92
4.4.1	Study of the beam waist as a function of the focal length	92
4.5	Discussion - experimental beam waist determination	95
4.6	Conclusion	96
5	Wavelength characterisation with the DMD based detection system	97
5.1	Background study	98
5.1.1	Resolution of wavelength measurement systems	98
5.1.2	Coherence properties of the DMD	99
5.2	Single channel for the DMD based laser detection system	101
5.2.1	Implementation of the single channel system	101
5.2.2	Optical characteristics of the four lasers	102
5.3	Experimental results	104
5.3.1	Beam size and defocus amplitude comparison for circular and rectangular polynomials at each laser wavelength	104
5.3.2	Evolution of beam waist with wavelength	108
5.3.3	Wavelength characterization and resolution	109
5.4	Study of different coherent sources on the DMD based detection system	112
5.4.1	Impact of the four laser spectral bandwidths in the system	112
5.4.2	Comparison between the HeNe laser and an LED around the focal point	113
5.5	Conclusion	116
6	Dynamic use of the DMD window	118
6.1	Existing multi-focal Fresnel zone plates	118
6.2	Implementation of the four Fresnel zone plate on the DMD based laser detection system	119
6.3	Experimental results	121
6.3.1	Red laser and green laser individually corrected and focused	121
6.3.2	Overlap use of red and green laser	127
6.4	Conclusion	128
7	Discussion and future work	130
7.1	Review of the research challenges and objectives	130

7.2	Future work	131
7.2.1	Field of view development	131
7.2.2	Pulsed lasers	132
7.2.3	NIR light detection	132
7.2.4	Algorithm development	133
7.2.5	Field trial	133
	References	134

Acronyms

DMD Digital Micromirror Device	2
FZP Fresnel Zone Plates	2
MZ Mach-Zehnder	2
CW Continuous Wave	2
OWC Optical Wireless Communication	35
FSO Free Space Optical	36
LWR Laser Warning Receiver	38
OPD Optical Path Difference	53
SLM Spatial Light Modulator	78

List of Figures

1.1	Evolution of the maximum output powers and wavelength diversity of laser pointers over a period of 13 years as studied in reference [3].	15
2.1	General composition of a laser system.	20
2.2	Mechanisms resulting from the interaction of light with matter.	21
2.3	Longitudinal modes of laser light.	23
2.4	Divergence of a collimated beam (exaggerated).	24
2.5	Characteristics of a laser pulse.	25
2.6	Representation of an electromagnetic wave.	26
2.7	Illustration of temporal coherence.	29
2.8	Young two-slit experiment.	31
2.9	Different mechanisms associated with laser light.	32
2.10	FAA public domain photo showing a laser pointer aimed at a cockpit at night and while taking off.	34
2.11	Composition of a Laser Warning Receiver.	38
2.12	Illustration of the Fabry Pérot interferometer.	40
2.13	Illustration of the Michelson interferometer.	41
2.14	Illustration of the Mach Zehnder interferometer.	43
3.1	Configuration of the Mach-Zehnder laser detection system.	54
3.2	a) Example of an output CW signal modulated at 1200 Hz received by the balanced photodiodes. b) Fourier transform of the signal.	55
3.3	a) Reflection principle of the cone mirror. b) Example of a beam reflected by the cone mirror.	57
3.4	Configuration of the laser detection system with the cone mirror.	58
3.5	Captured images of the cone mirror when the laser is positioned at 0° and 225°.	59

3.6	Combined data of the first harmonic amplitude and the cone mirror image for every angle spaced by 45°	60
3.7	Transmission efficiency comparison between the cone mirror and the original systems.	61
3.8	Sensitivity comparison between the cone mirror and the original systems.	62
3.9	Captures of the LED and the laser beam reflections on the cone mirror.	63
4.1	Illustration of a non aberrated wavefront passing through an imaging system that results in an aberrated wavefront.	67
4.2	Chromatic aberration: a)Longitudinal b)Lateral.	68
4.3	Primary aberrations and their mathematical terms. $2a_{20}$, $3a_{11}$, $0a_{40}$, $3a_{31}$ and $2a_{22}$ represent the coefficients of field curvature, distortion, spherical aberration, coma and astigmatism. h' is the height of the image and (r,θ) the polar coordinates of a pupil point.	70
4.4	Diffraction from a reflective grating showing the 0th and +1 order and the total optical path difference ($OPD_1 + OPD_2$).	74
4.5	Zone plates with transparent odd zones showing the first order of focus.	75
4.6	The different states of DMD mirrors: parked, on and off.	79
4.7	Laser detection system based on DMD.	80
4.8	Fresnel zone plate written on the DMD.	81
4.9	Comparison of intensity pattern with a central FZP (left) image and an offset FZP (right) for an input intensity of 1.1mW [62].	82
4.10	Evolution of the beam size as a function of the FZP focal length as reported in [60].	84
4.11	DMD interferogram in an ideal case.	85
4.12	Michelson type interferometer and phase map of DMD when turned off.	86
4.13	Interferometer and phase map of DMD when turned on.	86
4.14	Beam spots taken from the same radial distance from the DMD while the focal length is varied [62].	87
4.15	Horizontal and vertical projection of the beam length (pixel size = $4.65 \mu m$).	88
4.16	Variation of horizontal and vertical beam widths as a function of the defocus for a laser wavelength $\lambda = 632.8 \text{ nm}$	89

4.17	Amplitude of R5-R11 Zernike modes for which the intensity has been found maximum for the wavelength $\lambda = 632.8$ nm.	89
4.18	Vertical and horizontal Gaussian fit from the centre of the beam (pixel size = $4.65 \mu m$).	90
4.19	Variation of the horizontal astigmatism amplitude R5 while the vertical astigmatism amplitude R6 is fixed (left), evolution of the vertical and horizontal standard deviations as a function of the different R5/R6 pairs (right).	91
4.20	Variation of the vertical astigmatism amplitude R6 while the horizontal astigmatism amplitude R5 is fixed (left), evolution of the vertical and horizontal standard deviations as a function of the different R5/R6 pairs (right).	91
4.21	Initial beam and beam after correction at the focal point for the wavelength $\lambda = 632.8$ nm.	92
4.22	(top) Vertical and horizontal spot width as a function of the defocus value. (bottom) Average of both beam widths.	93
4.23	Average spot width as a function of the FZP focal length for a laser wavelength $\lambda = 632.8$ nm.	94
4.24	Evolution of the beam shape around the focal point at defocus values R4=22.6, 23 and 23.4.	95
5.1	Path difference between two rays across one mirror.	99
5.2	Geometry of a DMD mirror focussing light at a point P at an angle χ to the optical axis.	100
5.3	Singe channel setup for the DMD based laser detection system.	102
5.4	633 nm, 532 nm and 405 nm laser beams exiting the single mode fibre.	103
5.5	Typical spectrum of the CPS405[125] and CPS532[126] diode lasers.	103
5.6	Evolution of the beam size as a function of the defocus value for circular and rectangular polynomials at each laser wavelength.	104
5.7	Evolution of the beam size as a function of the FZP focal length for the circular and rectangular Zernike types.	105
5.8	Evolution of the beam size as a function of wavelength for the circular and rectangular Zernike types.	108

5.9	Evolution of the defocus amplitude as a function of wavelength for the circular and rectangular Zernike types.	110
5.10	Comparison of the vertical and horizontal beam widths for 4 wavelengths at 405, 533, 633 and 760 nm for the circular polynomials.	113
5.11	Evolution of the HeNe laser beam around the focal point.	114
5.12	Evolution of the LED beam at different defocus values.	115
6.1	Number positions of the four FZP on the DMD window.	120
6.2	Example of a four FZP pattern written on the DMD window.	120
6.3	(top) Four HeNe laser beams focusing on camera after correction. (bottom) Evolution of the HeNe laser beam size for each of the four FZPs with a distance DMD-camera of 9.5 cm (FZP 1, 2, 3 and 4) and evolution of the HeNe laser beam size for one single FZP on DMD with a distance DMD-camera of 46 cm (FZP on whole DMD surface).	124
6.4	(top) Four green laser beams focusing on camera after correction. (bottom) Evolution of the green laser beam size for each of the four FZPs with a distance DMD-camera of 9.5 cm (FZP 1, 2, 3 and 4) and evolution of the green laser beam size for one single FZP on DMD with a distance DMD-camera of 46 cm (FZP on whole DMD surface).	125
6.5	Two green focused laser beams and two red focused laser beams diffracted from the four FZPs pattern and the corresponding FZP number for which each beam is focusing from.	127

List of Tables

2.1	Classification of lasers based on power.	27
2.2	Classification of lasers based on the active media.	28
2.3	Impact of wavelength on the eye.	28
2.4	Categories of laser threat sources and their features.	35
2.5	Summary of past laser detection technology with their advantages and drawbacks.	49
3.1	Example of light sources and typical coherence lengths in free space.	53
4.1	Representation of circular and rectangular Zernike modes written via LabVIEW on the DMD.	73
4.2	Rectangular Zernike polynomials in polar coordinates where "a" correspond to the conversion factor from circular surface to rectangular surface, $a=0.8$ in our case, taken from reference [107].	74
5.1	Comparison of experimental and theoretical values of defocus value and beam waist with wavelengths at 405 nm, 532 nm, 632.8 nm and 760 nm for the circular and rectangular polynomials at a focal length of 46 cm.	107
5.2	Wavelength resolutions of the DMD based detection system for the circular and rectangular polynomials.	111
6.1	Comparison of experimental and theoretical values of Zernike defocus and beam waist with wavelengths at 532 nm and 632.8 nm for each FZP at a focal length of 9.5 cm.	123

Chapter 1

Introduction

1.1 Thesis topic and motivation

Low cost CW lasers pointers have been widely available for the public in the last decade or two. As such, misuses related to those lasers in aviation have grown in the UK and the US [1, 2]. Moreover, both the output power and the wavelength range of the laser pointers have been growing. Tipper in 2020 [3] highlighted this trend over a period of 13 years as illustrated in figure 1.1. The decline in maximum power in some cases is due to the sellers stopping the trade of such lasers.

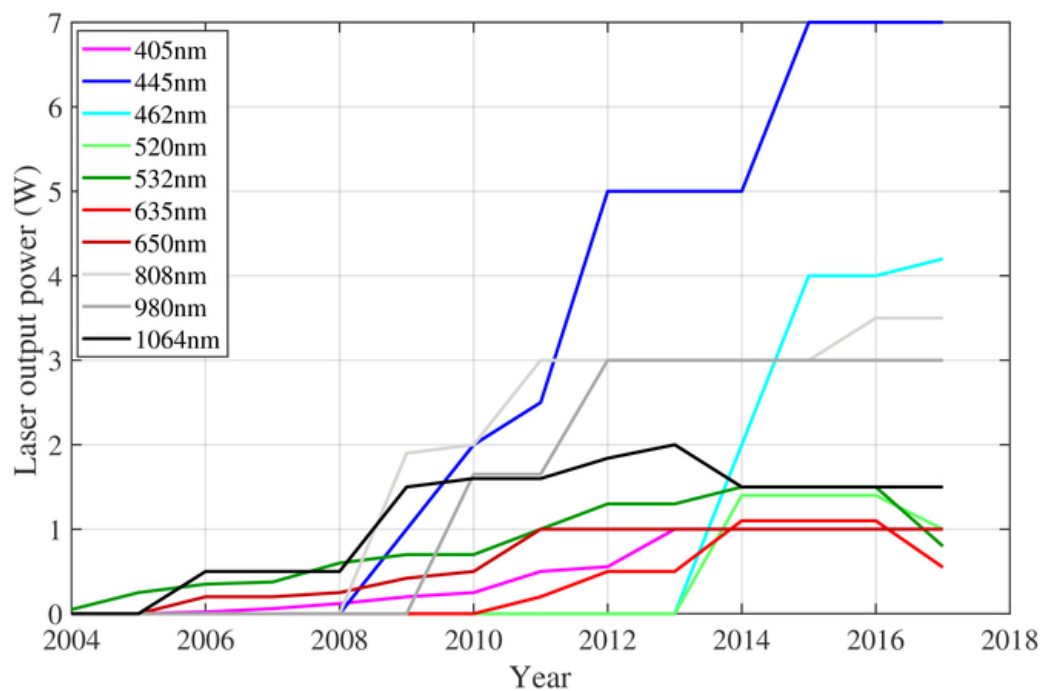


Figure 1.1: Evolution of the maximum output powers and wavelength diversity of laser pointers over a period of 13 years as studied in reference [3].

This increase in power implies a longer hazard distance for laser eye damage. Moreover, the diversity of wavelengths makes it more challenging for the detection process to include them all. As such, a laser detection system capable of detecting incident CW laser radiations and of characterising the laser parameters (wavelength, direction of irradiation etc.) would be of great interest. Moreover, in the military context, these laser detection systems are highly researched as lasers have been used for decades in the battlefield [4]. Such laser detection systems are used as warning detectors before countermeasures can be applied.

Laser detection systems generally use one of these laser properties:

- High spectral brightness: a high intensity beam in a limited spectral window.
- High coherence: precise phase properties (temporal or spatial).
- Collimated beam: low divergence of the beam throughout a large distance.

Commercially available technology, mostly used in the military setting, are focused on pulsed lasers and as such not many devices characterise the CW problem. When they do, military devices are at a high cost and/or rely mostly on an imaging or spectral recognition, i.e on the detection of intensity. Coherence recognition devices, known for their low false alert rate, are used as well, but they lack in resolution, sensitivity and wavelength range [5]. In the past years, David Benton has developed a technology based on coherence detection which uses low-cost materials. It discriminates dim laser sources against bright sunlight and can determine the laser wavelength with a precision of ± 10 nm [6, 7]. This technology brought the possibility of using coherence principle to detect CW laser at a low cost and high speed. Moreover, a laser detection system focusing on CW lasers has other applications in communication and sensing as well and as such has a high commercial interest.

1.2 Challenges and thesis objectives

This thesis is directed toward military applications. However, sometimes in this thesis, I have tried to take into account a wider view of laser detection systems as having a larger picture of the subject could give us either additional applications or additional experimental ideas. A thesis topic for a military context implies a major challenge. As military research is highly confidential, finding papers on the subject of laser detection systems can be sometimes difficult. However, many are still publicly available and will be studied in the background chapter.

The first objective of this thesis is to extend the capabilities of the coherence detection system developed by David Benton by implementing a wide field of view coverage. The initial azimuthal field of view of the system is of $\pm 3^\circ$ and is due to the small size of the optics combined with the short optical path. Many papers couldn't achieve a good sensitivity together with a wide field of view [8, 9], so the sensitivity of the system needs to be carefully studied in our experiment. The second objective is to develop a new technology using knowledge from already existing systems and to improve such system where possible. The device should be able to characterize laser wavelengths and to discriminate lasers from background light at a relatively low cost. Additionally sensitivity level, field of view coverage, wide spectral range (0.6-12 μm) and short response time (3-6 s) are other criteria to look for. The reasons for these specific criteria will be explicit in the background chapter part 2.2. The CW lasers are the laser types I am focusing on, however, the possibility to extend to pulsed lasers should be taken into account too. The final objective is the investigation of laser coherence length measurements. Oftentimes, interferometers are used for such measurements, however for longer coherence lengths this becomes more difficult. Indeed, the coherence length measurement is related to a difference of path lengths created in the system. If a laser is over 500 m in coherence length, this would imply a consequent size of the device.

1.3 Thesis structure

The body of this thesis is divided into five chapters. The first chapter is focused on the overall background of the topic of the thesis, followed by four experimental chapters. Each experimental chapter gathers its own literature review and/or background study. This thesis design was chosen to give the reader the relevant information along their reading.

The first chapter gathers the background related to laser detection systems and allows us to define the main requirements for our system. First, the principle and main characteristics of a laser will be studied. It is then followed by different applications the detection system could be used for, and the main requirements for such system will be given. Finally, the state of the art of the detection systems used in the military is discussed and compared to the requirements I have previously laid down.

The second chapter is a first approach of experimental study on a laser detection system and

uses a recent technology developed by David Benton [6]. In this chapter, I am looking at extending the field of view of the system. As such, the first part will be studying already existing field of view of laser detection systems. Moreover, the technology relies on coherent detection so some example of sources and their coherent properties will be given. Next, the principle of the technology will be explained as well as the means to extend its field of view. Finally, the results are shown and discussed.

The third chapter starts the study of a new laser detection system based on a DMD. First, a broad background study is given and includes basics of optical aberrations, Zernike polynomials and FZP and an explanation of the principle behind the system. Following this, optical aberrations of the system are characterized and then corrected using a correctional algorithm I have developed. Finally, the results of this correction are analyzed.

Once the aberrations have been characterized and corrected, the fourth chapter is focused on the characterization of laser wavelengths and for that purpose, four wavelengths are used. First, the resolution of different laser detection systems is summarized and the theoretical coherence properties of the DMD device are discussed. These properties will help us understand the results. Then, the implementation of a single channel setup is introduced to allow an equivalent input for each wavelength. The results of this new setup are then given and discussed. Finally, an experimental study of the coherence properties of the DMD is highlighted. The fifth chapter gathers the results of the final experimental chapter. The chapter studies the dynamic possibility behind the DMD window and the detection of multiple wavelengths all at once. As such, a background study of existing uses of the FZP surface is first given. Then, the new setup to allow multiple wavelength detection is explained followed by the results and their analysis.

Following the body of this thesis, a conclusion chapter is given. This conclusion chapter discusses the results of each chapter, and opens the discussion to future work.

Finally, all along this thesis a component library CC BY-NC 3.0 for Inkscape has been used for the illustration of optical setups [10].

Chapter 2

Lasers and laser detection systems

In this background and theory chapter, the basic principle of lasers is first introduced as well as their main characteristics. These characteristics will help us understand the different means to detect lasers. The second part of this chapter will introduce other possible sensing applications for which our laser detection system could be used. Finally, the state of the art on laser detection systems is discussed and where possible, a summary is given on the laser type they detect, the spectral range, the sensitivity and their field of view coverage.

2.1 General theory on lasers

2.1.1 Laser fundamentals

As the name Laser ("Light Amplification by Stimulated Emission of Radiation") suggests, a laser is an instrument used to produce light by stimulated emission. The frequencies of the resulting light can range from the infrared and the visible to the ultraviolet spectrum (other frequencies of the electromagnetic spectrum exists as well but the corresponding instrument is called a maser, m for "microwave") [11]. This section will be focused on understanding how a laser operates, defining its properties as well as the different types of lasers. I will also look at the coherence principle, fundamental knowledge for my research, and at the different light mechanisms that can be detected by the system.

Composition of a laser system

Four steps are needed to describe the creation of laser light. First, a light signal will be amplified by a group of atoms located in the laser medium. The amplified light will then be

retained in the cavity composed of two mirrors (where one has partial reflection), and will be redirected through the medium to be amplified again. At this step, the laser medium loses energy to the amplified light (mainly through the stimulated emission process). Thus, the medium needs to receive energy constantly and it will be achieved by the pumping process, associated with the light signal. Finally, the amplified light needs to be extracted from the laser cavity, and this will be done through the partially reflective mirror [12]. The precise laser wavelength is determined by the cavity length and the gain medium.

A generic diagram of an operating laser is shown in Fig. 2.1.

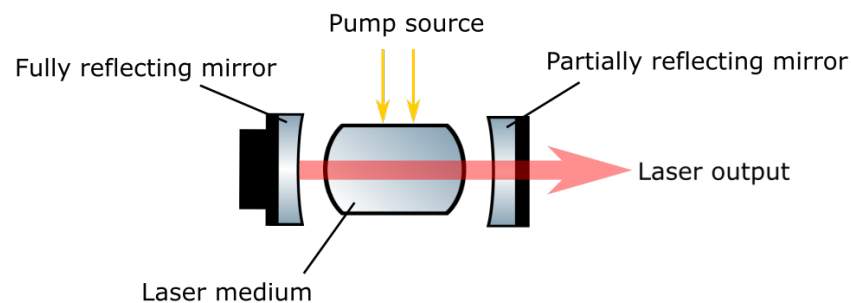


Figure 2.1: General composition of a laser system.

The application of the laser (e.g. spectroscopy, holography, medicine) determines how the choice of these three elements (laser medium, cavity and pump source) is made.

2.1.2 Amplification of light in the medium

The amplification of light in the laser medium is due to the interaction of the light with atoms and more precisely of photons with electrons.

Interaction light and matter There are three different processes that can result from this interaction photons/electrons: absorption, spontaneous emission and stimulated emission [13]. Absorption occurs when an electron from a lower level of energy reaches the upper level of energy by absorbing the energy of a photon with the right energy. The energy of the photon must be the same as the energy needed for the electron to reach the higher energy level. Then, when the electron is at an upper energy level, two processes can happen. The electron can either spontaneously emit a photon and go back to the lower energy level, this is the spontaneous emission and it always takes place in the laser medium. The energy level

difference will define the energy of the new photon:

$$\Delta E = h\nu \quad (2.1)$$

where h is the Planck constant and ν the frequency of the photon. Or the electron can be stimulated by a photon, go back to the lower energy level and create a second photon with nearly the same phase, frequency and direction as the first photon, this is the stimulated emission. The figure 2.2 illustrates these three mechanisms.

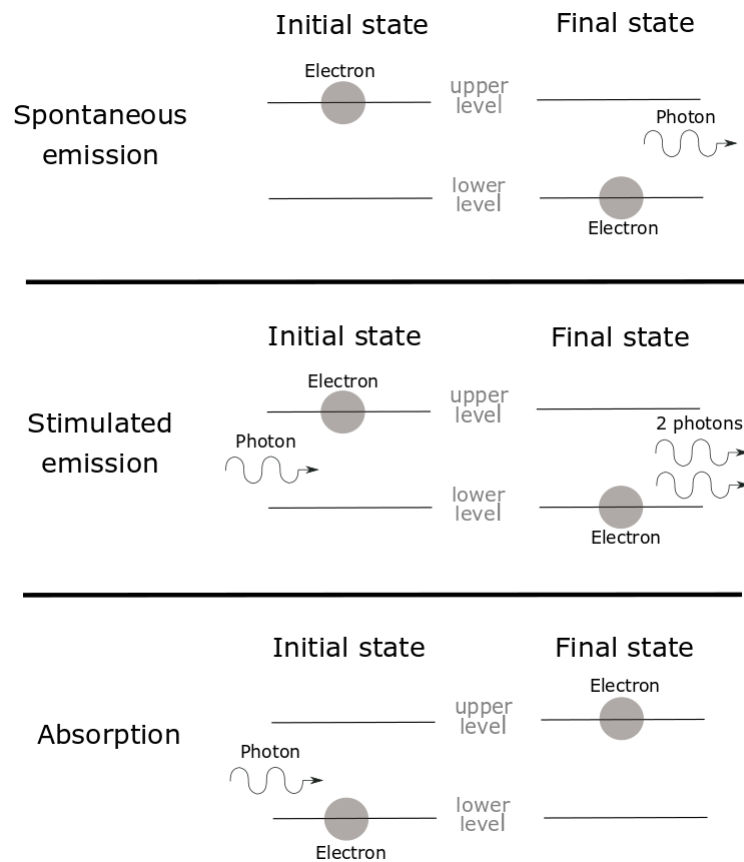


Figure 2.2: Mechanisms resulting from the interaction of light with matter.

With this knowledge, it appears that to create an amplified light in the laser medium, stimulated emission is needed (since the spontaneous emission is not controllable by its own definition). This requirement of stimulated emission implies that we would need to have most of the electrons in an excited level of energy.

Need of a population inversion However, at the normal state of matter, called thermodynamic equilibrium, the atoms are mostly in their lowest energy level, which means that the population at a lower energy level is bigger than the population at a upper energy level. So

if a photon is created from a stimulated emission, its chance to encounter an electron at a lower energy level is bigger than an electron at a higher energy level, which means that, at the thermodynamic equilibrium, absorption has more chance to occur than stimulated emission [14]. Or we need to produce stimulated emission to create our laser light, thus a population inversion needs to be created to have more electrons at the upper energy level than at the lower energy level. This is where the pump enters in action. The pumping process will add energy to the medium to keep the electrons at the upper level.

Impracticability of the two-energy levels system This pumping process is impractical with a two energy levels system because the energy of the pump has the same probability to be used for a stimulated emission than for an absorption, so the pump would only create equally populated two-levels. This problem is solved by using a three level system (or more), the middle level will serve as a transition to avoid the excited electron to go directly down to the lowest level, and thus it will create a difference in population between the first and the third levels, enough to create the population inversion needed to amplify the light [12].

Laser gain Finally, the quality of the amplification process in a laser cavity is defined by the gain G . It quantifies the amount of stimulated emission one photon can produce per unit distance. The gain is often related to the amplification factor A which measures the amplification of power through the cavity length L and is related to the gain by:

$$A = \exp(GL) \quad (2.2)$$

A refers to the ratio of output/input power.

2.1.3 Characteristics of the laser output

Now that the internal mechanism of a laser system were discussed, the characteristic properties of the laser light can be look at. This is a very important part here for my subject: these properties that characterize a laser beam can be used (and has been used) to discriminate a laser light from background light.

Wavelength Laser light is often assumed to be monochromatic. This is however not exactly true. Optical amplification occurs for a finite range of optical frequencies. The range

of frequency for which significant gain is available is called the gain bandwidth. The laser bandwidth $\Delta\lambda$ (or linewidth) of a laser is generally defined as the full width at half-maximum (FWHM) of its optical spectrum. As stated before, the wavelengths of a laser light are determined by the medium but also by the laser cavity length because only wavelengths that correspond to standing waves are supported. The optical length of the cavity L must be equal to an integral number N of half the wavelength λ :

$$L = \frac{N\lambda}{2n} \quad (2.3)$$

where n is the refractive index of the laser medium. The equation 2.3 implies that many wavelengths associated with a different integral number N could actually be possible in the laser cavity. These wavelength solutions, combined with the gain bandwidth of the laser medium will define the range of wavelengths of the output laser light. These wavelengths are the longitudinal modes of the laser (see Fig. 2.3) [14, 15].

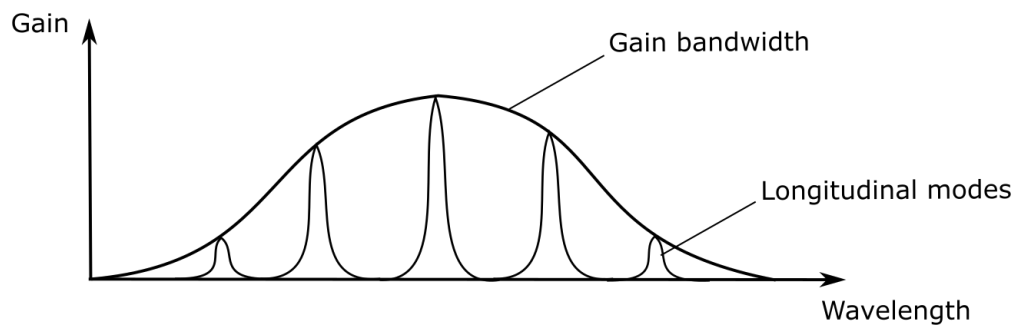


Figure 2.3: Longitudinal modes of laser light.

The final laser output will then be a product of the longitudinal modes and the gain bandwidth.

Beam divergence When the light leaves the laser system, it is known to spread into a small angle θ by diffraction, the spreading angle θ is called divergence. If we consider the laser beam as a Gaussian beam, i.e. the transverse profile of the intensity follows a Gaussian function, we can define $\omega(z)$ as the radius of the laser spot from the optical axis along the direction of propagation z , and if the mirrors in the cavity are curved, they will produce a beam waist ω_0 inside the cavity, the beam waist corresponds to the smallest $\omega(z)$. The beam waist is related

to the length L of the cavity and the laser wavelength λ by [14]:

$$\omega_0 = \sqrt{\frac{\lambda L}{2\pi}} \quad (2.4)$$

However, in real life, a laser beam is not perfectly Gaussian so often time, the divergence of the beam is defined with the beam waist by [12]:

$$\theta = M^2 \frac{\lambda}{\pi\omega_0} \quad (2.5)$$

where M^2 is the beam quality factor. The M^2 factor is the ratio of the real diffraction angle of the laser beam over the diffraction angle of the idealized Gaussian beam. The figure 2.4 illustrates the different parameters of a collimated laser beam [16].

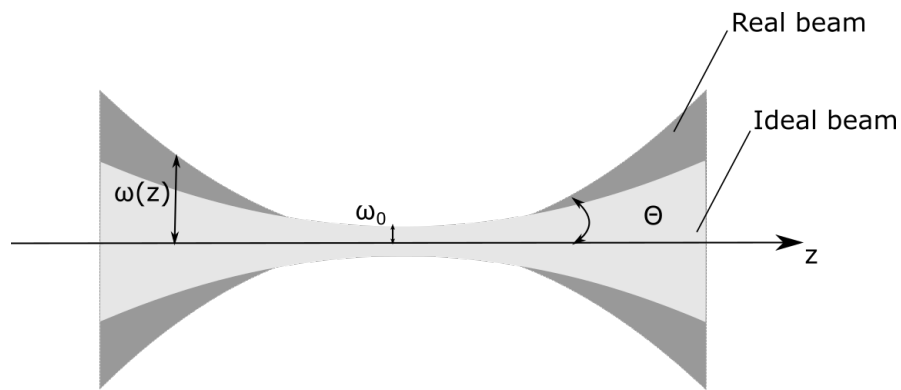


Figure 2.4: Divergence of a collimated beam (exaggerated).

The M^2 factor measures the beam quality of the laser since the divergence can vary and depends on the type of cavity, the width of the laser output and on diffraction at the borders of the laser output [14].

Laser power Laser power can refer to two different powers: the intracavity power inside the cavity and the power measured from the beam (the output power). The former is created by the stimulated emission process and the latter is only a fraction of the intracavity power that was filtered out by the partially reflective mirror limiting the cavity. It is natural then to say that the power in the cavity is much higher than in the output beam.

Four laser characteristics can influence the laser output power: the gain, the cavity, the laser medium and the pump source. Depending on the nature of these criteria, the laser output can vary from few picoWatts, milliWatts to petaWatts.

Intensity The power over a given area is in general measured in watts per unit area ($W.m^{-2}$). This quantity is defined as the irradiance, but often referred as the intensity [14]. The laser beam is known to be collimated which means that waves travel parallel to each other in the same direction with a low divergence. This allows the laser to have a well-defined beam: high intensity over long distances with small divergence.

Time of emission The time of emission varies and depends on laser applications since limiting the duration of the emission can improve the output power. Laser emission can be placed into two categories: pulsed lasers or continuous wave (CW) lasers. The CW laser has a continuous and uninterrupted beam while the pulsed laser has pulse light at a regular frequency. A pulsed laser can also be characterized by [17, 18]:

- its pulse duration τ_{pulse} : it can reach tens of attoseconds;
- the pulse's peak power P_{peak} : it is the power at the peak;
- the pulse energy E_{pulse} : it is the integral of its optical power over time;
- the pulse's repetition rate or frequency f_{pulse} : defines the number of pulses per second and is simply the inverse of the period T_{pulse} between two pulses;
- its pulse width: it is considered as the Full Width at Half Maximum (FWHM).

The figure 2.5 illustrates these different characteristics.

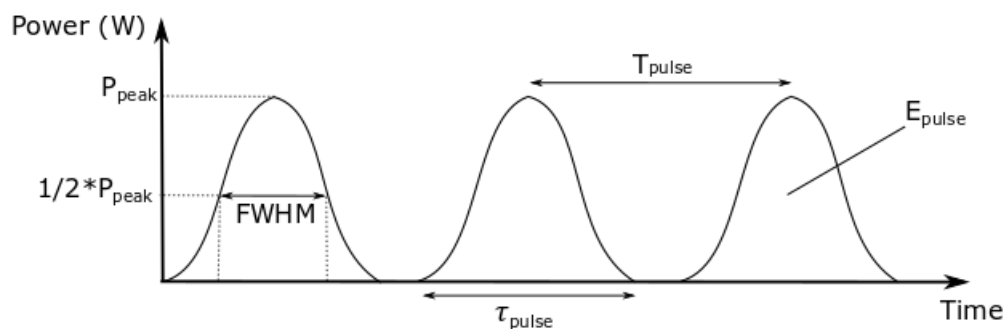


Figure 2.5: Characteristics of a laser pulse.

Coherence A unique property of lasers is the coherence. A light is coherent when the photons composing the light have a well-defined phase relationship at different locations (spatial coherence) or at different times (temporal coherence) [19]. These two different types of coherence (temporal and spatial) will be studied more in the section 2.1.5.

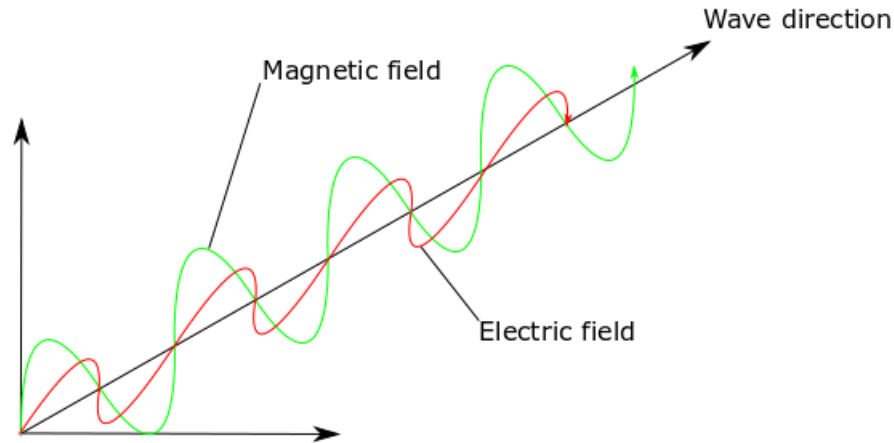


Figure 2.6: Representation of an electromagnetic wave.

Ideally, the photons exiting the laser have the same frequency and are in phase. However, in reality, the stimulated emission creates photons with slightly different wavelengths and the photons are not systematically in phase. The wavelength difference implies a frequency difference between the photons ($c = \lambda * \nu$) that will affect the quality of the coherence over long distances (they will become out of phase). The difference in phase comes from the spontaneous emission that happens at any time in the laser medium, it creates a photon with its own phase. This resulting photon can then create another cascade of stimulated emission, the new photons will have the same phase but different from the initial cascade of stimulated emission.

Between different types of lasers, two criteria will affect their coherence: the duration of laser emission and the type of gain. A high-gain laser will be less coherent than a low-gain laser because the light stays longer in the cavity for a low-gain laser. Moreover, a short pulse will be less coherent than a long pulse because a short pulse has a wider bandwidth which implies a shorter coherent length [14].

Polarisation Before talking about polarisation of light, we first need to define the light as an electromagnetic (EM) wave. Light is a superposition of electric and magnetic fields perpendicular to each other and perpendicular to the propagation direction (see Fig. 2.6). It is the phase of the horizontal and vertical components of the electric field that determines the polarization type. One type of polarization is called linear which means that the electric field oscillates in only one direction. There are two other types of polarization: circular and elliptical but there is no need to develop these two other polarizations for our study.

In a basic laser system, a laser light is unpolarized. However, often time an optical component (e.g. a Brewster plate) is added between the laser medium and one of the two mirrors to linearly polarize the light. The output power would be the same as the unpolarised light [14].

Conclusion From all these laser output properties, we can retain three that have often been used to detect lasers: coherence, beam collimation and spectral intensity. A low diverging and high intensity beam can be for example detected with a camera, however at low intensity the discrimination between the laser light and background light can be difficult and even often impossible. On the other hand, the coherence principle doesn't require a high intensity to be detected, and is very specific to a laser light so the discrimination with the background and non coherent light is easier. Using the coherence principle as a mean to detect laser seems the most adapted for our study. Nevertheless, the state of the art of the past laser detection systems will be analysed in section 2.4 and the best results among them will be discussed.

2.1.4 Laser classification, danger and safety

Laser classes Lasers are classified based on their output powers and their capacity at damaging the human body (eye or skin). The level of the damage depends on several aspects: the duration of exposure, the wavelength, the energy of the beam, and the body area exposed to the beam. Table 2.1 summarizes the different classes of laser and their potential danger[20, 21]. As can be seen from table 2.1, there exists a risk already for lasers around 1 mW and those are easily accessible in the market.

Table 2.1: Classification of lasers based on power.

Class	Power	Danger characteristics	Examples
1	Very low power	No danger during normal operation	CD players, laser printers
1M	Very low power	No danger except if use with collecting optics	Laser scanners
2	< 1 mW Waveband 400-700nm	Considered safe due to blink reflex from eye	Some laser pointers
2M	< 1 mW Waveband 400-700nm	Danger if use with magnifying optics	Laser levels
3R	1 to 5 mW	Eye damage possible from direct beam and certain specular reflections	Some targeting devices
3B	5 to 500 mW for CW lasers < 10 J/cm ² for a 0.25 s pulsed laser	Eye damage possible from brief exposure and specular reflections, skin burn possible	Research applications
4	500 mW > 10 J/cm ² for a 0.25 s pulsed laser	Eye and skin damage possible even from reflected beam	Surgery, drilling

Type of laser active media Lasers can also be classified into different categories based on the nature of the active media. The main categories are [18]: solids, gases, liquids and semi-

conductors. In table 2.2 is gathered some example of lasers, their types and their applications as reference in [22]. As shown in table 2.2, lasers are often titled by the composition of the

Table 2.2: Classification of lasers based on the active media.

Type	Example of laser	Wavelength	Example of applications
Solid-state	Nd:YAG Ti:Saph	1060 nm 650-1100 nm	Material processing, rangefinding, surgery Spectroscopy, LIDAR, multiphoton microscopy
Gas	HeNe Nitrogen	632.8 nm 337 nm	Interferometry, holography, barcode scanning Dye laser pumping, measuring air pollution
Liquid	Dye	400-1000 nm	Spectroscopy, laser medicine
Semiconductors	AlGalnP	630-900 nm	Optical disc (CD, DVD), laser pointers, machining

gain medium.

Laser hazards to living tissue As mentioned before, laser power classes are meant to rank lasers based on the danger for living tissue. Three mechanisms are responsible for these damages: thermal, acoustical and photochemical processes [23]. Thermal damage, or burn, is caused by an increase of temperature due to absorption of laser energy. The level of damage depends on the tissue type, the exposure time, the wavelength and energy of the beam. Acoustical damages are caused by mechanical shockwaves that propagate through tissue. The shockwaves are created from localized vaporization of tissue. Finally, photochemical process happens when the beam interacts with tissue cells and mostly with short-wavelength (blue or UV). Skin is usually less sensitive to laser light than the eyes. In regards to the eyes, the damage degree depends widely on the wavelength and the energy absorption [24]. It can cause damages to the cornea, the lens, or the retina. Table 2.3 summarizes the possible eye damages and the concerned wavelength range.

Table 2.3: Impact of wavelength on the eye.

Wavelengths	Location of injury	Consequences
100 - 315 nm	Cornea	Keratocojunctivitis if high doses
315 - 400 nm	Lens	Effect not immediate but next few years
400 - 1400 nm	Retina	Flash blindness or retinal burns and lesions
1400 nm - 1 mm	Cornea	Corneal burns

Among the visible wavelengths, human eye is more sensitive to green light (520–570 nm) than the other wavelengths. And on the opposite, for IR lasers, the 1500 nm is the less sensitive wavelength for the eye.

Laser safety The distance of the operator to the laser source plays an important role in the risk. For this, the Nominal Ocular Hazard Distance (NOHD) is used. It is the minimal distance from the source from which there is no risk for the operator. For example, for class 3 and class 4 lasers, this distance is very long, and the beam needs to be stop at the end of the optical system to avoid injury. Moreover, to avoid any damages to the eyes or the skin, several safe work practices need to be used. Eye protection should be used for class 3B and class 4 type lasers. For laser with potential skin damages, a full body protection is required including safety eye wear. In any case, any persons working with lasers, even low powers, need to follow training for the safe use of the materials.

2.1.5 Coherence principle - Interferences

Since the coherence principle is very specific to a laser, it is important to understand clearly this concept and to define any other physical quantities related to it. As I mentioned before, the coherence is divided into two categories: temporal and spatial. Temporal and spatial coherence are strictly independent of each other.

Temporal coherence

Temporal coherence defines the phase relationship of light emitted at different points in time [15]. The figure 2.7 illustrates the principle. A wave (green color) is analyzed at different points in time t_1 and t_2 and the phase relationship is analyzed between the two waves.

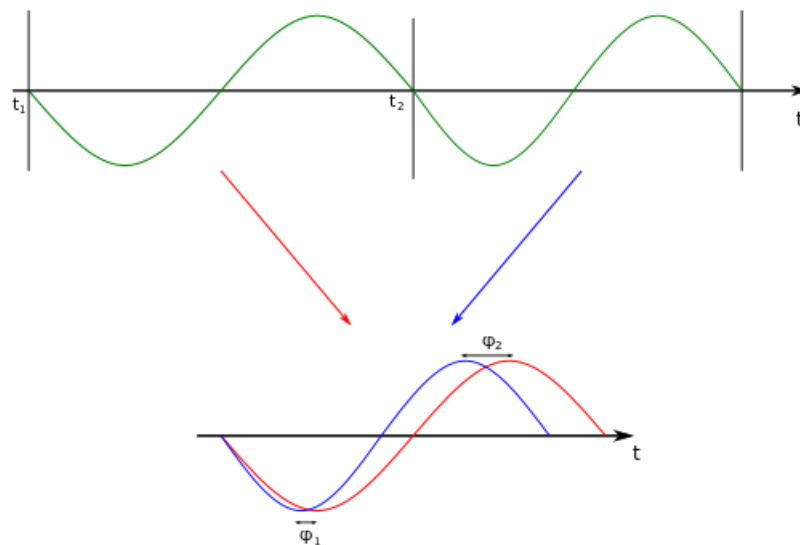


Figure 2.7: Illustration of temporal coherence.

We can see here that the phase difference is not constant in this example ($\phi_1 \neq \phi_2$), the light is said to be partially coherent. The coherence time τ_c is the characteristic time over which the phase relationship is stable. The coherence length L_c , which is the corresponding length, is related to τ_c by:

$$L_c = c \times \tau_c \quad (2.6)$$

Moreover, coherence length for a Gaussian spectral source [25] is directly related to the laser bandwidth in wavelength $\Delta\lambda$ (or in frequency $\Delta\nu$) by:

$$L_c = \sqrt{\frac{2 \ln 2}{\pi}} \frac{\lambda^2}{\Delta\lambda} = \frac{2\sqrt{\ln 2}c}{\pi\Delta\nu} \quad (2.7)$$

Where λ is the average wavelength of the light. The relationship between the linewidth $\Delta\lambda$ and the coherence length L_c implies that the temporal coherence also describes how monochromatic is a source since $\Delta\lambda$ quantifies the range of wavelengths the laser output contains. In other words, the smaller the coherent length is, the less monochromatic the light is. Every light has a coherence length: for ordinary lights, it is of few micrometers and over kilometers for some lasers.

Spatial coherence

The other type of coherence is the spatial coherence, it studies the conservation of the phase difference over the area perpendicular to the direction of propagation (cross-section of the beam). In other words, it describes how far away two sources (or two parts of the same source) can be found in the transverse direction of the observation plane and still be coherent over different observation planes [13, 26]. Spatial coherence also indicates how uniform the phase of a wavefront is. A good way to understand and to visualize the spatial coherence of a laser is to use the Young two-slit experiment as shown in the figure 2.8.

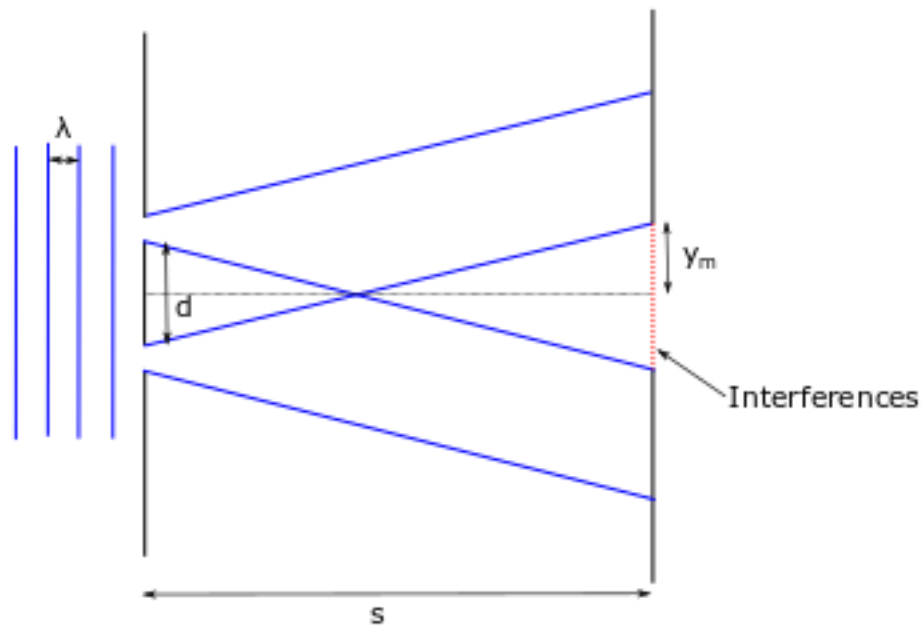


Figure 2.8: Young two-slit experiment.

One source of wavelength λ is divided by two slits in two sources. The two sources are separated by a distance d from each other in the transverse direction of the propagation and they are distanced from the observation plane by s . The two sources adds to each others at the observation plane which creates interference and the spatial coherence of the two sources is limited by a distance y_m .

Interference

When two waves are temporally or spatially coherent, they can interfere and create a specific pattern called fringes. This interference is the addition of the wave amplitudes and we observe the corresponding intensity. An interferometer is an optical device used to interfere two or more coherent light waves. The intensity distribution of the interference pattern depends on the phase difference between the two waves. Extreme cases are constructive interferences (the two signals adds to each others) or destructive interferences (the two signals subtract to each others). This difference in intensity makes it interesting to use a physical quantity to describe the quality of the created fringes. This quantity is called Visibility and is defined as follows:

$$v = \frac{I_{max} - I_{min}}{I_{max} + I_{min}} \quad (2.8)$$

where I_{max} and I_{min} are the maximum and minimum amplitudes respectively of the total intensity from the superposition of the two beams. When the visibility is between 0.5 and 1, fringes can be observed. When it is inferior to 0.2, we cannot define distinctly the fringes. The visibility is a good tool to find the coherence length of a source when associated with an interferometer such as a Michelson interferometer. The measure of the coherence length is based on the increase of the path difference created between two beams (separated from one same source) but it will be practicable only for lasers with a coherence length of no more than tens of centimeters. Longer than that, the path difference will be impracticable on a traditional optical table.

2.1.6 Laser beam mechanisms

For my interest in the laser detection technology, it is important to define the different mechanisms of light that can be created from a laser[27] and thus that I can detect with such device.

There are four mechanisms:

- Direct beam: the laser beam itself;
- Reflected radiation: reflection of the laser light from different background;
- Port scattering: detection of the light scattered at the exit port of the Laser due to scattering particles;
- Atmospheric scattering: caused by aerosol particles in the air along the beam path.

Figure 2.9 shows a representation of the four different light mechanisms.

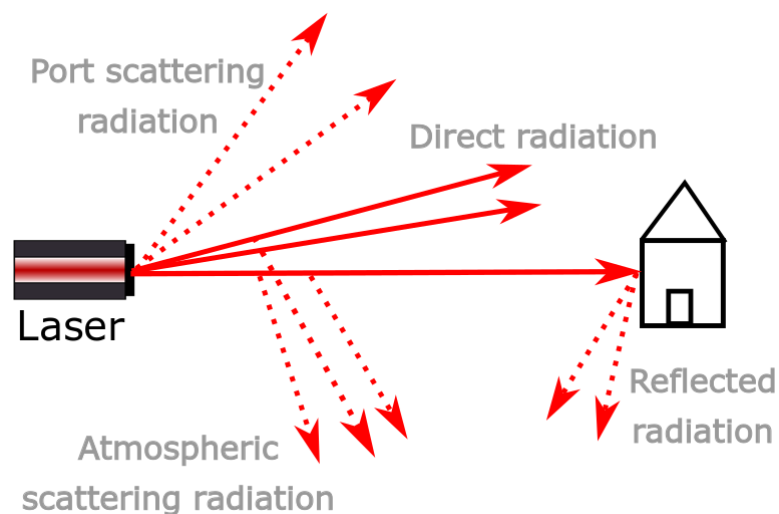


Figure 2.9: Different mechanisms associated with laser light.

Differentiating the direct beam from the indirect beams is an important criteria to keep in mind for our study, so that the laser direction can be found. The atmospheric scattering radiation can be categorised in three types: Rayleigh scattering, Mie scattering, and non-selective scattering[18]. Rayleigh scattering mostly occurs due to atmosphere gases and is created when the particles in the air are smaller in size than the wavelengths of the incident radiation. This scattering is wavelength dependant: the quantity of scattering is inversely proportional to the fourth power of the wavelength. Mie scattering is caused by particles in the lower part of the atmosphere such as pollen or dust. It occurs when the particles are larger than the wavelengths of radiation. This scattering is also wavelength dependant. Finally the non-selective scattering occurs in the lower part of the atmosphere when the particles in the air are much larger than the incident radiation. This scattering is not wavelength dependant.

2.2 Applications of laser detection technology

This section is focused on the possible applications a relatively low cost laser detection system could have in addition to the need in military. These applications ranges from indoor to space settings and a review of the requirements for an efficient laser detection system is discussed in the end of this section.

2.2.1 Laser pointers

One of the reasons detecting lasers is of interest is because of the growing abuse of laser pointers by civilians. A good example of laser pointer hazards is in aviation - the UK Civil Aviation Authority has listed all the laser incidents that happened in airports in the UK from 2009 to 2017: in 2017, 989 accidents were reported[1]. As you can see in the figure 2.10, aiming a laser pointer from the ground to an aircraft in low altitude (when taking off or landing) and at night can have terrible consequences on the field of view of the pilot. Indeed, as the eyes can take up to 30 minutes to adapt to the darkness, bright disruption from darkness to the eyes will take several seconds for the eye to adapt, and thus disturbing the vision during that time [21]. More generally, a laser pointer can seriously damage the eyes of an individual. A recent study from Linton at al. [28] showed particularly a risk for children with behavioural problems as the diagnosis may be delayed in such children.



Figure 2.10: FAA public domain photo showing a laser pointer aimed at a cockpit at night and while taking off.

The types of laser used typically have continuous and visible beams and the ones legally available for sale in the United Kingdom have a power of up to 1 mW, although higher power lasers are readily available on the internet. The corresponding laser beams can be seen over few kilometers. The most common wavelengths are green (e.g. 532 nm), blue (e.g. 473 nm) and red (e.g. 633 nm)[29].

Detecting a laser pointer directed towards an airplane or an individual, including the detection of the direction it is coming from as well as the wavelength, can help to take the appropriate countermeasures and to avoid fatal accidents or irreversible eye injuries.

2.2.2 Military requirement

Lasers in the military have many applications, we can divide them into two categories: low-power laser applications and directed-energy applications [15]. As the range of applications is wide, I will only highlight the more used and known laser applications in those two categories and for which our laser detection system will be of interest.

Low-power laser applications

Low-power laser applications are laser systems used for instrumentation and sensors. They are often associated with a threat. In the battlefield, threat using lasers is divided in four categories [27] which are detailed in table 2.4. As for the wavelength range of the LTD systems, the use of the 1.06 nm over the 1.54 nm is due to cost efficiency. For this setting, the direction (defined by the angle of arrival) of the incoming laser needs to be known, thus a 360° field of view is required. Moreover the wavelength (spectral range of laser threats are between $0.6\mu\text{m}$

Table 2.4: Categories of laser threat sources and their features.

Name of laser threat	Function	Laser type	Typical peak power (W)	Wavelength (μm)
Laser range-finders (LRF)	To measure distance laser/target	Pulsed	10^6	1.06 and 1.54
Laser target designators (LTD)	To designate a target	Pulsed	10^6	1.06
Laser beam riders (LBR)	To direct the missile to its target	CW	A few	near IR
NIR laser illumination	To illuminate target for small and close target	CW	few mW	NIR

to $12\mu\text{m}$ [4, 30]), the pulse width and the pulse repetition frequency (when pulsed laser are used) are information useful to the user, it will allow them to recognize the laser threat and take the appropriate countermeasure (like smoke screens and dazzler weapons).

Directed-energy applications

Directed-energy laser applications are mainly weapons that can inflict damage to the target. For this reason, the laser system requires high power for CW lasers and sufficient energy for pulsed laser. A good example is the laser dazzler, it is used to create vision impairments to the target, just like the laser pointer in aircraft. However, this time the power is much higher: around 500mW [15]. The wavelength range is mainly in the green spectrum (e.g. 532 nm). An example of such dazzler is the Glare LA-9/P laser dazzler developed by B.E. Meyers & Co., Inc. [31]. One other example is the Portable Laser Countermeasure System, known as the PAPV, but this time with power equal to 1.5 J at 1.06 micron and 0.2 J at 0.53 micron.

2.2.3 Optical Wireless Communication system

Optical Wireless Communication (OWC) systems are systems using optical waves to transmit data, instead of the normal radio frequencies (mainly because the radio frequency spectrum is limited and over crowded). There are two categories of OWC: indoor system and space system.

Indoor systems

Indoor OWC systems includes all communication within a building. One good example of use of lasers in indoor systems comes from coherent optical communication. Coherent optical communication use what is called line-of-sight (LOS) transmission (emitter and receiver needs to be in view of each other) and diffuse transmission (transmits in all directions and reflects

from background objects) [32, 33]. Where it is interesting for us is that coherent transmission is based on the comparison between a phase and/or frequency modulated optical signal and a local oscillator (e.g. laser; see heterodyne and homodyne technique) [34] which directly relies on the coherence of the light. The wavelength range used is visible or infrared light, from 400 nm to 1600 nm.

Free space optical systems

Free Space Optical (FSO) communication systems apply to outdoor systems. There are many applications including ground-to-satellite links and inter-satellite communications [35]. I present one good example where the laser system technology could apply. Compared to radiowave communication, an inter-satellite laser communication is preferred as the RF spectrum availability is becoming limited due to its large use in space [36, 37]. One of the technologies to make this communication is the N-slit interferometer [38]: the interferometer combined with a visible laser light can generate a series of optical signals representing letters. These signals are unique and thus if they were intercepted optically, they would be modified and it would systematically be noticed in the interference pattern. This is why this technology is used to secure data transmission between satellites. It can also be used to detect air turbulence in airfields [39]. A laser detection system would be very interesting here if we combined a diffraction pattern with a CCD camera to look at the interference pattern. The wavelength here belongs to the visible and short IR spectrum (from 380 nm to 3000 nm). The needed power of the laser depends on the distance between the satellites but can be as low as few tens of milliwatts [35]. Moreover, concerning eye safety, a laser at 1500 nm could be used at higher power (10 times higher) than for a shorter wavelengths at for example 750 nm since the outer layer of the eye, the cornea, absorbs the light energy at 1550 nm and prevents it from focusing on the retina, where the danger would be.

2.2.4 Laser guide star

Another application of laser in space is the laser guide star. A guide star is used to correct the effect of atmospheric turbulence on an image taken through a telescope on Earth. The passage of light through the Earth's atmosphere results in a wavefront distortion. A laser is used as a reference light source and together with a deformable mirror, they are able to correct the wavefront (as explained in part 13.7.2 of reference [15]). Here, a laser detection

system technology could be useful if combined with a deformable mirror to reconstruct the wavefront. To go through the atmosphere and back, the laser needs to be powerful: 20-50W, but will be greatly attenuated on the way back to earth. The wavelength range depends on whether the guide star is a sodium beacon or a Rayleigh type: short wavelengths for the Rayleigh guide star (down to 350nm) and 589.2 nm for the sodium beacon guide star. Pulsed lasers are preferred for the Rayleigh type while continuous lasers are more often used for the sodium beacon type.

2.3 Summary: requirements for our laser detection system

As seen previously, many applications can be found for the use of a low-cost laser detection. Having a wide enough field of view seems to be required for most of the applications: the larger the field of view is, the more cost-effective the technology will be. However, the signal-to-noise ratio cannot be affected too much by a wide field of view for this to work: the sensitivity of our system needs to be taken into account as well. Moreover, the laser light seems to range from visible to near-infrared so we have a bandwidth requirement from $0.38\mu\text{m}$ to $12\mu\text{m}$ and being able to measure the laser wavelength would be a great advantage. The power can actually be quite big, over hundreds of milliwatts and in that case a commonly used photodiode would be easily saturated and I need to take this into consideration for this technology. It is also important that in the other case where the laser power detected is weak, our system is able to detect it. A detection range of 10 km should also be considered and this will impact mainly the detection of laser target designators and beam riders [5]. Both pulsed and continuous lasers are used so I should consider the detection of these two types as well as the determination of the pulse width and the pulse repetition frequency when pulsed lasers are used. Furthermore, regarding the laser threat especially, a short response time is required, between 3-6 s to activate the countermeasure, so the nature of the processing unit needs to be taken into account. Finally, the power of lasers especially in the military should be considered and the level resistance of the detectors should be established when possible.

2.4 Review of existing laser detection systems

From the last 40 years, many patents and scientific papers have been published introducing new technologies to detect lasers and to define the laser radiation parameters such as the laser frequency, the pulse duration, the pulse frequency, the power and the direction of the beam. These laser detection technologies are known as Laser Warning Receiver (LWR) in the military and they are often composed of three parts: an optical unit, a detection unit, and a processing unit [40] as illustrated in figure 2.11. In these laser detection systems, the optical unit will direct and/or modify the incident beam towards the detection unit. Then, a digital signal will be created from the optical signal in the detection unit. From this digital signal, the characteristic of the laser will be given by the processing unit.

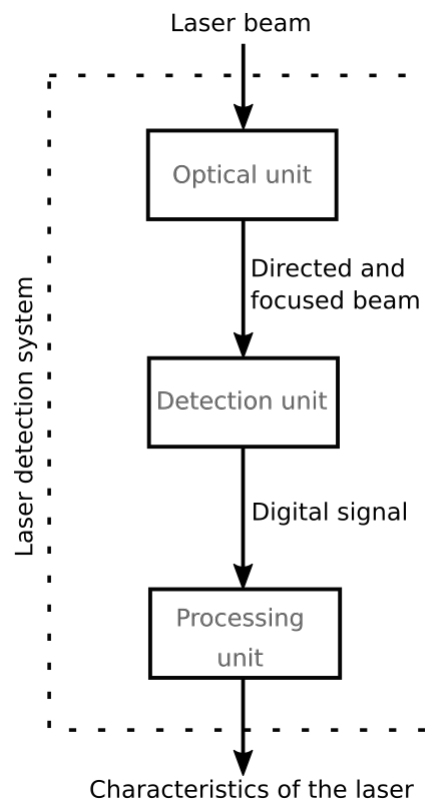


Figure 2.11: Composition of a Laser Warning Receiver.

The processing unit should contain all the signatures of possible optical signals on the battlefield, this includes lasers sources and interferences. The composition of the optical unit and sometimes the detection unit depend on the laser characteristic used in the technology to discriminate the laser from the background light. To classify laser warning receivers, Wang in 2014 separated the technologies in three categories based on the observed light characteristics: coherent recognition, scattering recognition and spectrum recognition [41]. While Benton

in 2019 [42] separated them based on the discrimination technique: coherence, imaging and spectral. I will here follow Benton's classification as the discrimination of laser light from interference is one of the main criteria for our system, these categories will give us a clear idea on which technologies will be of interest for us. In these three categories, coherent recognition systems are systems using the temporal coherence of a laser light to discriminate it from the background light, it includes amplitude splitting interferometers such as Michelson, Fabry-Perot, Mach-Zehnder and Fizeau interferometers. Imaging systems use the low divergence and high brightness properties of a laser beam and includes technologies using CCD cameras or photodiodes. Spectral discrimination systems will also discriminate based on the brightness of the beam but this time use the laser monochromatic properties by incorporating diffraction grating in their systems.

In this section, I will look at the different papers on those technologies and for my interest, I will highlight the type of laser all the technologies can detect, the spectral range, the sensitivity of the system and when it is included, their method for a wide field of view coverage. The relative uncertainty (equal to absolute error over real value) of the wavelength measurement for the different technology is also included. Drawbacks and advantages of the different technologies are also discussed.

2.4.1 Coherent recognition

Amplitude splitting method is based on the analysis of fringe interferences created at the end of the interferometer. An interferometer can be used in two modes: static or dynamic. Static interferometers have a constant path difference while dynamic interferometers have a continuous and uniform change of the path difference, they are often called scanning interferometers [43]. In this part, I will focus the study of laser detection into 4 interferometers, the most used in the field: Michelson, Mach-Zehnder, Fizeau and Fabry-Perot interferometers.

Fabry-Pérot etalon

A Fabry-Pérot etalon is composed of two partially reflecting mirrors parallel to each other and separated with a specific distance (from micrometers to centimetres apart). The figure 2.12 illustrates the interferometer.

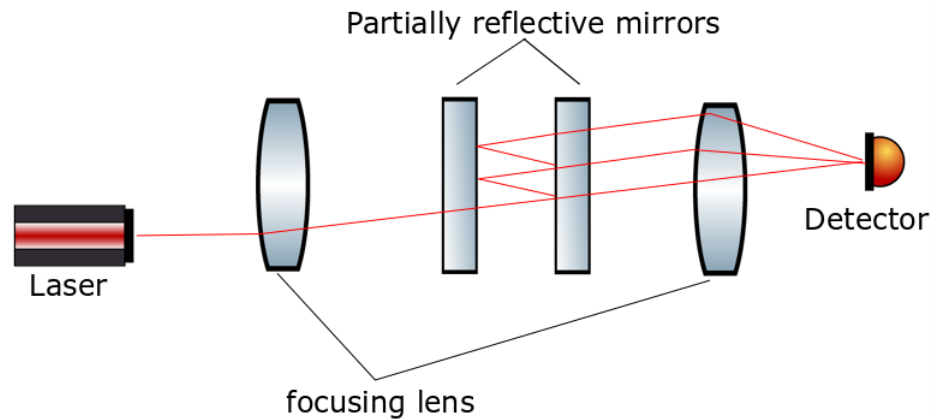


Figure 2.12: Illustration of the Fabry Pérot interferometer.

The distance between the two mirrors is normally fixed and depends on the wavelength I need to detect: only this wavelength will create interference fringes at the output of the interferometer. Moreover, a minimum space between the two mirrors of few micrometers is enough to discriminate the background light due to the short coherence length of this light.

One of the first papers to introduce a Fabry Pérot interferometer for the detection of lasers was Robert Crane Jr. in 1979 [44]. He used an angle-scanned Fabry-Pérot interferometer as a coherent modulator: by scanning across a scene (field of view of 90°), it modulates only input coherent light (from pulse laser and CW laser) and does not modulate incoherent light. The scan is done by angularly and continuously moving the etalon on the axis perpendicular to its optical axis which changes the thickness of the etalon and allows a range of frequency to be detected [45]. The source direction and the laser wavelength can be found by looking at the transmittance pattern, however the wavelength detection is restricted to a short spectral band imposed by the scan process (example: $0.45\text{-}1.1\mu\text{m}$, $2\text{-}4\mu\text{m}$ and $5\text{-}12\mu\text{m}$). Following Crane, Siebert Edward T. [46] used a multi-stepped etalon: a static Fabry-Perot with several regions of different thicknesses. The system was able to have a field of view of up to 160° and the wavelength detection was limited only by the detection range of the detectors. So, unlike Crane, this technology doesn't have limited spectral band but it is necessary to know beforehand the laser wavelengths to be detected, which is a big drawback for the desired technology. In 1986, another dynamic Fabry Perot interferometer type has been used [47]. The optical path length is changed by applying a sound wave to the etalon which allows only a specific spectral range to be detected. Manasson and Sadovnik used an interferometer in 1996 made from electro-optical crystal [48] to modulate coherent light at a specific frequency. It allows the detection of pulsed and CW laser in a wide spectral range. However, here

again, the thickness of the etalon is previously fixed from an "expected" laser threat, thus the wavelength range is not immediately long enough for our case ($0.6\text{-}12\mu\text{m}$).

In conclusion, Fabry-Perot etalons succeed very well in discriminating lasers from background light, even from low intensity lasers and for both CW and pulsed lasers. They can achieve an acceptable field of view of 160° and a high sensitivity. The interferometer can reach a relative uncertainty of 2×10^{-9} for the determination of the wavelength [49]. However, the physics of a Fabry-Perot etalon makes it impossible to have the whole wavelength band I am looking for ($0.6\text{-}12 \mu\text{m}$) - only short bands are possible.

Michelson interferometer

A Michelson interferometer is composed of one beam splitter that will split the incoming beam between two paths, called arms. One beam will go to a movable mirror, the other to a fixed mirror. Depending on the location of the movable mirror (i.e. the path difference between the two arms), the interference will change.

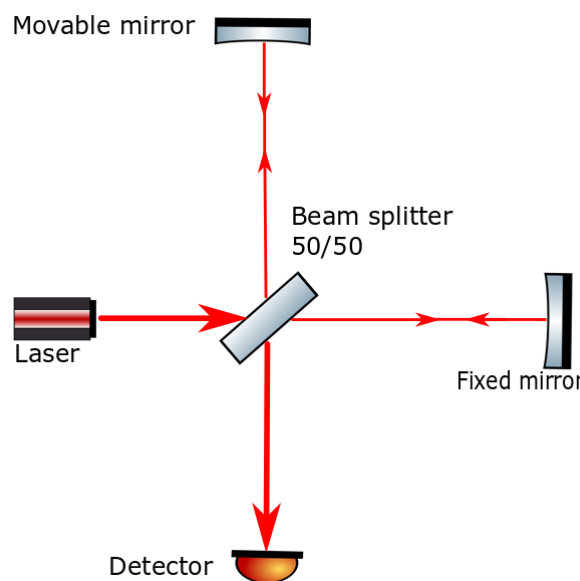


Figure 2.13: Illustration of the Michelson interferometer.

In 1988, Hickman and Duffy introduced a laser detection system with a scanning Michelson interferometer [50, 51]. Their idea is to modulate one of the mirrors with a piezoelectric transducer to induce a modulation on the path difference in the region where the background light doesn't interfere anymore (it is the case after few μm of path difference). Thus, only light with a longer coherence length, such as lasers, will be modulated and at the modulation frequency of the transducer. They combined this with a Fast Fourier transform stage to an-

alyze the modulated signal output [51]. They also modified the Michelson interferometer to have access to two output channels (instead of one channel) and thus they were able to use the other output with a CCD camera to obtain the position, shape and size of the coherent incoming signal. Their technique is very efficient in discriminating laser light from background light. However, they did not look at determining the wavelength in their research and their technology require additional electronic processing to obtain a good sensitivity. In the following year, Sutton uses a twin Michelson interferometer: two different path differences are made in the same interferometer by introducing a piece of glass as a delay on the lower part of the beam [52]. Their interferometer is also composed of a scanning arm (use of a phase modulator) to measure the fringe profile of the two interferometers. By comparing the two fringe profiles and knowing the two path differences, the coherence length of the source can be measured. Moreover, his technology is associated with a bandpass coherence processing that rejects signals outside the coherence length range of 0.13-0.17mm by using a diffraction grating monochromator. The exit of the monochromator was chosen to filter only the desired wavelengths. This technology has a field of view of only 0.06° due to the size of the optical components (1-2cm). It achieves an accuracy of the coherence length measurement of 10%. However, this can be increased by using a modulation frequency in excess of 10kHz (400Hz in his experiment). In 1999, Coutinho et al. used a scanning Michelson interferometer with a piezoelectric driver and compare a reference path difference of a white incoherent light with a path difference where they superpose a laser to the white light [53]. The difference in phase, in amplitude and in frequency along the two path differences allow them to discriminate the laser light with a good signal to noise ratio and with low-cost materials. However, the signal needs a lot of digital processing before obtaining the results and no wavelength determination has been achieved. In 2007, a static Michelson interferometer was used but this time with one of the mirror slightly tilted which create vertical interference fringes (instead of circular fringes) [54]. The interferometer is associated with a Fourier transform lens and an array of CCDs to analyze the interference. For a wide field of view coverage, they used an optical antenna composed of two lenses (the two are plano-convex) and a fibre optic bundle. In their experiment, the system was able to give a field of view of 45° but with a possibility to increase it by changing the refractive index of the fibre or its numerical aperture.

To summarize these different papers, a Michelson interferometer when in a scanning mode has really good results in discriminating lasers from background light but needs a lot of signal

processing. The Michelson interferometer can reach a relative uncertainty of 6.4×10^{-9} [55] for the determination of the wavelength. It is able to detect a wide spectral band and include both type of lasers (CW and pulsed). The optical antenna in the last paragraph seemed an efficient way to improve the field of view.

Other interferometers

Other types of interferometers used in laser warning devices are MZ and Fizeau interferometer. Mach Zehnder interferometers are very similar to Michelson interferometers. The figure 2.14 illustrates the MZ interferometer principle.

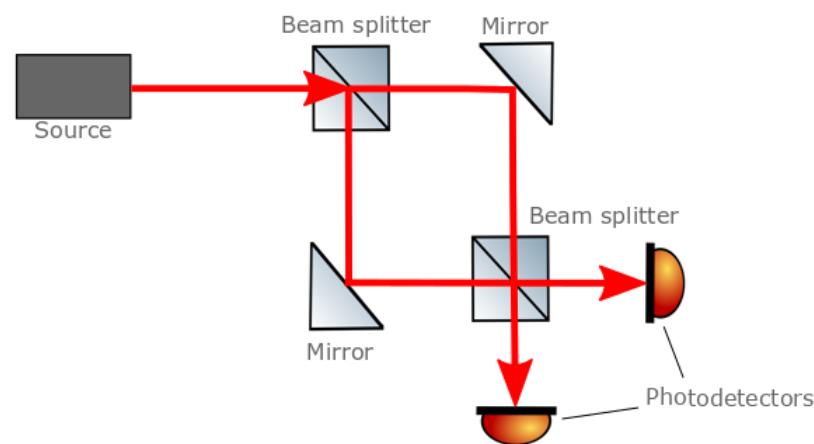


Figure 2.14: Illustration of the Mach Zehnder interferometer.

The main difference between these two interferometers is the number of outputs available without any modification of the system: two outputs for Mach Zehnder interferometer and one output for Michelson interferometer.

Benton in 2017 [6] used photodiodes with a scanning Mach-Zehnder interferometer for a low-cost laser warning system. The scanning interferometer is composed of a modulating piezo mirror replacing one of the two mirrors. The idea is related to the scanning Michelson interferometer from [50, 51] where only the coherent light is modulated. Benton's interferometer proves to be efficient at detecting continuous lasers at low intensities. He is able to detect a laser beam down to 1nW. He also introduces a method to determine the laser wavelength by changing the modulation amplitude and looking at the ratio of the fundamental harmonic over the third harmonics. However, the third harmonics is not always strong enough to be detected and thus this wavelength determination method shows inconclusive results. For the Fizeau type, in 2000, a wedge etalon has been used [8] combined with two types of Fourier

transform analysis (electronic and optical). This time the two mirrors of the interferometer are not parallel but one of the two mirrors has a small angle. It allows constructive interferences at several locations and create intensity spikes along the other mirror length. The use of a Fourier transform lens improves the sensitivity (signal to noise ratio) in comparison to an electronic Fourier transform but in consequence the lens imposes a field of view of $\pm 60^\circ$ from the normal.

2.4.2 Spectral recognition

Spectral recognition systems look at a narrow spectral band and use generally diffraction grating combined with a detector array. The use of diffraction gratings in laser detection systems started 20 years ago. A diffraction grating is an optical component composed of reflecting elements (reflection grating) or transmitting elements (transmission grating). It can split the light into its different wavelengths and the distance between the reflecting (or transmitting) elements tells us the angle at which the different radiations will be diffracted based on the grating equation [56]. Those gratings are notably efficient at differentiating the incidence laser from any optical interference.

In 2006, Zhang et al. [57] used a horizontal grating combined with a CCD sensor to measure the wavelength with an optical spectral range from 500 nm to 1100 nm (accuracy 10 nm; without restriction on the wavelength range) and the incident angle of pulsed lasers with a field of view of 22.5° (accuracy 1°). It is then followed in 2009 by McAulay with the same type of grating [9], he explains that although this method is very efficient to find the wavelength and the direction of the laser, the sensitivity is quite limited when the light has low intensity. The idea is then to separate the estimation of wavelength and direction into two different tasks which will then require two almost identical laser warning receivers. Another paper from 2009 [58] explains the process of calculating the wavelength and angle of arrival with again an horizontal grating. The intensity of the diffraction pattern of the laser will be composed of two stripes formed on the CCD camera at two specific locations and the wavelength and angle of arrival can be deduced from the locations on the camera. There is no restriction on the type of lasers (pulse or CW) and they obtained a wavelength resolution of 10 nm. The drawback here could be the size of the camera (56 x 60 x 39.4 mm) if I am looking for a smaller detector size. Wang et al. were focused then on the development and improvement of the field of view with a fish eye lens in 2013 and 2014 [41]. The new field of

view is of 160° (accuracy of 2° before 140°) and wavelengths of pulsed and CW laser can be determined with an accuracy of 40nm. Although the wide field of view is very promising, the accuracy on the wavelength needs to be improved. Another form of diffraction grating is the Digital Micromirror Device (DMD) which consists of a few centimeters rectangular array of micro-mirrors of around 15 micrometers each. The mirrors can be individually addressed and be tilted by $10\text{-}12^\circ$ and thus the DMD has diffractive properties [59]. In 2014, Partanen et al. [60] used a DMD to create a Young's double slit experiment and measured the spatial coherence function (amplitude and phase) of the beam as well as the beam intensity with the help of a CMOS camera. The system is fast and low-cost and has a wide field of view (over 90°). More recently, Mohagheghian et al. used the DMD to create a Fresnel Zone plate (FZP) to determine laser wavelength [61]. A FZP is composed of transparent and opaque rings where each ring radius is proportional to the wavelength and the focal point of the diffracted light. Mohagheghian et al. use these properties and modify the ring radius (and thus the focal point) and they look at the laser beam spot size resulting from the diffraction with a CCD camera. They reach a relative uncertainty in the wavelength determination of 10^{-5} . They however notice strong astigmatism in the beam spot profile which can affect the accuracy. Benton proposes in 2018 [62] a method to avoid astigmatism on the focal point by using an approach similar to the use of Zernike polynomials.

To summarize these papers on diffraction grating technology, the main advantage is a wide and quite accurate field of view determination combined with the measurement of wavelength for both pulsed and CW lasers. However, the wavelength determination has some drawbacks for low intensities and it is not accurate enough when the horizontal grating or the double-slit experiment are used (accuracy 10nm). Unlike those diffraction gratings, the use of FZP have seen promising results in determining and improving the wavelength determination in a fast and low-cost way using a DMD.

2.4.3 Imaging recognition

Imaging recognition systems regroup all the systems using the low divergent and high brightness of the laser beam. Two-sub categories are often used in laser warning receivers: photodetectors based systems and camera based systems. A third separated categories can be added to these technologies, it is also using imaging systems but is targeting scattered light. This can be of interest for a future complete detection of laser light on the battlefield.

Photodetectors based system

This section summarises laser detection systems based on photodetectors [63, 64].

A patent from 1995 uses a position sensitive photodetector which can define the position of an illuminated spot on the detector [65]. They combine this position detector with a dome reflector to focus the beam on the detector. Their technology allows a 360° field of view and gives the direction of the incoming laser light. Their method to detect wavelength is to use one filter to block unwanted radiation and use several detectors for other wavelengths. In 2011, a technology using an array of photodiodes combined with a converging lens was able to obtain a field of view of 90° (accuracy of $\pm 3^\circ$) in azimuth and 35° in elevation [66]. A 5cm aperture for the lens is needed to collect enough intensity from a low intensity laser or for a far distance laser (typical 500m). The use of two photodiodes (Silicon and InGaAs) mounted with an amplifier and a processing unit have been introduced to extend the spectral range to 400-1700nm [67]. Their technology also discriminated a direct beam from a reflected laser beam based on the density powers of known laser receivers. They have however not being able to determine the laser wavelength. To improve the laser warning receiver technology in harsh environment and to decrease the false alarm rate, El-Sherif et al. used the fact that high power pulsed lasers (rangefinders) create photoacoustic waves on solid surfaces [68]. Although very young, their technique has proven effective and reduced the false alarm rate by 4. Moreover, the protective material used is low-cost. A new technology from 2017 uses a set of photosensitive linear arrays to detect lasers for a 360° field of view and thus reducing the size of the detector system [69]. To achieve this, the wavelength range has to be reduced and can only detect two wavelengths. This technology is used for specific purposes and does not satisfy our requirement as our optimal range of wavelength detection is wide (from 0.38 μm to 12 μm). Very recently, in the beginning of 2018 a new technology has been proposed using optical array associated with photosensors [40]. The device has a very good signal to noise ratio even from far distances and hazy conditions for three wavelengths (0.63 μm , 1.06 μm and 1.54 μm) with the possibility to extend the range from 0.62 μm to 1.54 μm . However, the field of view is of 20° and needs to be improved for our purpose.

In summary, the detection of spectrum with a non-imaging system combined with a good processing unit is good to discriminate direct beams from reflected beams and typically the technology has a good field of view. However, the determination of multiple wavelengths is

restricted to the amount of photodiodes used and discriminating the laser light from other light is not guaranteed to succeed if only the high intensity of the power is considered.

Camera based systems

Imaging Laser Detection System (ILDS) are usually composed of a fish-eye lens and CCD/CMOS camera devices [70]. They are able to detect both CW and pulsed lasers and by analyzing the images, they can find the laser pulsed rates. The following papers introduce new way to improve ILDS issues (saturation, dynamic range etc.).

In 2010, Zhou and Ying based their research on improving image processing software algorithms to enhance the dynamic range [71]. They reached a 30% improvement which consumes more time (around 2 seconds) but allow detection of lower intensity beams. The same year and to correct this time the locating error of a laser spot on a CMOS camera, Ying et al. have developed a model based on Monte Carlo analysis [72]. This model predicts the spot energy location on non-light sensitive area of the camera (between the pixels). To avoid saturation of the imaging sensor by the laser beam, the BRILLIANT system has been developed [27]. It works by controlling the gate of a camera and synchronizing it with the incoming laser pulses. Two papers from 2006 [73] and 2009 [74] have their systems based on a multispectral detector available on the market. This detector is able to detect laser light from pulsed laser (high and middle power), to determine the direction of the light as well as the time between the observation of the laser light and the present. However, the detector has only a short spectral band ($0.5\text{-}1.8\mu\text{m}$, $2\text{-}5\mu\text{m}$ or $5\text{-}12\mu\text{m}$). The first paper fixed this problem by duplicating the detector in four places while the paper from 2009 used an off-axis system composed of mirrors to have only one detector head. More recently, Tipper et al. use a defocused camera with ND filters to discriminate laser based on the beam size on camera [3]. The ND filters act also as a filter for background light, they achieved an overall good sensitivity level down to $1\mu\text{W}\cdot\text{cm}^{-2}$ and a relative wavelength accuracy of $\pm 5\text{nm}$ for visible light.

Although those ILDS systems appear to be excellent in detecting laser light in CW and pulsed modes, in determining the pulse laser characteristics, the direction of illumination as well as having a wide field of view, they have several negative points. First, they are not able to distinguish laser light from other lights (LED for example) without losing sensitivity level, this can increase the false alarm rate. Moreover, the wide spectral band I would like to achieve is not accomplished without either decreasing the received signal power (detection

of low power laser becomes difficult) or duplicating the detectors (expensive option). Finally, a lot of processing needs to be done to give the different characteristics of the laser and it increases the countermeasures reaction time.

Scattering recognition

Scattering recognition systems fall into the category of non-direct and off-axis detection of the beam. The amount of light scattered from the original beam depends on the laser type, the wavelength and the propagation medium [27]. One can think that a simple laser detection system, based on coherence or spectrum recognition could work to detect scattered laser light. It is actually true, but a scattering recognition system will be more interesting for long off-axis distance detection (up to 100 meters off-axis) where the two other systems fail to detect weak scattered light. Moreover, a scattering recognition system would be useful when the parameters for scattering light are optimal, which is the case in the maritime environment [75]. This fact combined with a need of long off-axis distance detection are the reasons why this laser detection system is mainly used for warship applications.

This part introduces models of scattering on background aerosols. A model that studies the distribution and optical properties of aerosol particles (interaction properties between the particle radiation at different wavelengths) needs to be considered before designing a detection system. This model predicts the behaviour of the laser scattered light knowing the environmental conditions. There exist many models and they differ by the number of input parameters (atmospheric pressure, sea temperature, relative humidity etc.) they take into account. The oldest one is the Shettle and Fenn models [76] that take only 4 parameters into account. An alternate, the EMAC/MADE-IN model [77] has combined two former models (the MADE-IN model [78] which defines aerosol dynamics properties and the EMAC model [79] which defines aerosol chemistry properties) to achieve better results. Another model introduced in 2005 [75] considered this time 12 input parameters.

Now, laser warning receivers based on scattering recognition are discussed. After the model is defined, the design of the system can start. Several papers can be found of such detection system [80, 81]. They are all based on spectrum recognition, using either an array of imaging sensors from which the power collection at every pixel is used to determine the pulse rate for example [82] or directly using a power meter which allows from the model to find the distance of the laser beam to the detector [75]. Those systems are able to detect CW and pulsed

lasers. However, they all failed in three criteria I am looking for in the technology: the size, the accuracy in the determination of the direction of the incoming lasers, and the wavelength measurement. Indeed, to detect scattering particles from a laser beam, the detector needs to be of an important size mainly due to the field of view coverage and the amplification combination. The laser wavelength determination is not considered for those systems and the direction of direct laser beam is impossible to determine from the scattered light.

Overall, those systems only determine the presence or not of a laser and the possible distance of the laser beam from the detector. They are thus not of interest for a direct detection of the laser beam that I would like to achieve first.

2.5 Discussion

In this chapter, I first studied basic properties of lasers and concluded that the coherence properties of a laser since being a unique feature of this technology would be a good discrimination criteria for our technology. In the second part of the chapter, I introduced different applications of laser detection technology including but not limited to military based requirements. I concluded that there was a demand for a wide field of view, a good sensitivity, a wide spectral range, a CW and pulsed laser detection and a short response time from the detection process. In the final part, I introduced the laser warning receivers in the market and classify them in three categories: coherence discrimination method, spectral discrimination method and imaging discrimination method. Table 2.5 shows a summary of each technology type with their main advantages and drawbacks.

Table 2.5: Summary of past laser detection technology with their advantages and drawbacks.

Type of discrimination	Type of technology	Advantages	Drawbacks
Coherence based	Fabry-Perot Michelson Mach-Zehnder Fizeau	Wavelength determination Discrimination laser / background light CW and pulsed lasers Low intensity detection	Short wavelength band (for Fabry-Perot) Long processing Misalignment of system Restricted field of view
Spectral based	Diffraction grating	Idem Wide field of view	Detection difficult at low intensity
Imaging based	Camera Photodetectors Scattering	CW and pulsed lasers Pulse characteristics Wide field of view (for camera)	Discrimination from background light difficult Wavelength determination accuracy

The imaging recognition in both photodetectors and camera systems has many advantages. The camera based systems achieve a good field of view determined by the size of the camera. Both types succeed in detecting CW laser and pulsed lasers as well as determining the pulse characteristics. They are able to discriminate laser from background light based on

the intensity of the laser. But there are two problems. One is that if a bright non-coherent source is detected, it can be seen as a laser beam. The other issue is the determination of the wavelength, which doesn't seem to be possible with these two systems only based on the power or the color detected (in that case a lack of accuracy on the wavelength). Moreover, I can affirm that the scattering recognition method is not of our interest for now. This method discriminates scattering light from background light by mainly looking at the power of the incoming light which is not reliable. However, one paper introduced a technique to determine the pulse rate of a pulsed laser and this is something I have to keep in mind for a future research.

On the other hand, the coherence detection systems seem to have more to offer. Interferometers have for a long time been used to determine laser wavelengths and so they might be our first choice. However, the Fabry-Perot interferometer is definitely not feasible in our case because of the short wavelength band restriction. The scanning Michelson and Mach-Zehnder interferometers [6] seem efficient in discriminating lasers from background light and in detecting low intensity. They are a good solution for a low-cost and efficient detection but the long processing would be a disadvantage in terms of the limited time we have to take the appropriate countermeasure (only 3-6s between the detection of the laser threat and the attack). The other discrimination technique is the diffraction grating. It is also able to determine laser wavelength and it is efficient in discriminating lasers from background light but the inaccuracy on the wavelength detection causes a problem at low intensity. However, one recent paper using a FZP pattern [61] has shown promising results in wavelength resolution but it did not consider aberration correction to improve the sensitivity level. Using this technology while correcting the astigmatism on the FZP as it was done by Benton [62] would improve the sensitivity level and wavelength resolution.

Chapter 3

Low cost laser detection system with a 360 degree azimuthal field of view

The first approach on laser detection system is based on a technology created by David Benton[6]. This work improves the field of view of the detection system as well as implementing a method to determine the direction of the incoming laser. After a brief introduction on several laser detection systems and their field of view, the principle of the technology will be explained and then the method to extend the field of view and to determine the direction of the laser beam will be shown.

Some parts of this chapter were presented in the SPIE Security + Defence conference in 2019 [83], and a journal paper was published in Optical Engineering in 2021 [7].

3.1 Background study

3.1.1 Field of view of existing laser detection systems

In defence, laser detection systems are highly researched since lasers have been used for decades for communication, navigation, guidance, control and weapon systems[84]. Most of the laser system applications use high energy pulsed lasers [85], however some applications such as laser aiming modules or beam rider guidance are using low power CW lasers [86]. LWR have been developed to identify the nature of the laser threat as well as the direction of irradiation. Very few of the current LWRs in the market are effective against CW lasers. Moreover, another requirement to detect CW lasers comes with the increase of the uses of

laser pointers in the last decade [87]. To answer these needs, our detection system is focused on the detection of CW lasers and a low cost implementation of a wide field of view is added in this chapter for a better coverage of the scene.

Typically LWRs are composed of three units: an optical unit, a detection unit, and a processing unit [40]. The field of view of an LWR depends on the composition of the optical and/or detection unit but can be extended with additional optical components. For example, imaging laser detection systems (ILDS) are usually composed of a fish-eye lens and CCD or CMOS camera devices [70] and can reach 180° of field of view. Oftentimes several ILDS units need to be combined together to reach a 360° full azimuthal coverage [73]. However, this is not a cost-effective system. Interferometer based detection systems are another type of LWR that make use of coherence detection, their field of view will be restricted by the size of the interferometer aperture and the optical path of the system. A static Michelson interferometer associated with an optical antenna has demonstrated a 45° horizontal coverage[54] while a Fabry-Perot based LWR has already achieved a horizontal field of view of 160° [46]. Sometimes, the field of view needs to be reduced to 120° in order to increase sensitivity in the system[8]. Diffraction gratings can also be used as part of detection systems, and typically rely on the use of a CCD camera. In 2014 a fish eye lens was combined with a sinusoidal amplitude grating and the system was able to achieve a 160 ° field of view [41].

An additional feature of a laser detection system requirement is the measurement of the laser wavelength, although not discussed in this chapter, this is a requirement to keep in mind for the future system to use. Among all the LWRs, interferometer based systems and diffraction grating based systems are the most reliable at determining the wavelength. However, they are mostly working with pulsed lasers[88, 89], their field of view is limited [41] and/or they are complex and expensive [90, 54].

The laser detection system used for this work is composed of a modified MZ interferometer and a balanced detector[6]. It is able to detect weak, continuous laser sources against bright broadband backgrounds. The field of view of the MZ system has been measured and is equal to $\pm 3^\circ$. The aim of this work is to expand the field of view thereby making the device more practical. In addition to the field of view, the incoming beam direction has been studied as it is essential to determine the origin of the threats.

3.1.2 Typical coherence properties among light sources

In this part, a summary on typical coherence properties of light sources is done [18, 91]. Table 3.1 summarises different sources and their coherent lengths. As can be seen from this table,

Table 3.1: Example of light sources and typical coherence lengths in free space.

Source type	Wavelength (nm)	Coherence lengths
Filtered sunlight	400-800	800 nm
Light emitting diode (LED)	632	12 μm
Light emitting diode (LED)	1000	20 μm
Laser diode	649	92 μm
Laser diode	532	200 μm
Low pressured sodium lamp	589 nm	600 μm
DPSS UV laser	346	<1 cm
Diode-pumped solid-state laser	405 nm	>1 m
Multi mode HeNe laser	633	20 cm
Single mode HeNe laser	633	300 m

laser diodes tend to have smaller coherence lengths and can be as low as 100 μm . Single mode lasers have higher coherence lengths, and even have the possibility to reach kilometers of coherence [92]. Moreover, although non laser lights are known to be non coherent, they have actually some amount of coherence and this needs to be carefully considered when the discrimination of lasers from background light is discussed for our laser detection system.

3.2 Configuration of the laser detection system

3.2.1 Principle of detection - coherence modulation

Unlike conventional laser detection systems based on the detection of enhanced brightness, the laser detection system presented here works by detecting light sources that have a significant coherence length. For this to work, the path difference between the two Mach Zehnder arms is required to be longer than the coherence length of the background light, which is the case with a difference of few micrometers in length. A piezo-mounted mirror replaces one of the two reflective mirrors of the original Mach-Zehnder interferometer to modulate the path length in one arm. The path difference combined with the modulating element cause the output signal to be modulated at a known frequency only if the input light has a longer coherence length than the path difference. In other words, detecting a modulating signal will indicate the presence of laser light in the system. Knowing this, the Optical Path Difference (OPD) is

manually defined by adjusting the piezo mirror distance in one arm until a spectral width is detected by the system. The exact OPD cannot be determined unless it is characterised with the use of different low coherent sources.

The detection part is composed of two balanced photodiodes at the outputs of the interferometer and a data acquisition unit (USB-6341 Multifunction I/O Device) used to digitize and send the data to a computer. A schematic representation of the detection system is shown in Fig. 3.1. The plano-convex lens (focal length $f=7.5$ cm, 2.5 cm aperture size) helps to focus the laser beam on the two photodetectors. To have a compact and easily transportable device, the size of the optical components were minimized. The beam splitters and the mirrors are 1cm long. The total optical path length from the focusing lens to the photodetectors is equal to 7.5 cm. The photodiodes are Si type and have a wavelength detection range from 350 nm to 1100 nm. The detectors are 3 mm long each and this combined with the optical path of the system (7.5 cm) limits the field of view to $\pm 3^\circ$. For this experiment, I used a 635 nm laser diode, the piezo mirror was modulated at a frequency of 1.2 kHz and at an amplitude of 2.5 V.

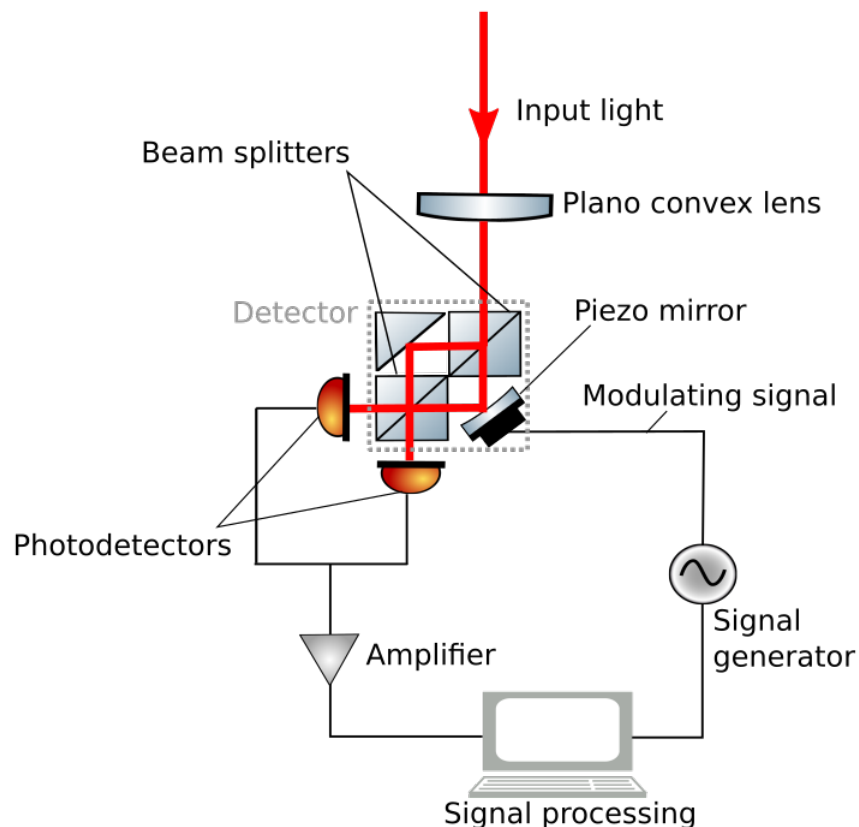


Figure 3.1: Configuration of the Mach-Zehnder laser detection system.

The photodiode signals are amplified using a transimpedance amplifier. These signals are then sampled and a Fourier transform analysis is made: peaks in the Fourier transform at the modulation frequency (and its harmonics) are evidence of coherent input. A rolling average spectrum was generated by summing consecutive frequency spectra. The graph in Fig. 3.2 gives an example of a signal modulated at 1200 Hz detected by the two balanced photodiodes and the Fourier transform applied to the signal where the second and third harmonics are visible.

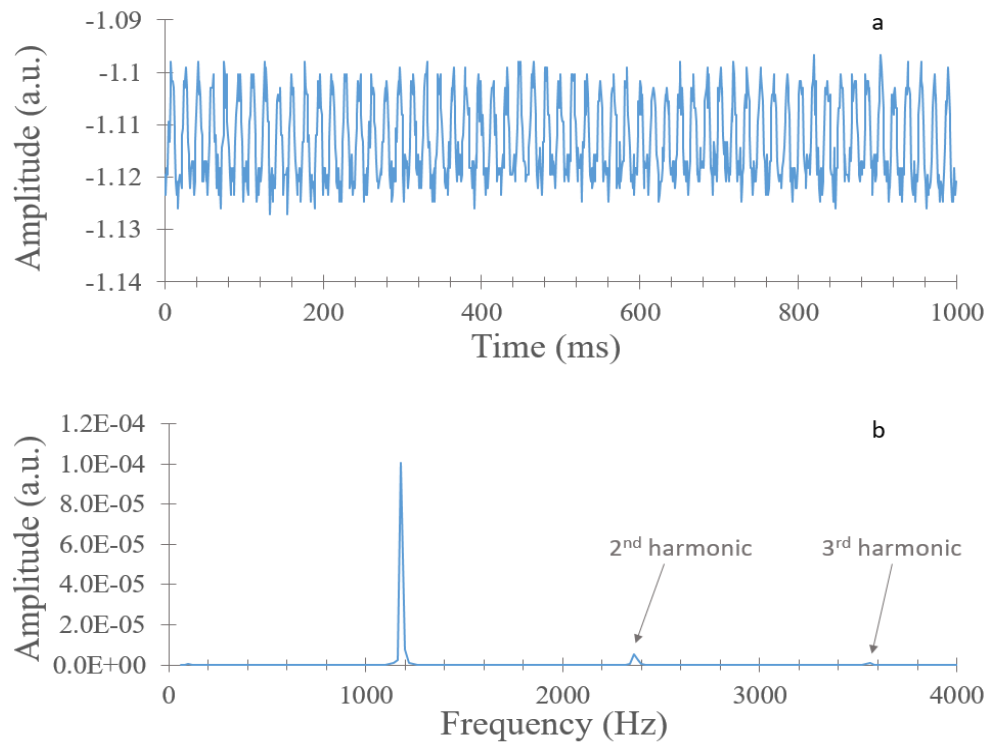


Figure 3.2: a) Example of an output CW signal modulated at 1200 Hz received by the balanced photodiodes. b) Fourier transform of the signal.

3.2.2 Laser detection theory

For an MZI with a path length modulated with a sinusoid of frequency f_m the intensity modulation at the output port is given by [6]:

$$I_d = \frac{1}{T}(E(1 - R(\lambda))R(\lambda)\gamma)^2[1 + \cos(k(\Delta L(t)))] \quad (3.1)$$

Where $R(\lambda)$ is a wavelength dependent reflectivity for the beamsplitters, E is the light field amplitude, γ is a factor representing reflection loss, T is the sampling time (i.e the time interval

between successive samples), $k = 2\pi/\lambda$ and ΔL is the path length difference between the length of the two arms L_1 and L_2 :

$$\Delta L(t) = L_1 - L_2(0) - v_m p \sqrt{2} \sin(2\pi f_m t) - v_{off} p \sqrt{2} \quad (3.2)$$

Where v_m is the voltage modulation amplitude v_{off} is a dc offset voltage applied to the mirror and p is the response of the piezo in $\mu m/V$. The factor $\sqrt{2}$ is due to the piezo mirror being at a 45 degree angle. Combining constant terms into a factor C the intensity at the output ports can be written:

$$I_d = \frac{1}{T} (E(1 - R(\lambda))R(\lambda)\gamma)^2 [1 + \cos(k(v_m p \sqrt{2} \sin(2\pi f_m t) + C))] \quad (3.3)$$

The Term C is in fact a slowly varying term which also accounts for drift of the interferometer and thus affects the phase of the cosine term (kC) producing a sinusoid as it varies beyond $\pi/2$. This can be simplified using $I_0(\lambda) = \frac{1}{T} (E(1 - R(\lambda))R(\lambda)\gamma)^2$ and $\beta = kv_m p$

$$I_d = I_0(\lambda) [1 + \cos(\beta \sin(2\pi f_m t) + kC)] \quad (3.4)$$

Using the trigonometric identity $\cos(A + B) = \cos(A)\cos(B) - \sin(A)\sin(B)$, this can be expressed as a combination of sine and cosine contributions

$$I_d = I_0(\lambda) [1 + a(\cos(\beta \sin(2\pi f_m t))) + \sqrt{(1 - a^2)} \sin(\beta \sin(2\pi f_m t))] \quad (3.5)$$

where $a = \cos(\beta C)$ is effectively a phase dependent distribution factor. Using the Bessel function identities

$$\sin(z \sin \theta) = 2 \sum_{k=1}^n (-1)^k J_{2k+1}(z) \sin((2k+1)\theta) \quad (3.6)$$

$$\cos(z \sin \theta) = J_0(z) + 2 \sum_{k=1}^n (-1)^k J_{2k}(z) \sin(2k\theta) \quad (3.7)$$

where the functions J_k are Bessel functions of the first kind, this gives

$$I_d = I_0(\lambda) [1 + a [J_0(\beta) - 2J_2(\beta) \sin(2\pi 2ft) + 2J_4(\beta) \sin(2\pi 4ft) + \dots] + \sqrt{(1 - a^2)} (-2J_1(\beta) \sin(2\pi ft) + 2J_3(\beta) \sin(2\pi 3ft) + \dots)] \quad (3.8)$$

the intensity at the detector can thus be represented in terms of harmonics of the modulation frequency where the odd and even harmonics vary as independent sets but with fixed internal ratios. The effect of slow offset drift can thus adjust the relative power in odd and even frequencies through the factor a . This can be actively controlled using a voltage offset on the piezo mirror. Setting $a=0$ by controlling V_{off} produces the odd harmonics and removes the “lost” power that goes into the J_0 (DC) term.

3.2.3 Implementation of a wider field of view with a cone mirror

A way to combine a larger azimuthal field of view and the direction determination of the incidence light is with the use of a cone mirror (Edmund Optics). It is composed of a cylindrical base and a cone top, the top has a silvered coating allowing reflection of a good percentage of the light towards the direction perpendicular to the input light as show in figure 3.3a. The cone mirror used in the experiment has a diameter of 1 cm and a total length of 1.5 cm and reflects 90% of the light at 635 nm. A beam reflected from the cone mirror is widely distributed in an arc as can be seen in figure 3.3. The beam reflection is in a arc shape due to the type of laser used in this experience, I used a red laser which had an elliptical beam output. The arc length depends slightly on the incident angle and the incident angle can only vary by few degrees to get the best reflection from the cone mirror.

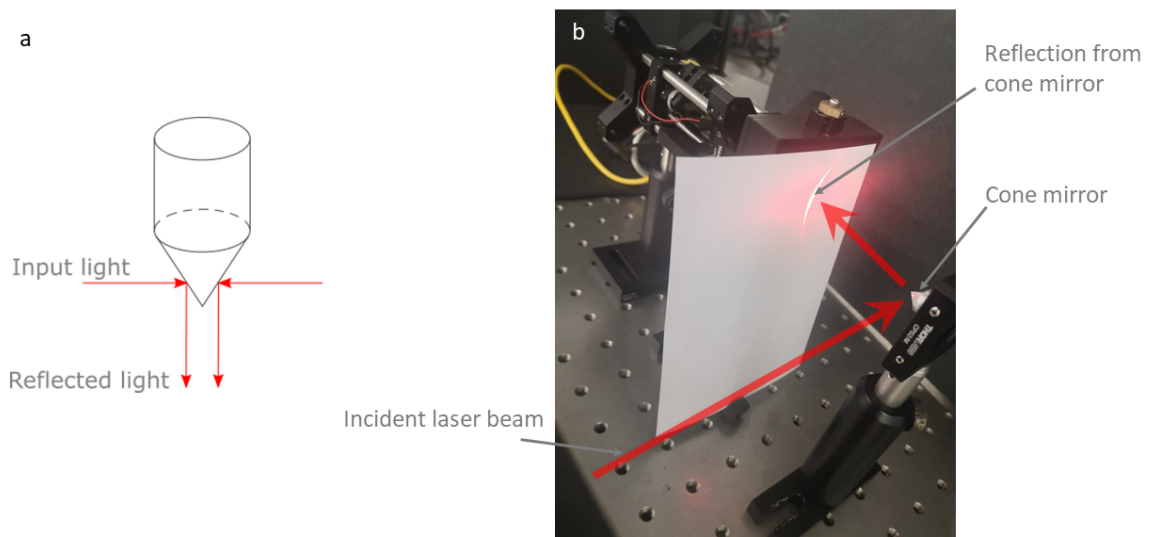


Figure 3.3: a) Reflection principle of the cone mirror. b) Example of a beam reflected by the cone mirror.

In this work, the aim is to both detect a laser source and determine the angle of incidence.

For that purpose, the previous detection system composed of two photodiodes has been modified: one of the outputs is used to measure the intensity of the modulating signal via one photodiode while the second output is used to determine the direction of the beam via a camera. Both functions can be performed at the same time. This will have an effect on the sensitivity which is reduced without the benefit of a balanced detector system.

The cone mirror is positioned to direct light into the interferometer and the system with the cone mirror is aligned vertically as shown in Fig. 3.4. The camera is looking through the interferometer from one of the output ports and is focused on the cone mirror. To show the effectiveness of this approach, a laser was directed into the system at various angles spaced by 45° . The 0° angle was set as illustrated in the figure. The amplitude of the first harmonic and a camera image were recorded for each angle (0° , 45° , 90° , 135° , 180° , 225° , 270° and 315°).

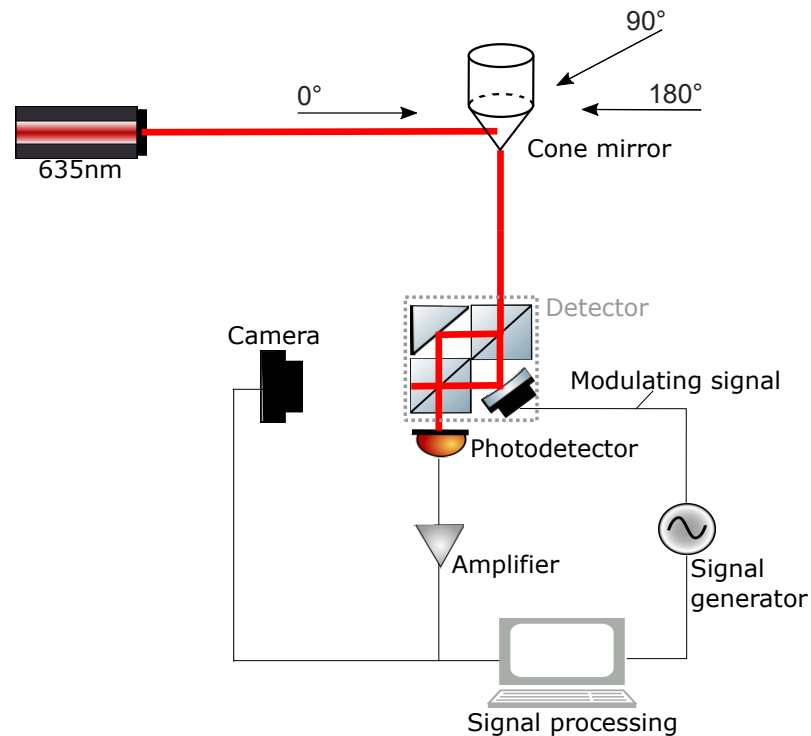


Figure 3.4: Configuration of the laser detection system with the cone mirror.

3.3 Experimental results

3.3.1 Determination of the direction of irradiation

In this part, I am looking at determining the direction of the incident light. Captured images of the cone mirror when the laser is shone at 0° and 225° are presented in Fig. 3.5. As it

can be observed on the captures, the beam is visible on the surface of the cone mirror and the direction of the laser input can be inferred from its relative angular position. It should be noted that the laser spots on the cone mirror appear different for different angles. The reason is that the laser was positioned manually around the cone mirror and it creates a possibility of misalignment on the laser-cone mirror vertical plane. This would then cause a different incident angle on the cone mirror and thus create a difference in the light reflected by the cone mirror. There is possibly also a misalignment of the cone mirror axis with the interferometer axis.

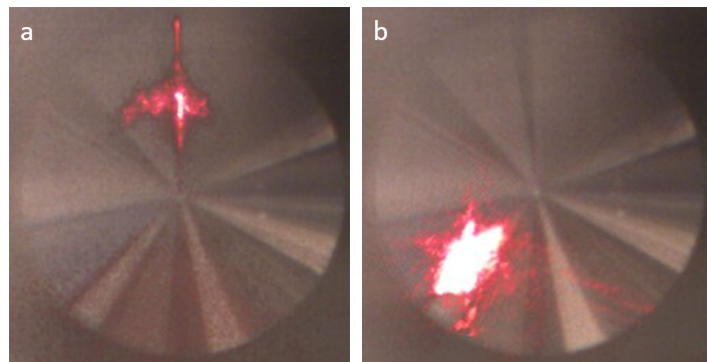


Figure 3.5: Captured images of the cone mirror when the laser is positioned at 0° and 225° .

While the first output of the interferometer is capturing the cone mirror images, the second output is simultaneously measuring the amplitude of the first harmonic of the signal. The results can be seen in Fig. 3.6 where both the amplitude of the first harmonic and the capture of the cone mirror are combined for each angle. In the graph, the radial distance represents the amplitude of the first harmonic.

These results show that the first harmonic is measured for every laser input angle. Thus it confirms that the laser is detected as a modulating input at every given angle. Moreover, the measured amplitudes of the fundamental frequency proved to be high, implying that weak signals could still be detected. Sensitivity measurements with and without the cone mirror have been studied and are shown and discussed in section 3.3.3. Finally, the captures shown in Fig. 3.6 also demonstrate that the direction of the laser beam can be determined from the camera at every angle. However, the capture of the cone mirror at 315° shows a deformed beam reflection which would impact the accuracy in the determination of the irradiation direction. Nevertheless, if the centre of mass of the beam is calculated for each capture, a better accuracy of the direction can be worked out. Thus, an estimated angular accuracy of

$\pm 5^\circ$ in the direction of the laser can be asserted.

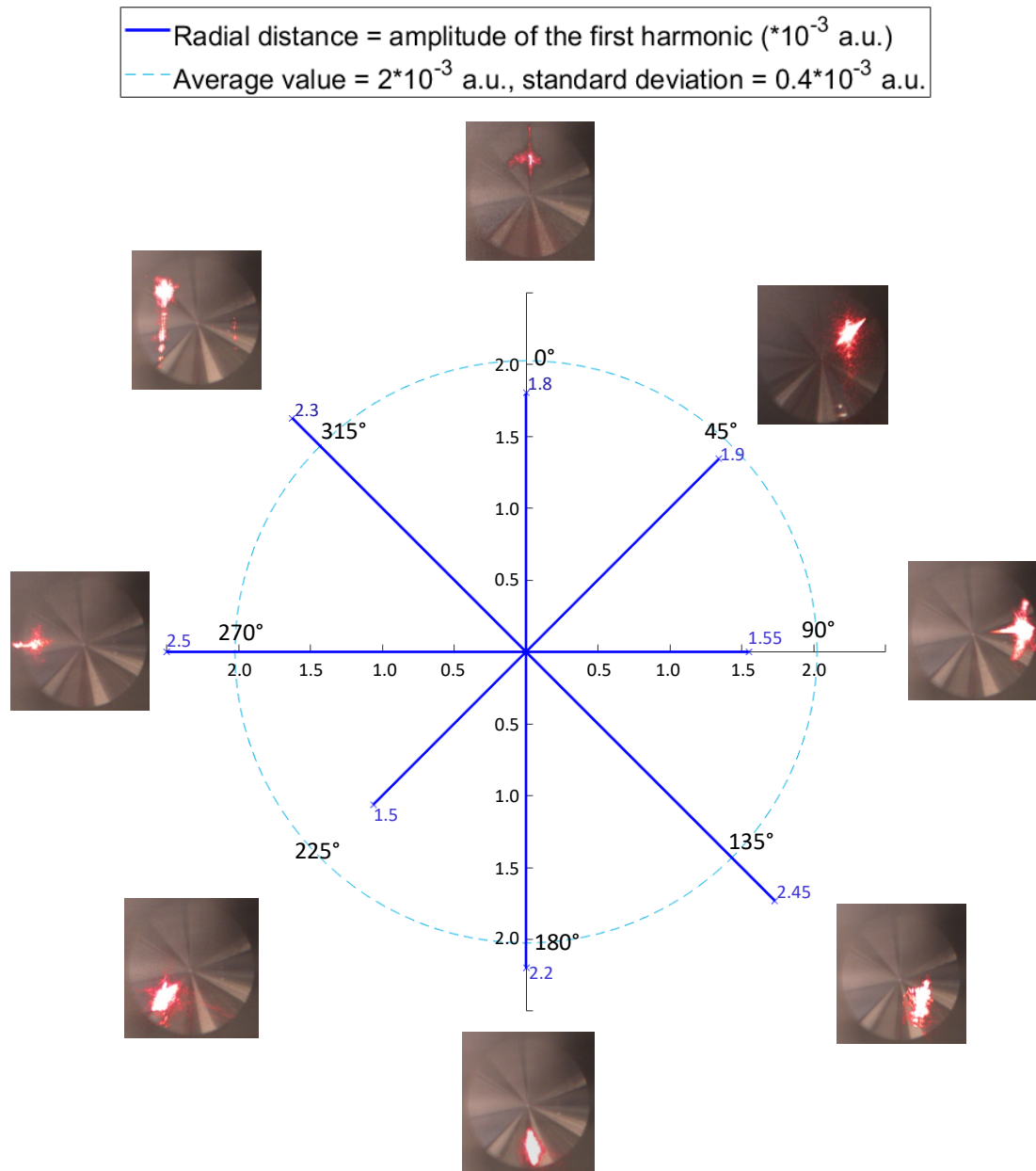


Figure 3.6: Combined data of the first harmonic amplitude and the cone mirror image for every angle spaced by 45° .

3.3.2 Transmission efficiency measurements for original and cone mirror systems

In this section, the difference in signal attenuation between the original system (see Fig. 3.1) and the cone mirror system (see Fig. 3.4) is analysed. The signal attenuation is calculated by looking at the power of the laser beam before it enters the detector and after it leaves through the last beam splitter. To have a relevant comparison with the cone mirror system

whose detection part is composed of one single photodiode, only one of the two outputs in the original system is measuring the power. The intensity of the laser diode is attenuated with Neutral-Density filters and a power meter is used to measure the input/output power level.

In Fig. 3.7, the input/output power ratio for the original system and for the cone mirror system are shown. This gives a transmission efficiency of 37% for the original system and of 3% for the cone mirror system. The original system had a maximum 50% transmission efficiency to be expected as only one of the two output ports is used in the measurement, the additional efficiency loss is due to the optics in the Mach-Zehnder interferometer. In the cone mirror system, the additional losses are the result of the typical beam shape reflected from the cone mirror (see Fig. 3.3b) since only a part of the beam can reach the detector input.

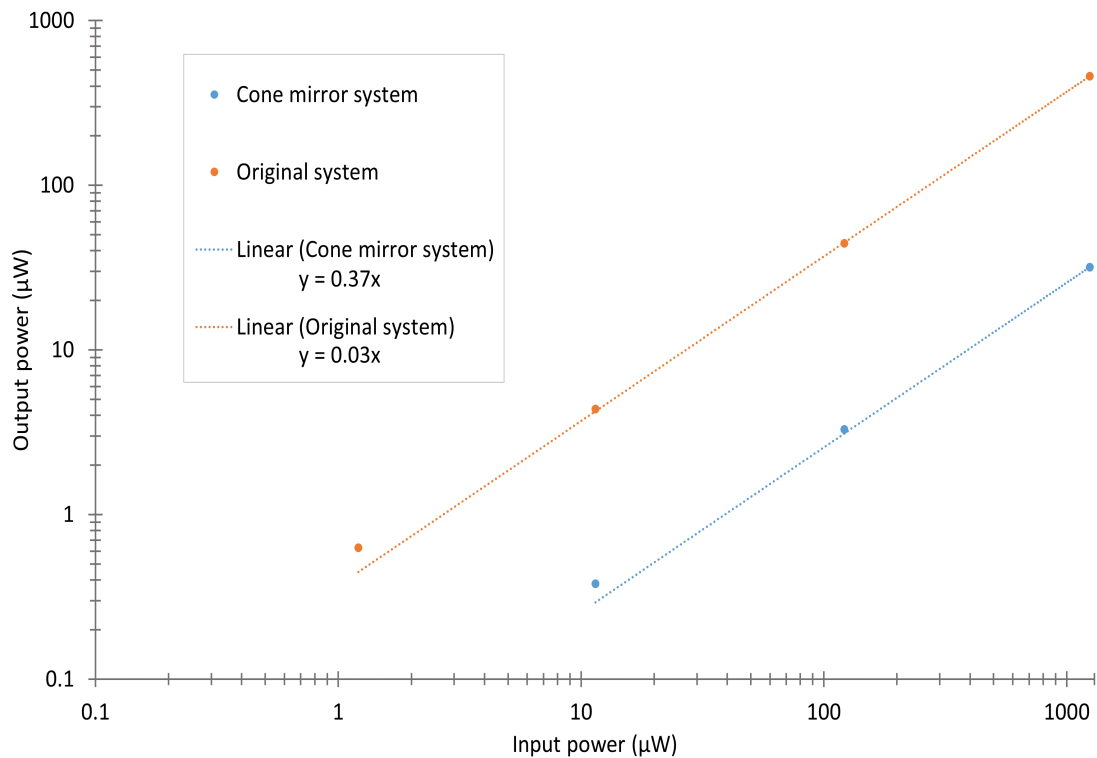


Figure 3.7: Transmission efficiency comparison between the cone mirror and the original systems.

3.3.3 Sensitivity measurements for original and cone mirror systems

The sensitivity corresponds to the minimum laser power required to detect a peak in the Fourier transform. Sensitivity measurements are done by measuring the Signal to Noise ratio (S/N) for different laser powers, the S/N ratio is calculated by measuring the amplitude of the fundamental harmonic and by comparing it to the noise level in the Fourier transform.

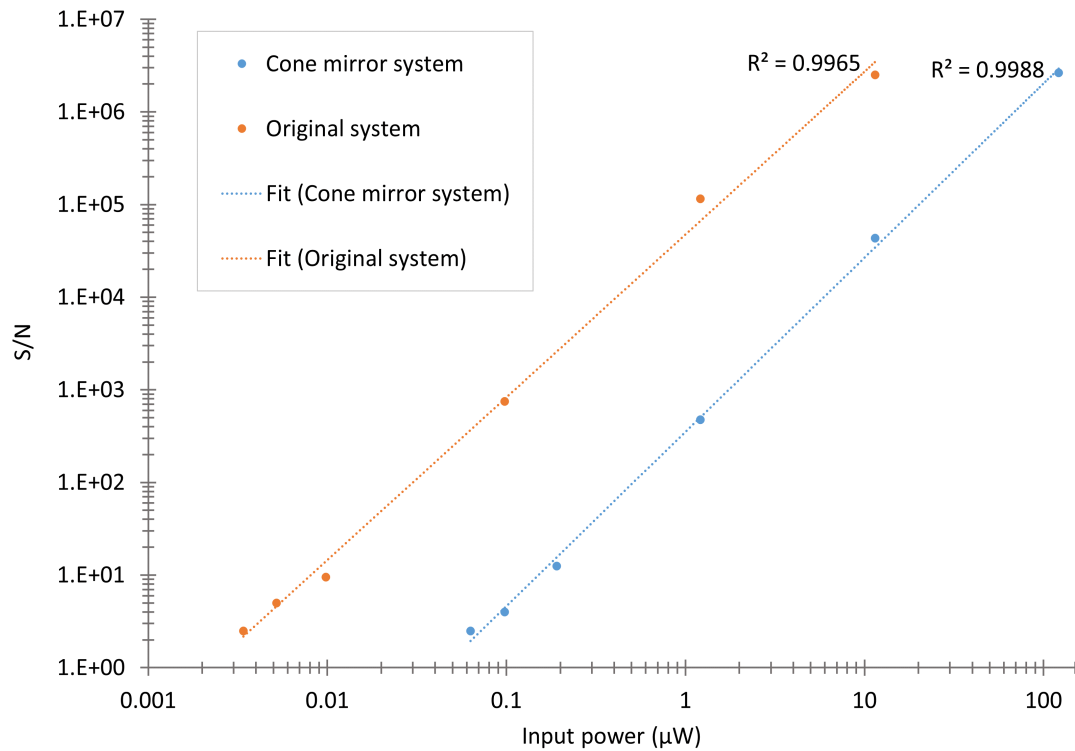


Figure 3.8: Sensitivity comparison between the cone mirror and the original systems.

The results are plotted in Fig. 3.8.

These results showed that the cone mirror system is able to detect a signal down to around 70 nW (or $1 \mu\text{W}\cdot\text{cm}^{-2}$) for an average processing time of less than one second; this is the ultimate sensitivity, the detected power or irradiance for which $S/N=1$. These are quite interesting results, they attest that the system when combined with a cone mirror is still able to detect weak signals under 100 nW. Moreover, it can be seen that without a cone mirror (original system), the ultimate sensitivity is around 2 nW or $0.03 \mu\text{W}\cdot\text{cm}^{-2}$. Thus it can be seen that we have traded the benefit of a wide detection field of view for a reduced sensitivity. Nevertheless the system retains a useful sensitivity level.

3.3.4 Confirmation of laser detection system principle

To demonstrate that the modified Mach-Zehnder interferometer combined with the cone mirror detects only coherent sources, an LED and a laser were both directed towards the cone mirror. Both were at similar wavelength (635 nm) and can be seen on the camera image of the cone mirror in Fig. 3.9. The LED appears significantly brighter on the camera image; however, no change in the amplitude of the first harmonic is seen when the LED is turned on and off.

As expected the LED contributes nothing to the modulation signal thus proving that the system is successfully distinguishing coherent sources. However, although the camera indicates

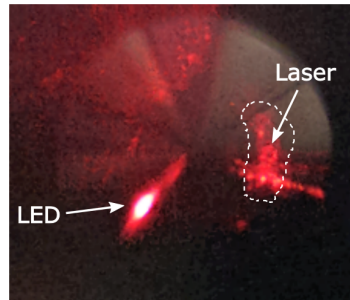


Figure 3.9: Captures of the LED and the laser beam reflections on the cone mirror.

the presence of two sources, it cannot distinguish the laser from the LED source.

3.4 Conclusion

LWRs which can detect CW lasers and have a wide field of view are relatively uncommon. In this chapter, I presented a means to widen the field of view of a MZ detection system and to determine the laser direction of a CW laser. A cone mirror was introduced into the system and allowed a CW laser to be discriminated from background light for a range of input angles, demonstrating a 360° field of azimuthal detection. With the use of a camera at one of the two system outputs, images of the cone mirror are captured. They show the position of the laser source on the cone mirror from which the source direction can be inferred. The direction determination method impacts the sensitivity of the system however it is an acceptable compromise to get a wider field of view since using only one output of the Mach-Zehnder interferometer with a photodiode is enough to detect a laser signal down to 70 nW (or $1 \mu\text{W}\cdot\text{cm}^{-2}$). Moreover, if an LED is reflected together with a laser from the cone mirror, the LED is not detected by the system, confirming the ability to discriminate lasers from non laser sources.

Overall, this modified detection system comes with a high sensitivity and a wide spectral range (in this case, the photodiode has a spectral range from 350 nm to 1100 nm). The spectral range could be extended to infrared with suitable optics and IR detectors. The acquisition time of the detector is less than one second for weak sources which are integrated, less than 100ms for stronger sources. If a pulsed laser is used with the current camera and cone mirror system, the detection should be possible on the condition that the integration time is increased

for higher rate lasers. Determining the pulse repetition rate should then be straightforward by looking at quick changes in brightness over time on the camera. In terms of the detection against bright background, which would be a more realistic representation of outdoor conditions, David Benton [6] mentioned it in his paper, achieving a laser detection of tens of nW against a bright halogen lamp with the use of a balanced detector in the MZ interferometer. With the cone mirror, only one photodetector is used, so this would imply a possible laser detection down to around few hundreds nW. This can be improved with better optical components, such as a larger aperture, currently its length is of around 1 cm and limited by the piezo mirror small size. A second realistic issue that was not investigated in this chapter is the impact of the atmosphere on a laser beam, especially scintillation. Scintillation leads to a depletion in the image quality and a change of intensity over time. This was not the main purpose of this chapter however, and this was more carefully investigated in reference [93]. The use of a camera for direction finding could produce issues when multiple sources are present, as this responds to brightness. In this work an LED and laser at the same wavelength were indistinguishable to the camera, and sufficed to say that one of the sources was a laser without being specific. In general, if the sources were of different wavelengths this may be sufficient to discriminate them (if a colour camera is used). Moreover, the imaging of the beam in the cone mirror requires some image analysis to increase the angular accuracy in the direction determination, so far being at $\pm 5^\circ$.

Chapter 4

Optical characterization and correction of a DMD based detection system

In the previous chapter, I expanded the field of view of a laser detection system based on a Mach-Zehnder interferometer. A 360° horizontal field of view was achieved by implementing a cone mirror to the system and the source direction was determined by adding a camera to the set-up. Although promising results were found with this system, the main drawback as a laser warning receiver is the importance of the optics alignment that can affect the efficiency of the system. Benton in 2020 [94] addressed this problem with an MZI interferometer and liquid crystal modulators and removed any moving part from the detection system. However, it was shown to have a slower response and to be less sensitive. Thus, I need to find a laser detection system that can detect CW lasers, have a wide spectral range and an already existing wide field of view would be advantageous too.

In chapter 2, I previously studied laser detection systems and concluded that diffraction gratings based LWR are the most advantageous in terms of wavelength determination and field of view. The combination of Fresnel Zone plate (FZP) with a Digital Micromirror Device (DMD) becomes quite interesting as both FZP and DMD are binary devices and rely on diffraction and could have potential for use as a LWR. Indeed, FZP is a focusing device for which the focus depends on the wavelength. So, this device would be interesting for detecting a wide range of wavelengths, not restricted to visible light either. Moreover, the DMD being used as a diffractive element implies that lasers and background light should be distinguishable. So, this important criteria for an efficient laser detection system should be filled too. Thus, the FZP combined with the DMD has the possibility to achieve a great laser detection system.

Although the wavelength determination has some drawbacks for low intensities in diffraction gratings based LWR, Mohagheghian and Sabouri showed very promising results in 2018 with the use of a FZP on a DMD to determine visible wavelengths and obtained a wavelength accuracy of 0.10 nm [60]. They didn't however correct optical aberrations in their system, which could improve the focusing efficiency and the sensitivity level. Benton, however, started the correction of astigmatism in 2018 to improve the efficiency of such systems [62]. In this chapter I continue his work by using Zernike polynomials for additional wavefront correction. The laser detection system is composed of a DMD and a camera.

This chapter is focused on the characterisation and the correction of optical aberrations present in the DMD based laser detection system. The first part of this chapter studies the advantages of both the DMD and FZP along with a quick study on optical aberrations. The second part is aimed at determining the optical aberrations created by the DMD, while the third part will present the algorithm developed to correct the optical aberrations. The fourth part shows the results of the algorithm applied on the laser detection system. Finally, the last part will discuss the results.

4.1 Background study

In this background study, a first introduction on optical aberrations is shown followed by a study of wavefront correction. Then, Fresnel Zone plates are explained as well as important properties inherent to them. Finally, the digital micromirrors device is studied with the implementation of the FZP on the DMD.

4.1.1 Basic of optical aberrations

There exists two concepts in optical aberration that are important to distinguish: wave aberrations and ray aberrations. When the rays from an object pass through an optical imaging system, it creates an image [95]. First, let's look at the image of a point source where no aberrations are present, this "ideal" image is also called a diffraction-limited image [96]. Figure 4.1 illustrates the wavefronts of an aberration-free object and an aberrated image. The light diverging from a point source S propagates as sinusoidal waves, centered on the point S [97]. An aberration-free image would be created by an imaging system if the object rays converged to an image point S' . However and in reality, the surfaces present in the optical

imaging system will affect the spherical wavefront. The deviation of the image wavefront from the reference spherical wavefront is defined as wavefront aberration and it represents the difference in optical paths lengths between the object and image wavefronts [98, 99]. The wavefront aberration unit is in wavelengths (of the light source). In consequence, the rays from the aberrated wavefront which propagates perpendicular to the wavefront surface will deviate from their original course and will not converge to the single point S' . The deviation of the ray at the point S'' from the image point S' is called the transverse ray aberration. And the distribution of rays around the image point S' is called a spot diagram.

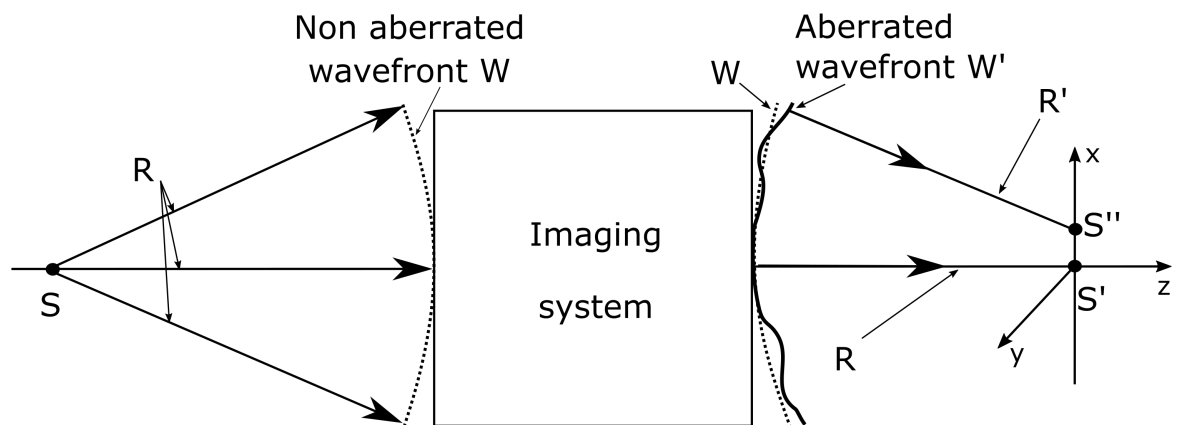


Figure 4.1: Illustration of a non aberrated wavefront passing through an imaging system that results in an aberrated wavefront.

Moreover, optical aberrations can be classified in two categories: monochromatic and chromatic. Monochromatic aberrations are due to the nature of lenses and mirrors while chromatic aberrations is caused by dispersion and occurs when several wavelengths are used. The two types of aberrations are explained in details in terms of ray aberration in the following subsections.

Chromatic aberration

There exists two different types of chromatic aberrations caused by dispersion: longitudinal and lateral[100]. Longitudinal aberration are on axis aberration: different wavelengths will focus at different locations on the optical axis. While lateral aberration are off axis aberration: different wavelengths will focus at different locations on the plane perpendicular to the optical axis. Figure 4.2 illustrates those two aberrations. Both types of chromatic aberration can occur

at the same time.

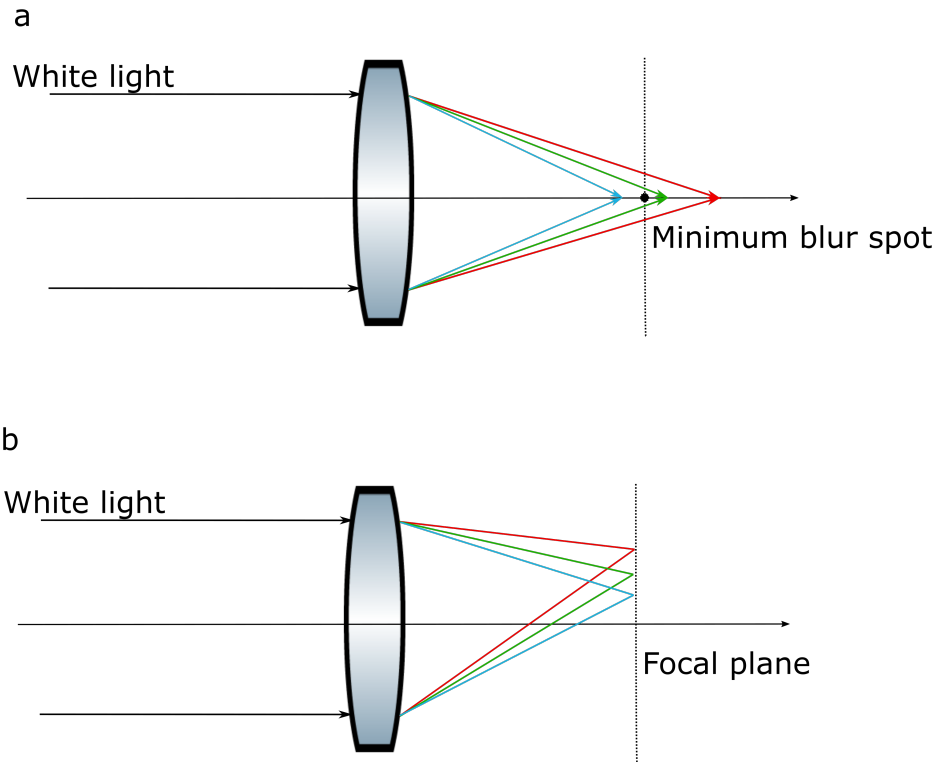


Figure 4.2: Chromatic aberration: a)Longitudinal b)Lateral.

Monochromatic aberration

For a pupil point with polar coordinates (r, θ) , the aberration function of a rotationally symmetric system can be written as a power-series expansion as (ch.13 from [101]):

$$W(\rho, \theta) = \sum_{n=0}^{\infty} \sum_{m=0}^n a_{nm} \rho^n \cos^m \theta \quad (4.1)$$

where $\rho=r/a$, with a the radius of the exit pupil and a_{nm} an expansion coefficient which represents the peak value of an aberration term.

$$a_{nm} = a^n \sum_{l=0}^{\infty} {}_{2l+m}a_{nm} h'^{2l+m} \quad (4.2)$$

h' is the height of the image. Aberration types are associated with an order defined as: $i = 2l + m + n$. There exists 5 primary aberrations, corresponding to order $i=4$, and called Seidel aberration functions: spherical aberration, coma, astigmatism, field curvature and distortion [99, 101, 102, 103]. Lower order aberration exists as well, such as piston, tilt and defocus. However piston and tilt are not exactly optical aberrations as they only shift the focal

point without aberrating the image.

- Defocus aberration : defocus aberration is simply when an image is out of focus. It corresponds to a shift on the optical axis of the focus. In consequence, the image appears blurry.
- Spherical aberration : spherical aberration is the only monochromatic aberration existing on the optical axis. It is caused by spherical surfaces when rays from the edge of the surface (i.e. marginal rays) focus at a different point than the rays from the center (i.e. paraxial rays). Fig. 4.3C is an exaggerated drawing of spherical aberration. The smallest region where the rays are contained is called the circle of least confusion.
- Coma: coma affects off-axis sources and is defined as the variation in magnification over the entrance aperture. It is caused by the refraction differences in the diverse zones of the lens and it implies that the marginal rays will focus at different heights than the paraxial rays. Figure 4.3D illustrates this aberration. In consequence, the image of a point source will appear distorted and will look like a comet.
- Astigmatism: astigmatism is defined when two perpendicular rays focus at different points on the optical axis. Figure 4.3E illustrates the astigmatism aberration. The image created is then either elliptical or a circular blur. Astigmatism can either impact off-axis points and it increases the more off-axis we get, or it occurs in non-symmetrical system and then even on-axis points can be impacted.
- Field curvature: field curvature is created when off-axis points focus in different focal planes than the axial points. It occurs when a flat object normal to the optical axis creates a spherical image. Figure 4.3A illustrates an exaggerated field curvature aberration. In consequence, the image will not be uniformly sharp. This aberration is caused by the surface curvature.
- Distortion : distortion is an aberration easy to recognize as the whole image is deformed by it. Figure 4.3B shows the two types of distortion aberration (b: pincushion distortion, c: barrel distortion) against the object a. The cause is the change in magnification with field angle: the bigger the field of view, the more the magnification changes.

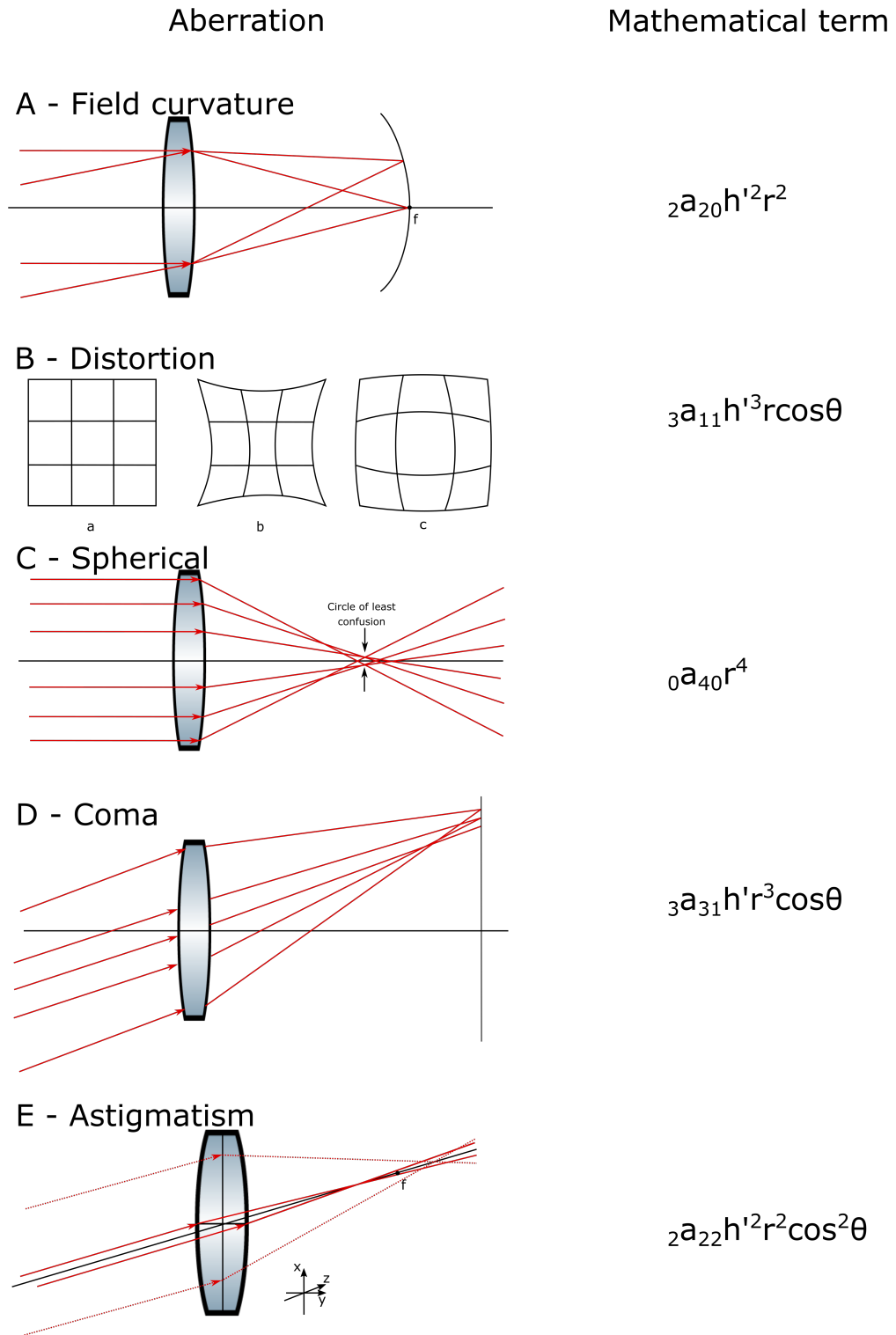


Figure 4.3: Primary aberrations and their mathematical terms. ${}_2a_{20}$, ${}_3a_{11}$, ${}_0a_{40}$, ${}_3a_{31}$ and ${}_2a_{22}$ represent the coefficients of field curvature, distortion, spherical aberration, coma and astigmatism. h' is the height of the image and (r,θ) the polar coordinates of a pupil point.

4.1.2 Adaptive optics and introduction to Zernike polynomials

Adaptive optics

Adaptive optics is the combination of wavefront sensing and wavefront correction. The measurement of the wavefront is made by using a wavefront sensor and is based on light intensity distribution. The most common wavefront sensors are the Hartmann-Shack wavefront sensing and interferometric sensors [101]. But the former is highly expensive while for the latter, although having a better performance, their optics are difficult to align and the algorithm used to extract the information from the interferometric pattern can be difficult to implement. With most of these systems, the reconstructed wavefront is expressed in terms of Zernike polynomials, where the amplitude of each polynomial represents the degree of aberration [104]. In this thesis, I developed a simple dynamic algorithm to correct the focus based on intensity measurement by implementing Zernike polynomials to both define a focusing lens and to correct optical aberrations inherent to the system (see. part 4.2).

Aberration theory using Zernike polynomials

I have included the power expansion function often used to describe aberration in equation (4.1). However, one big disadvantage of this function is that the polynomials don't form a complete set and they are not orthogonal over a unit circle, which is an important characteristic to get independent polynomials. To counter this problem, Zernike polynomials are used and the new aberration function becomes (ch.13 from [101]):

$$W(\rho, \theta) = \sum_{n=0}^{\infty} \sum_{m=0}^n c_{nm} Z_n^m(\rho, \theta) \quad (4.3)$$

Their advantages are many: they represent balanced aberration yielding minimum variance, their orthonormality gives us access to the standard deviation of the aberration term $c_{nm} Z_n^m(\rho, \theta)$ directly by the coefficient c_{nm} and their orthogonality implies that the coefficient c_{nm} will not change if more aberration terms are added or subtracted from the aberration function. Moreover, if we compare the mathematical terms of field curvature and distortion from figure 4.3 with the Zernike terms from table 4.2, we notice that the field curvature and the distortion aberrations have the same dependency in (r, θ) than respectively the defocus and the tilt Zernike polynomials [95]. Thus, the defocus and tilt terms are used to correct the field

curvature and the distortion aberrations.

Now, as stated before, our system is composed of a Digital Micromirror Device, which has a rectangular surface. Zernike polynomials are fitted on a circular surface and as such using them could lead to major problems and a non-efficient use of the given surface. To counter this problem, Legendre polynomials could be used, as they represent aberrations of a slit aperture. However, Mahajan showed that they are not suitable for a system with an axis of rotational symmetry and introduced instead orthogonalized Zernike circle polynomials over a rectangular pupil [105, 106]. Table 4.1 shows the difference between the circular and rectangular Zernike polynomials as written on the DMD and table 4.2 explicits the first terms of the rectangular polynomials [107].

4.1.3 Fresnel Zone Plates

Fresnel zone plates are a focusing device based on diffraction. Other diffractive elements often used in laser detection are the horizontal grating and the double-slit experiment as explained in the first chapter. The choice of the Fresnel Zone plate over these two element came for its inherent ability to dynamically manipulate the focal length of the input light when combined with an SLM device. This implies that at the exit of the system, a camera, used to analyse the diffraction pattern, does not need to be moved to gather all wavelengths on its aperture, unlike other diffractive elements. Another type of focusing plate are the Gabor zone plates and unlike FZP they only have one pair of conjugate foci. They do however obtain a similar focusing efficiency at the first focus and the simplicity of the FZP pattern over the Gabor zones plates makes it a better choice for now [108, 109]. FZPs have been used for decades and have a wide range of applications including but not limited to visible, UV, and x-ray wavelengths. In this section, I first study the focusing principle behind an FZP and I then look at the main properties of a FZP.

Focus principle

Diffraction is at the origin of the focusing principle in FZP. If we consider a reflective grating as in Fig. 4.4, constructive interferences will occur for waves in phase, so for an optical path

Table 4.1: Representation of circular and rectangular Zernike modes written via LabVIEW on the DMD.

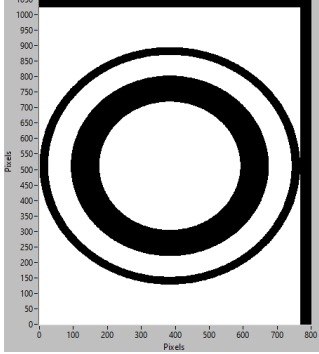
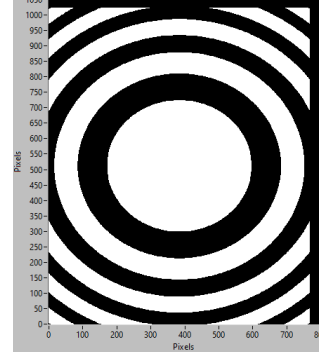
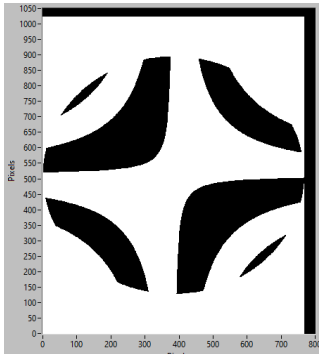
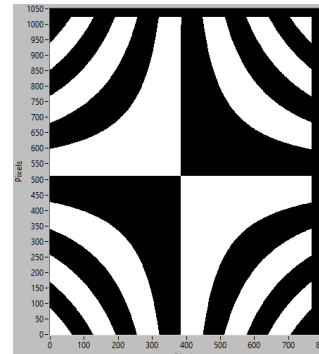
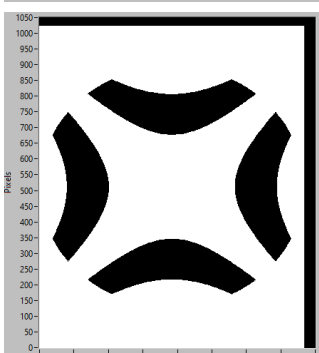
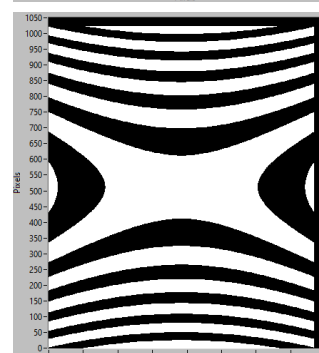
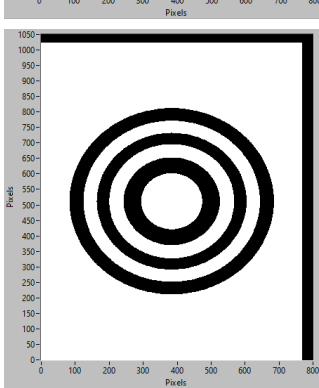
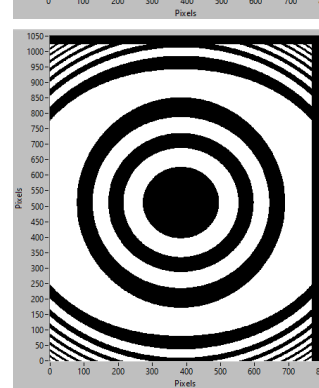
Mode name (mode number)	Circular polynomials	Rectangular polynomials
Defocus (4)		
Oblique astigmatism (5)		
Vertical astigmatism (6)		
Primary spherical (11)		

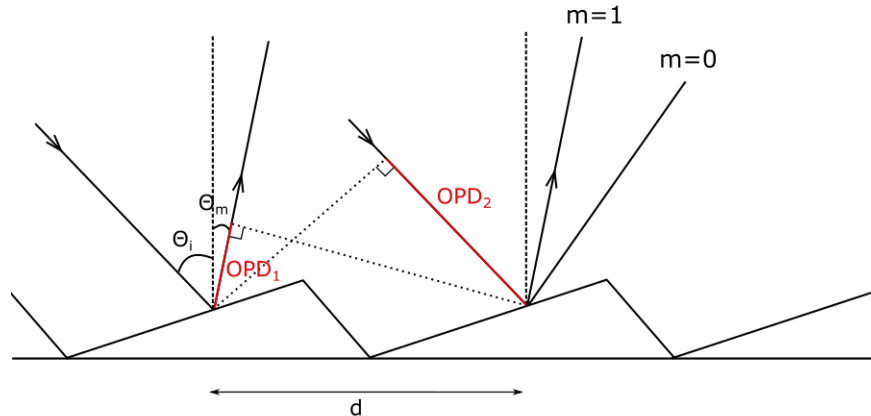
Table 4.2: Rectangular Zernike polynomials in polar coordinates where "a" correspond to the conversion factor from circular surface to rectangular surface, $a=0.8$ in our case, taken from reference [107].

Mode number	Rectangular Zernike polynomials	Aberrations types
R1	1	Piston
R2	$[\sqrt{3}/a]\rho \cos \theta$	Tip
R3	$\sqrt{3/(1-a^2)}\rho \sin \theta$	Tilt
R4	$[\sqrt{5}/(2\sqrt{1-2a^2+2a^4})](3\rho^2-1)$	Balanced defocus
R5	$[3/(2a\sqrt{1-a^2})]\rho^2 \sin 2\theta$	Balanced oblique astigmatism
R6	$[\sqrt{5}/(4a^2(1-a^2)\sqrt{1-2a^2+2a^4})][3(1-2a^2+2a^4) \times \rho^2 \cos 2\theta + 3(1-2a^2)\rho^2 - 2a^2(1-a^2)(1-2a^2)]$	Balanced vertical astigmatism
R7	$[\sqrt{21}/(2\sqrt{27-81a^2+116a^4-62a^6})] \times (15\rho^2-9+4a^2)\rho \sin \theta$	Balanced vertical coma
R8	$[\sqrt{21}/(2a\sqrt{35-70a^2+62a^4})] \times (15\rho^2-5-4a^2)\rho \cos \theta$	Balanced horizontal coma
R9	$[\sqrt{5}\sqrt{(27-54a^2+62a^4)/(1-a^2)}/(8a^2(27-81a^2+116a^4-62a^6))][(27-54a^2+62a^4)\rho^3 \sin 3\theta - 3[4a^2(3-13a^2+10a^4) - (9-18a^2-26a^4)\rho^2]]\rho \sin \theta$	Balanced vertical trefoil
R10	$[\sqrt{5}/(8a^3(1-a^2)\sqrt{35-70a^2+62a^4})] \times [(35-70a^2+62a^4)\rho^3 \cos 3\theta - 3[4a^2(7-17a^2+10a^4) - (35-70a^2+26a^4)\rho^2]]\rho \cos \theta$	Balanced oblique trefoil
R11	$[1/(8\mu)][315\rho^4+30(1-2a^2)\rho^2 \cos 2\theta - 240\rho^2+27+16a^2-16a^4]$	Balanced primary spherical

difference of λ and as such, the diffraction grating equation can be easily derived:

$$OPD_1 + OPD_2 = d(\sin \theta_i - \sin \theta_m) = m\lambda \quad (4.4)$$

where $m = 0, \pm 1, \pm 2 \dots$ is the propagation order of interest.


Figure 4.4: Diffraction from a reflective grating showing the 0th and +1 order and the total optical path difference ($OPD_1 + OPD_2$).

Similarly, a zone plate is usually composed of transparent and opaque zones, each zone is separated by an optical path difference of $\lambda/2$, so the waves are out of phase. This phase difference between two consecutive zones implies that only destructive interference would be created if two consecutive zones were transparent, hence the use of opaques zones at every other number to avoid this. Two consecutive transparent zones have then the same polarity of phase and create constructive interferences at the image point. The optical path length difference between the first zone and the n^{th} is equal to $n\lambda/2$. The FZP focus principle is illustrated in Fig.4.5.

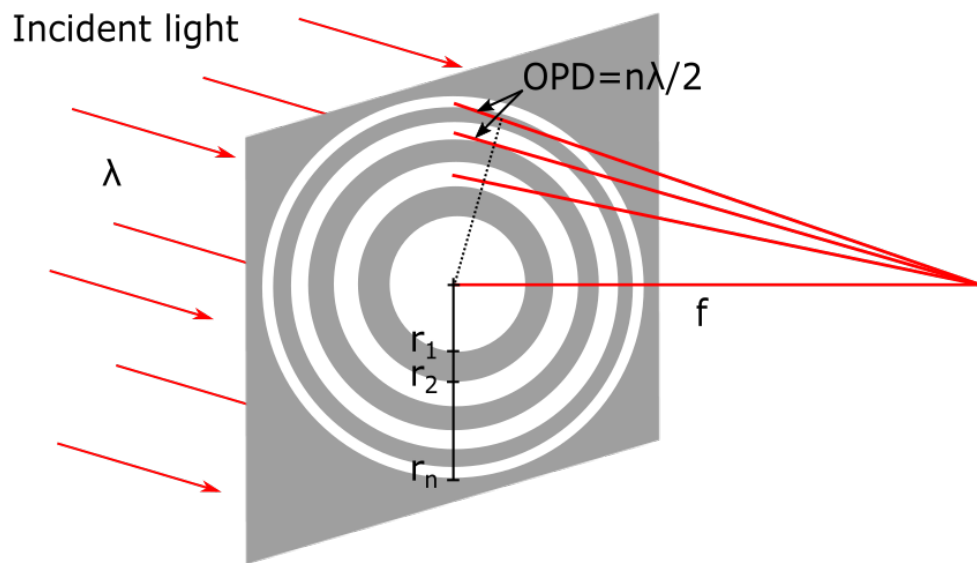


Figure 4.5: Zone plates with transparent odd zones showing the first order of focus.

From figure 4.5, Pythagorean theorem will get us after simplification:

$$r_n^2 = n\lambda f + \frac{n^2\lambda^2}{4} \quad (4.5)$$

where r_n is the radius of the n^{th} zone, λ the wavelength of the incident light and f the first order foci. The second term of equation 4.6 represents spherical aberration but it can be ignored for $f \gg n\lambda/2$ and thus the FZP equation becomes:

$$r_n \simeq \sqrt{n\lambda f} \quad (4.6)$$

Just as a diffraction grating will have multiple order of diffraction, a FZP will also have multiple order of focus and they can be defined with the relationship:

$$f_m = \frac{f}{m} \quad (4.7)$$

with $m = 0, \pm 1, \pm 2, \dots$ the foci order and where, unlike diffraction gratings, negative orders will give virtual foci of negative focal length. The different foci efficiencies will be discussed in the next part. Moreover, equation 4.6 shows that the focal length is inversely proportional to the wavelength which implies that different wavelengths will focus at different distances from the origin. This demonstrates the longitudinal chromatic aberration inherent to FZP [110, 111].

Properties of FZP

Just like a lens, the diffraction pattern from a FZP results in a Airy pattern. The Airy pattern for a zone plate at its first order focus can be written as:

$$\frac{I_1(\theta)}{I_0} = N^2 \left| \frac{2J_1(ka\theta)}{ka\theta} \right|^2 \quad (4.8)$$

where I_1 is the intensity at the first focus, I_0 is the intensity of the incident illumination, $N = D^2/(4\lambda f)$ the total number of zones when D is the diameter of the lens, the function $|J_1(v)/v|^2$ the Airy function, a the lens radius, $k = 2\pi/\lambda$ and $\theta = r/f$. However, this is the only similar characteristic between a FZP and a lens. Due to diffraction and losses from opaques zones, FZP have less focusing efficiency than lens, they however can achieve a better resolution if the number of zones is over 200 [112]. Other focusing systems exist, but they are expensive, unstable due to the moving parts and can generate some noises [113]. Equation 4.8 also indicates that the more zones there is in the zone plate, the higher the intensity on the focal point will be. Furthermore, the diffraction efficiency of a FZP based on opaque and transparent zones can be defined as[114]:

$$\eta = \begin{cases} 1/4 & m=0 \\ 1/m^2\pi^2 & m \text{ odd} \\ 0 & m \text{ even} \end{cases} \quad (4.9)$$

What this means is that, outside of the 50% of the incident light lost and absorbed by the opaque zones, there is an additional 25% of incident light that will be directly reflected ($m=0$), the first orders focus will both get 10% of intensity ($m=\pm 1$) and the odd orders do not focus. Additionally, the Rayleigh resolution, which gives us the focal spot size in diffraction limited condition, can be defined for a FZP as:

$$d_r = 1.22d_N \quad (4.10)$$

where $d_N = \frac{\lambda f}{2r_n}$ is the outermost zone width. Equation 4.10 indicates that the resolution is limited to the smallest structure that defines our FZP, the pixel size of the DMD. Finally, the depth of focus, which can be defined as the amount of displacement on the optical axis away from the focal point for which an acceptably sharp focus is still detected and can be written for a FZP in term of the outermost zone width as:

$$d_f = \pm \frac{2d_N^2}{\lambda} \quad (4.11)$$

Optical aberrations in zone plates

Section 4.1.1 introduces what optical aberrations are and defines the most common found in optical imaging systems. However in this section, we will not need to explicitly look at the optical aberrations created from FZP. Indeed, Young studied in 1972 optical aberration in zone plate and expressed the optical path difference as [115]:

$$OPD = \frac{n\lambda}{2} + \frac{r_n^4}{8f^3} \dots \quad (4.12)$$

where the first term describes a diffraction limited wavefront and the remaining terms describes the wavefront aberrations. $\frac{r_n^4}{8f^3}$ is the spherical aberration term. The wavefront aberration starts to be important when $\frac{r_n^4}{8f^3}$ is superior at $\lambda/4$. So this combined with formula (4.6) implies that we can get an aberration free image if the number of zones of FZP is limited by:

$$N^2 \leq \frac{2f}{\lambda} \quad (4.13)$$

which is easily achieved in our case. For example, a HeNe laser focusing at the distance 46cm will give $\sqrt{2f/\lambda} = 1205$ zones while N will be under 200 zones when considering the DMD

dimensions.

However, since I am looking at discriminating lasers from background light or in other words, monochromatic light from non-monochromatic light, it is interesting to introduce the chromatic aberration of FZP. Equation 4.6 indicates that if the light is not monochromatic, the focal length would be impacted severely thus FZP can create important chromatic aberrations. If we consider a FZP for which there is no optical aberrations, then $OPD = \frac{n\lambda}{2}$, and just as before, chromatic aberrations will be present at another wavelength λ' if $OPD = \frac{n\lambda'}{2} \pm \frac{\lambda'}{4}$. This can be rearranged so that to avoid chromatic aberrations, the number of zones N needs to adhere to:

$$N \leq \frac{\lambda}{\Delta\lambda} \quad (4.14)$$

where $\Delta\lambda$ is the spectral bandwidth of the light.

4.1.4 Modeling a FZP on a DMD

As I am trying to dynamically correct optical aberrations and to focus different laser wavelengths at the same focal length, which requires different pattern of FZP, the use of a DMD comes as a good choice to achieve these goals. A DMD is an electronically controllable Spatial Light Modulator (SLM) and as such would allow us to programmably alter the FZP pattern quickly. Compared to other types of SLMs, the DMD has certain advantages, including a polarization invariance, a fast response rate of up to 32kHz and a wide wavelength range from UV to IR [116, 117]. Although limited by the depth of modulation due to the fixed value of the mirrors angle, Turtaev et al. proved recently that DMDs perform better at beam-shaping than Liquid crystal (LC) based SLM[118]. The reason is that LC-SLMs have poor scattering compared to DMDs and it contributes to non-controllable background noise. However, DMDs do have a major disadvantage, its focusing efficiency is low - down to 8% against 42% for the LC-SLM in their experiment. Additionally, the combination of a DMD with a FZP will affect an already poor efficiency. This needs to be acknowledged and the focusing efficiency of our system will be studied in detail in this section. The most widely available kit to interface a DMD with a computer - and the one I used - is given by Vialux and the programming is done via LabVIEW [119].

Principle of Digital MicroMirror device

A DMD is a reflective device composed of around a million micromirrors arranged in a rectangular array. Figure 4.6 illustrates the diffraction principle behind the DMD. Each mirror corresponds to one pixel in the image to be displayed. When the mirrors are in the "parked" state, it means the DMD is power-off and the mirrors rest parallel to the protective glass. When the DMD is on, the mirrors can rotate separately to an "on" and "off" states at a specific angle (usually $\pm 12^\circ$) so that the light is reflected towards two directions: the "on" state direction and the "off" state direction.

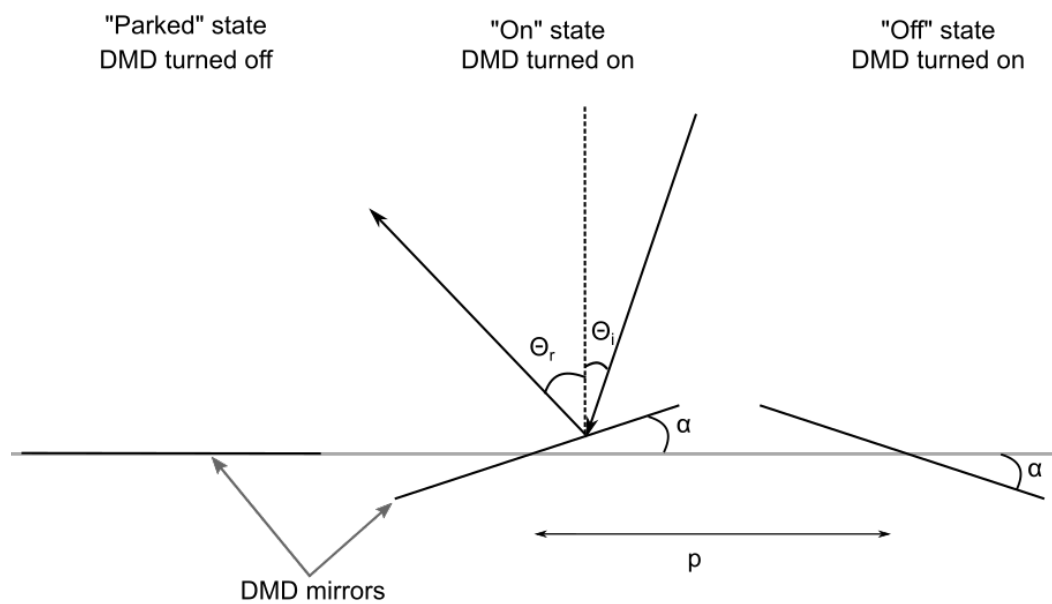


Figure 4.6: The different states of DMD mirrors: parked, on and off.

Although the DMD has often been referred as a blaze grating, Scholes et al. [120] recently proved that for small incidence angles for visible light, the DMD doesn't act as a blaze grating but more so as an augmented amplitude grating which is an important detail now to consider when I will be looking at the focusing efficiency of the FZP on DMD system. Before it, the implementation of the detection system is explained.

Implementation of the FZP on the DMD

The aim of the laser detection system is to characterise the laser wavelength by measuring the size of the beam at a constant radial distance from the DMD while the first order focal length of a Fresnel zone plate lens is varied. This wavelength characterisation method is similar to

[60]. The setup of this system is shown in Fig. 4.7. A 1024x768 resolution DMD with a mirror width of $13.6 \mu\text{m}$ and an angle deviation of $\pm 12^\circ$ is used in this work. To allow the two reflected beams to be coplanar with the incident light coming at 0° , the DMD is rotated at 45° . A black and white CCD camera from Thorlabs (DCU223M) with a 1024 x 768 resolution and a $4.65 \mu\text{m}$ pixel width is used.

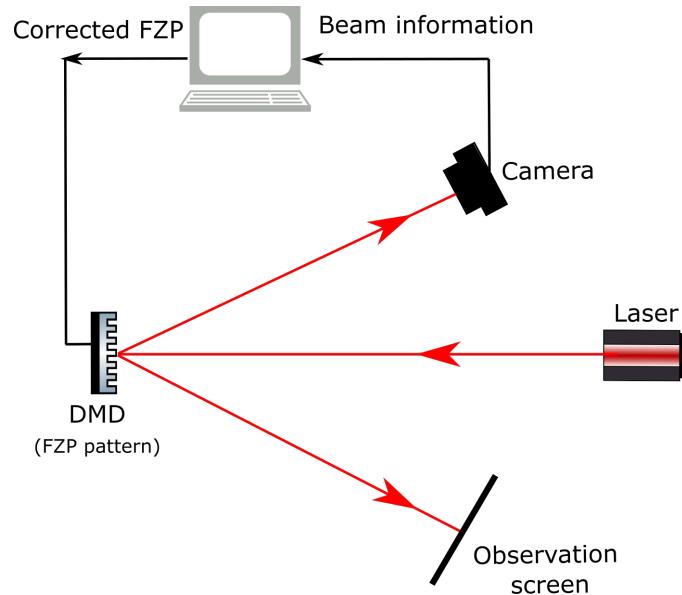


Figure 4.7: Laser detection system based on DMD.

To vary the focal length, the diffractive properties of the DMD are used and a FZP is written on the DMD: transparent zones are composed of the "on" state mirrors and focus the light towards the "on" state direction at $+12^\circ$ while the opaque zones are composed of the "off" state mirrors and focus the light towards the "off" state direction at -12° . To write the FZP pattern on the DMD, the defocus term of the Zernike polynomials is used: $R4(\rho) = A_{4,R} \times C(3\rho^2 - 1)$ where $A_{4,R}$ is the user controllable amplitude for the rectangular polynomials, C is a pre-calculated constant (see figure 4.2) and ρ the radial distance in the polar coordinate system. This equation can then define the different radii of the FZP lens in relation to the length of the DMD window. Figure 4.8 shows one FZP pattern written on the DMD. Since the FZP are written using one term of the Zernike series, the rest of them will also be used to correct the optical aberrations. Finally, the camera is used to analyse the characteristics of the beam. Two beam parameters are measured: the spot width and the peak intensity.

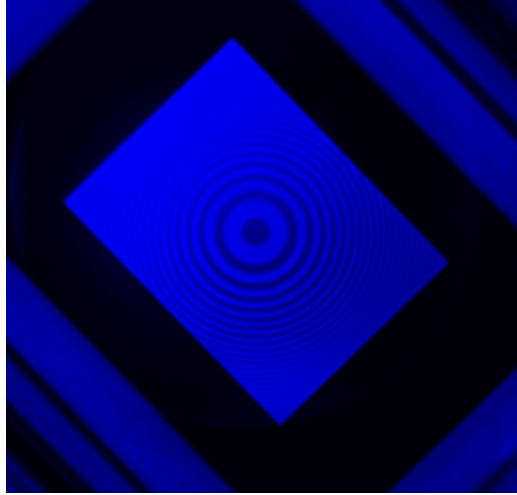


Figure 4.8: Fresnel zone plate written on the DMD.

Conversion defocus Zernike value to focal length

Before we consider the focal length formula for the rectangular polynomials, we need to define the formula for the circular polynomials as the derivation of the formula will be similar. First, let's consider our corrected wavefront, where each Zernike term except the defocus were defined to remove optical aberrations. In that understanding, only the defocus term will contribute to the focal length. The defocus contribution to the wavefront function W_C in term of circular Zernike polynomials is written in polar coordinates as [121] :

$$W_c(\rho) = A_{4,C} \times \sqrt{3}(2\rho^2 - 1) \quad (4.15)$$

Where $A_{4,C}$ is the amplitude of the circular defocus term in wavelength unit ($\lambda=632.8\text{nm}$ here). Moreover, the wavefront function can be defined in term of the focal length as [96]:

$$W(\rho) = \frac{\rho^2}{2f} \times r_c^2 \quad (4.16)$$

with r_C the radius of the DMD where the beam is reflected on for the circular polynomials pattern.

If we consider the maximum displacement of the Zernike mode for which $\rho = 1$, we can combine equations 4.15 and 4.16 and it gives the focal length for circular polynomials as:

$$f_c = \frac{r_{c,max}^2}{2\sqrt{3} \times A_{4,C} \times k_c} \quad (4.17)$$

With $r_{c,max} = (768/2) \times 13.68\mu m$ and k_c a scaling factor dependant on the wavelength.

Now, for the rectangular polynomials, if we consider the defocus contribution to the wavefront function as:

$$W_r(\rho) = A_{4,R} \frac{\sqrt{5}}{2\sqrt{1-2a^2+2a^4}} (3\rho^2 - 1) \quad (4.18)$$

Where a is the circular/rectangular conversion factor and equal to 0.8 in our case and $A_{4,R}$ is the amplitude of the rectangular defocus term in wavelength unit. Then if we consider again equation 4.16 at the maximum displacement of the Zernike mode for which $\rho = 1$ and combined it with equation 4.18, the focal length for the rectangular polynomials can be written as:

$$f_r = \frac{r_{r,max}^2 \sqrt{1-2a^2+2a^4}}{2\sqrt{5} \times A_{4,R} \times k_r} \quad (4.19)$$

Where $r_{r,max} = \sqrt{(768/2)^2 + (1024/2)^2} \times 13.68 \mu m$ is the radius of the DMD the beam is reflected on for the the rectangular polynomials pattern and k_r the scaling factor depending on the wavelength.

Focusing efficiency of the system

The focusing efficiency of the DMD combined with the FZP system has first studied by Benton [62]. He found with a generic approach a theoretical focusing efficiency of 1.6% and up to 3.8% when the beam is steered to the centre of the diffraction pattern (see Fig. 4.9).

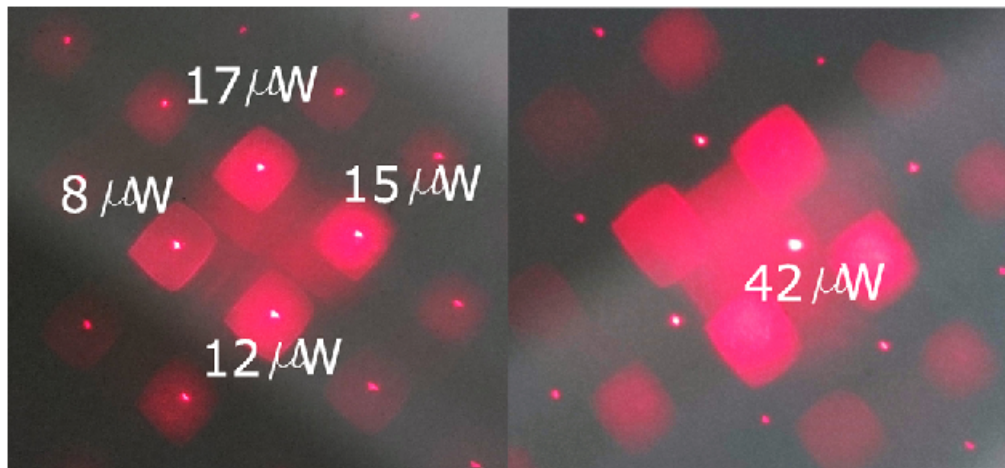


Figure 4.9: Comparison of intensity pattern with a central FZP (left) image and an offset FZP (right) for an input intensity of 1.1mW [62].

A more mathematical approach is given by [120]. The diffraction efficiency of the n^{th} order for the DMD combined with a grating can be calculated with:

$$\eta_n = \frac{\text{sinc}\left(w \frac{n + [\sin 2\theta_B + \sin \alpha]}{\Delta}\right)^4}{\sum_{m=-\infty}^{m=\infty} \text{sinc}\left(w \frac{m + [\sin 2\theta_B + \sin \alpha]}{\Delta}\right)^4} \cdot \left[\frac{1}{2} \text{sinc}\left(\frac{n}{2}\right)\right]^2 \quad (4.20)$$

Where $\text{sinc}(x) = \frac{\sin \pi x}{\pi x}$, θ_B is the mirror tilt angle ($=12^\circ$), α is the incident angle of the input light, w is the mirror width and Δ is the mirror spacing. $\Delta = w + \epsilon$ with ϵ an unofficial value between $0.8 \mu\text{m}$ and $1 \mu\text{m}$. Applying our values to this equation, I obtain an efficiency for the first foci of at best 5%

Moreover, the use of a DMD with a FZP implies that the opaques zones are now composed of "off" state mirrors and focus light towards a -12° direction allowing a second almost identical diffraction pattern in the system. Thus, I can access the laser output from two directions which can widen the range of wavelength of the detection system for example. In this thesis, my work will not be using the second output of the DMD system, however I will continue the discussion on possible applications in the conclusion chapter.

4.2 Analysis of DMD aberrations

In 2018, Mohagheghian and Sabouri [60] combined a DMD with a FZP to calculate laser wavelength. Their method relies on finding the actual FZP pattern which would focus a laser - with its specific wavelength - into a predetermined focal length. This focal length is set to be the distance between the camera and the DMD so that it would correspond to a focus on camera. To set this distance accurately, they use a HeNe laser as reference and they vary the FZP size for the given wavelength while keeping the camera distance fixed. They then look at the evolution of the size of the beam as a function of the FZP focal length. The FZP focal length can be found out from the FZP size based on the FZP equation 4.6. The evolution of the beam size is shown in figure 4.10.

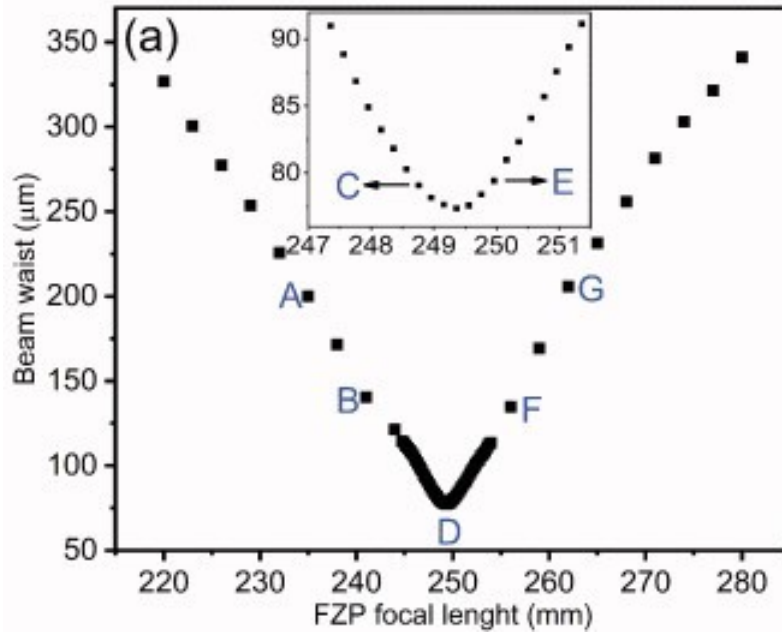


Figure 4.10: Evolution of the beam size as a function of the FZP focal length as reported in [60].

The FZP focal length corresponding to the smallest beam size will then be defined as the distance DMD-camera. After finding this distance, they then use again equation 4.10 but this time they vary the FZP pattern with the wavelength and have the focal length fixed and as predetermined. When the beam focuses on camera, the laser wavelength is determined. They repeated this measurement 500 times and for two lasers: HeNe at 632.8 nm and Nd:YAG at 532 nm. The average and the standard deviation of the 500 measured wavelengths is then calculated for each laser: 632.93 ± 0.03 nm and 532.06 ± 0.03 nm for respectively the HeNe and the Nd:YAG lasers. It is difficult to evaluate their wavelength resolution as their experiment is not a wavelength characterization but a wavelength calculation. Even if we were to look at their wavelength characterisation from figure 4.10, there is no accuracy measurement on the beam size that could lead us to determine the wavelength resolution.

Moreover, they measure a beam waist down to $75 \mu m$ for a focal length at 25 cm. However, after calculation, their diffraction limited beam waist should be around $12 \mu m$. This indicates that their experimental beam waist is around 6 times bigger than the diffraction limited beam waist. As they explained, they did not take into consideration the correction of possible optical aberrations which could lead to this important difference in the experimental beam size but also to a wrong characterization of the focal length. Indeed, they used the x axis to measure the beam size so already the astigmatism also present in their experiment would give a different focal length for the x and y beam lengths which would then lead to a wrong

focal length measurement for a given wavelength. Overall, their results are very promising. However, adding the correction of the beam phase profile could improve the determination of the real focal point and the beam size which would then allow a good wavelength resolution. There is no evidence of previous papers on this correction.

Before looking at the correction of the optical aberrations, I will determine their presence in the laser detection system. The phase profile of the beam is impacted by two main phenomena: astigmatism aberration and DMD window irregularities, both phenomena can distort the intensity distribution of the focal point. In this section, the two types of aberrations are studied.

4.2.1 Aberrations created by DMD properties

The first type of aberration to study is the aberration created by the irregularities on the window protecting the DMD. To highlight these irregularities, a phase map is made with the help of an interferometer based system. Two phase maps are made depending on whether the DMD is turned on or off using a HeNe laser, $\lambda = 632.8 \text{ nm}$. Figure 4.11 shows the phase map expected in an ideal case.



Figure 4.11: DMD interferogram in an ideal case.

DMD turns off

When the DMD is turned off, i.e. the mirrors are flat and not tilted, a Michelson type interferometer is used to produce an interferogram as shown in figure 4.12. A 50/50 beam splitter is used and a camera looking through the interferometer is focused on the DMD.

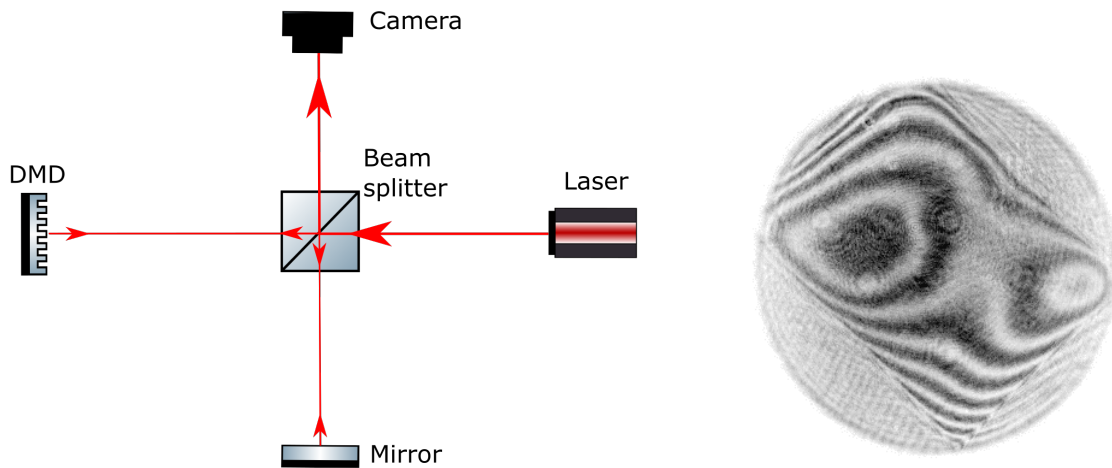


Figure 4.12: Michelson type interferometer and phase map of DMD when turned off.

DMD turns on

When the DMD is turned on, the incoming laser is reflected at a 24° angle and thus the previous set-up cannot work. This time, a pellicle beam splitter is used to transmit 92% of the incoming laser towards the DMD and to reflect 8% towards the camera. The transmitted beam is reflected on the DMD and the mirror and then joins the 8% of the initial split beam to create the interferogram as seen in figure 4.13.

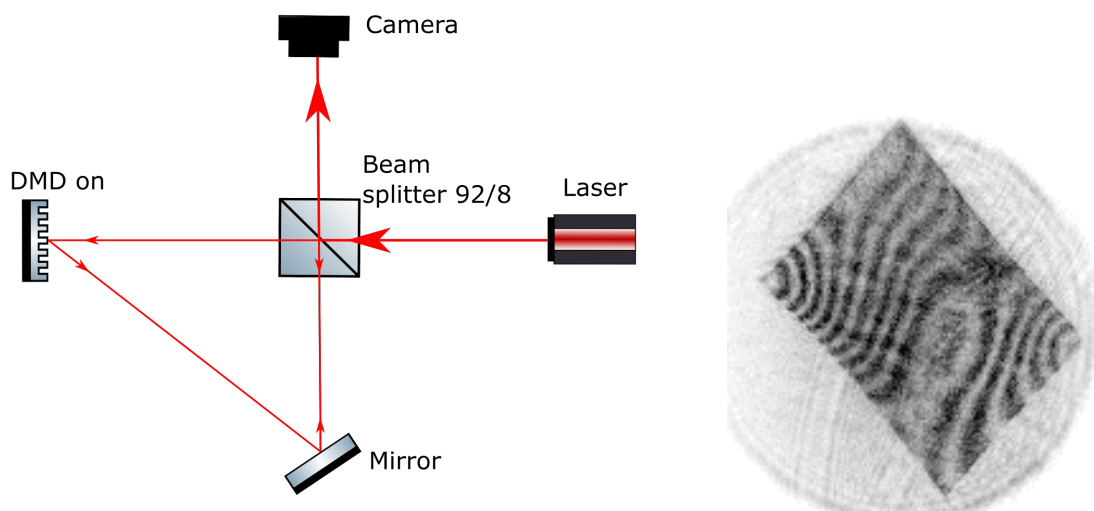


Figure 4.13: Interferometer and phase map of DMD when turned on.

Both of those phase maps show a phase profile with irregularities, which means that the DMD system can modify the beam profile.

4.2.2 Aberrations created by DMD orientation: astigmatism

The second type of aberration is created by the fact that the light is reflected at 24° on the DMD towards the camera: the camera sees the DMD off axis and the circles of the FZP look like ellipses which create different focal lengths in the horizontal and vertical directions. This defines astigmatism in the system and impacts the focal point shape. Figure 4.14 shows images of the beam spot for different focal lengths at the same radial distance from the DMD.



Figure 4.14: Beam spots taken from the same radial distance from the DMD while the focal length is varied [62].

The middle picture shows the circle of least confusion which is the smallest circle the rays can pass through: all the rays do not pass through the focal point due to astigmatism. The first and third picture are when the focal length is away from the camera, the spots are elliptical and imperfect. This astigmatism can cause inaccuracies on the beam shape, and difficulties in finding the focal point on itself. Correcting it should improve the accuracy of the focal length and thus of the wavelength determination.

4.3 Experimental beam optimization

An algorithm has been implemented on LabVIEW with the use of Zernike polynomials to write Fresnel zone plates and correct optical aberrations in the system. The Zernike mode numbers 1 to 15 are used. The algorithm can be separated into two parts: the first part is to systematically find the settings for the Zernike polynomials that will get the focal point located on the camera and the second part is to improve the shape of the beam. The steps of the algorithm are detailed in the following sections. The laser used is a HeNe laser at a wavelength $\lambda = 632.8$ nm.

4.3.1 Step 1: Determination of defocus Zernike term

In this first step, the amplitude of the defocus mode (mode R4) for which the focus sets on the camera is found by making use of the inherent astigmatism in the system. Indeed, from the camera perspective, the widths of the astigmatic beam in the vertical and horizontal directions show opposite behaviour before and after the focal point. Away from the focal

point, the horizontal and vertical widths are of different lengths: one is larger than the other due to astigmatism. When the largest width gets smaller closer to the focal point/camera, the other width gets bigger and this will continue so after the focal point. So, an intersection between the two measured widths would indicate the circle of least confusion, which for the first step I will define as the best focus. To make the width measurements, the camera is saturated (higher exposure time so that most of the pixels from the beam gets an intensity at 255), and an intensity threshold is applied on the camera image to let only intensity pixels over 245. In figure 4.15, an example of an oversaturated beam is shown as well as the vertical and horizontal widths I am measuring from the beam.

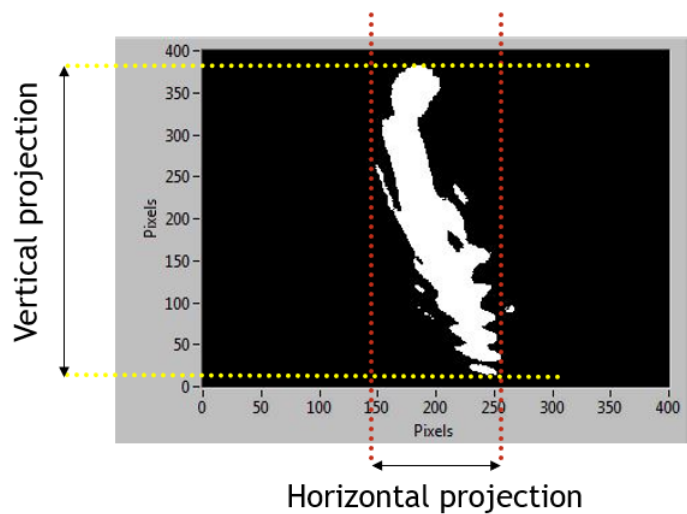


Figure 4.15: Horizontal and vertical projection of the beam length (pixel size = $4.65 \mu\text{m}$).

Using this, I can now vary the focal length (via the defocus) and look at the change in the x and y widths. The results are shown in Fig. 4.16 with the pre-correction widths. As expected, due to the strong astigmatism in the system, an intersection between the vertical and horizontal projections can be seen and this gives a good estimation of the focus.

The focus on camera is estimated to be for a defocus value of 23.00 ± 0.01 . This uncertainty is taken as the minimal step-size of defocus for which a distinguishable change in the beam is seen. Moreover, in figure 4.16, the beam measurements after aberration correction are also added and will be discussed in the next parts. It can however already be seen that the final corrected beam size is around 10 times smaller than the initial beam size.

4.3.2 Step 2: determination of R5 to R15 amplitudes

Once the defocus is set, the Zernike polynomials modes 5 to 15 can be determined to correct the beam from aberrations. This time a low exposure time is taken since I attend to adjust the

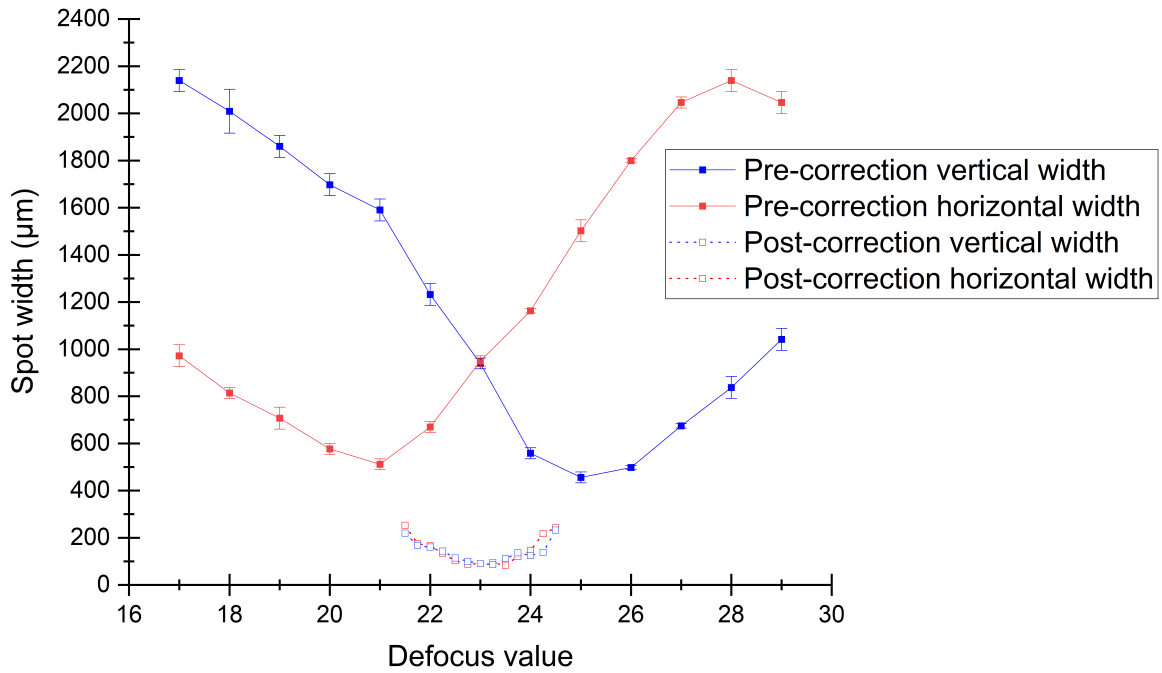


Figure 4.16: Variation of horizontal and vertical beam widths as a function of the defocus for a laser wavelength $\lambda = 632.8$ nm.

Zernike parameters and assess the image quality by maximising the peak intensity. Thus, I need to reduce the exposure time to ensure no saturation occurs. Figure 4.17 shows the peak intensities and the related amplitudes for each Zernike modes. The peak intensity corresponds to the value after the Zernike correction is applied.

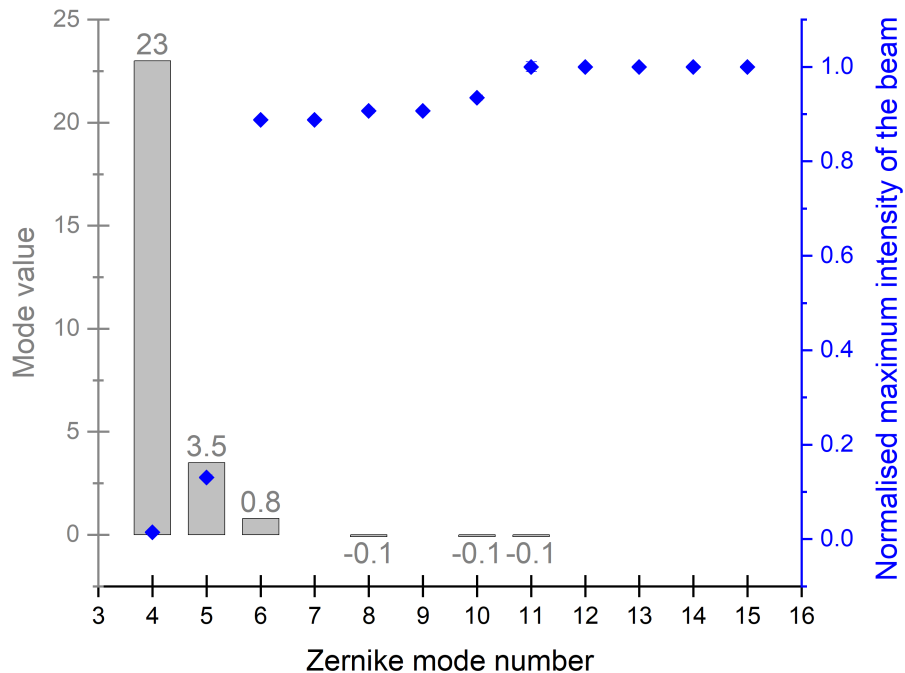


Figure 4.17: Amplitude of R5-R11 Zernike modes for which the intensity has been found maximum for the wavelength $\lambda = 632.8$ nm.

As expected, the vertical and horizontal astigmatism terms are the strongest, with the horizontal astigmatism being more important. This is to be expected as the DMD is off-axis on the horizontal plane. Most of the other aberrations don't play a role in the wavefront correction, however for the Zernike modes that do, they can be considered non negligible as the peak intensity has a 11% increase after the astigmatism is corrected.

4.3.3 Step 3: determination of R5 and R6 amplitudes

The third step is meant to determine the correct values of R5 and R6 amplitudes (horizontal and vertical astigmatisms). In the previous step, R5 and R6 have been found by looking at the maximum intensities. However this does not fully correct the astigmatism, but it does locate the range of values for R5 and R6 that improve the focal length position on the camera. To evaluate the astigmatism correction, a Gaussian fit is applied on the vertical and horizontal axis from the centre of the beam (see Fig. 4.18 with a Gaussian applied on the vertical axis). The standard deviations from these two Gaussian fits are then used to estimate the beam shape. When the widths are equal, the beam is circular.

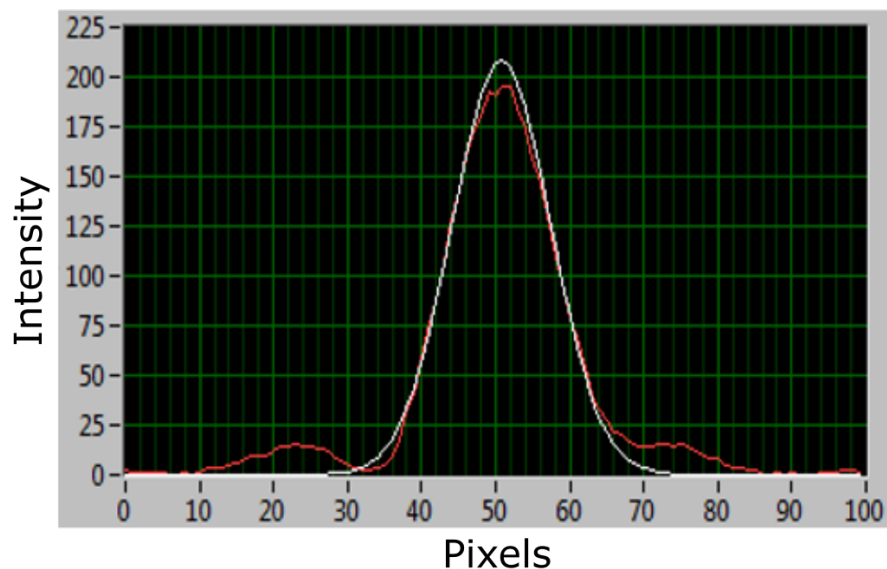


Figure 4.18: Vertical and horizontal Gaussian fit from the centre of the beam (pixel size = $4.65 \mu\text{m}$).

For this step, R5 and R6 amplitudes are first taken from the values in step 2. R5 amplitude is then varied when R6 amplitude is fixed and the pair with the smallest difference between the horizontal and vertical standard deviations is taken (see Fig.4.19). Then R5 amplitude is kept as found and fixed and R6 amplitude is varied until the smallest difference between the standard deviations is found again (see Fig.4.20) which indicates a circular beam. For both

graphs, the standard deviation is converted to the beam radius.

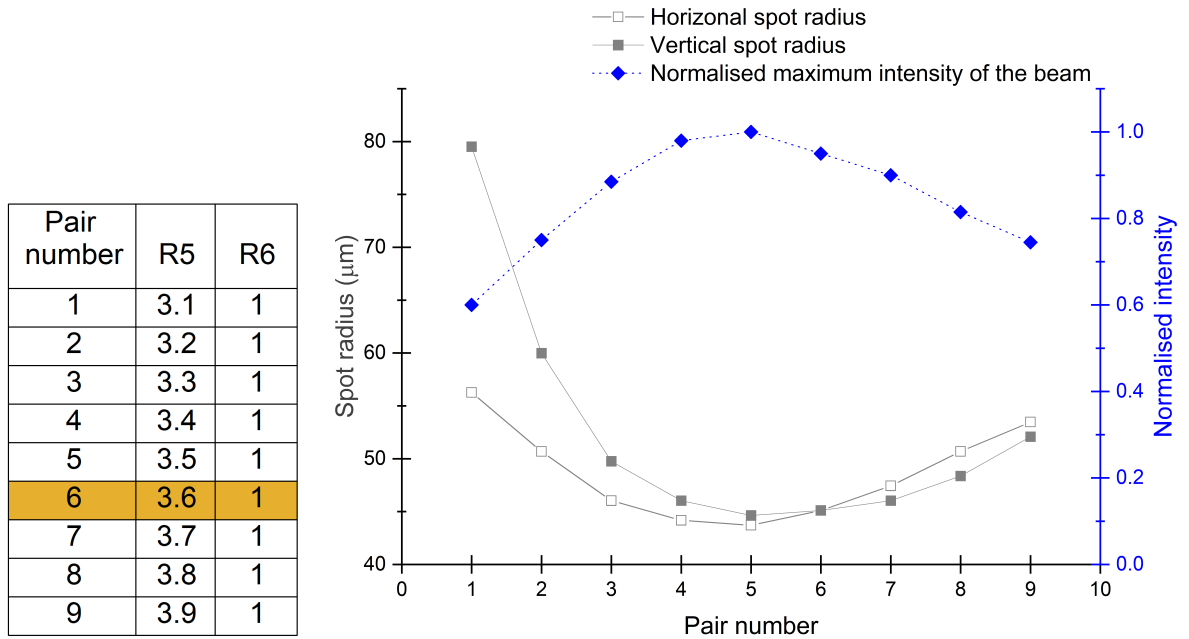


Figure 4.19: Variation of the horizontal astigmatism amplitude R5 while the vertical astigmatism amplitude R6 is fixed (left), evolution of the vertical and horizontal standard deviations as a function of the different R5/R6 pairs (right).

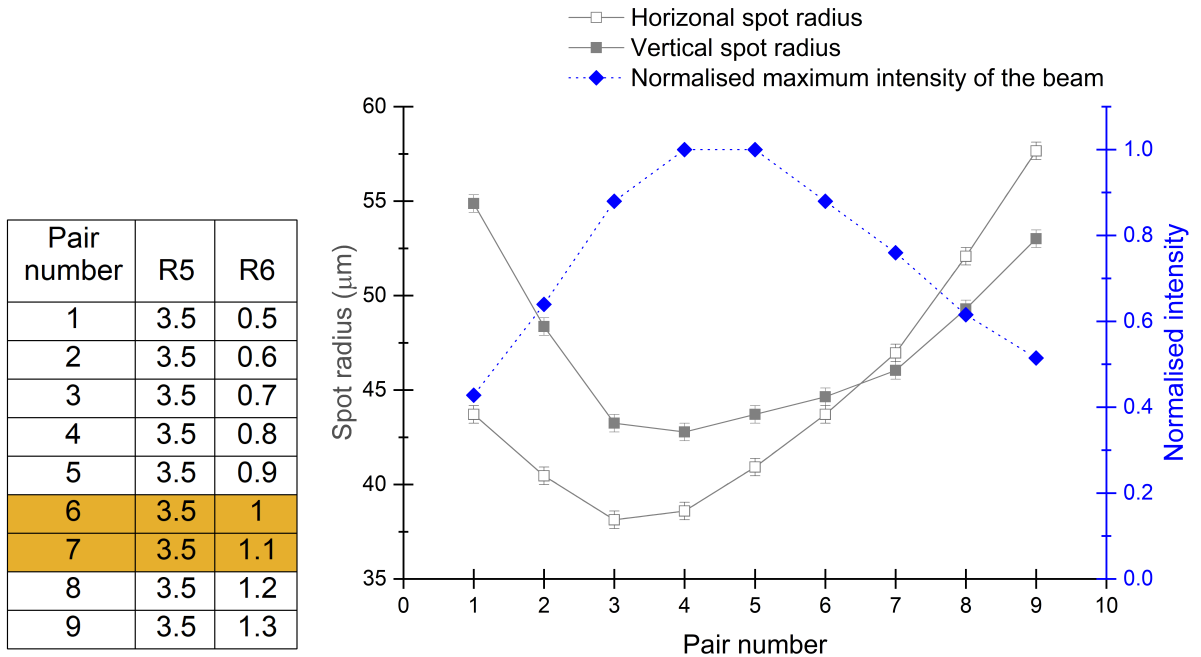


Figure 4.20: Variation of the vertical astigmatism amplitude R6 while the horizontal astigmatism amplitude R5 is fixed (left), evolution of the vertical and horizontal standard deviations as a function of the different R5/R6 pairs (right).

The most fitting pair is for $R5=3.6\pm 0.01\mu m$ and $R6=1\pm 0.01\mu m$. The amplitudes of all the Zernike polynomials are now defined to correct the astigmatism and to define the focal point on the camera. Images of the beam before and after correction are shown in figure 4.21. It can

be seen that the pre-correction focus is 10 times bigger than the post-correction focus. Next step is to look at the beam shape while varying the defocus.

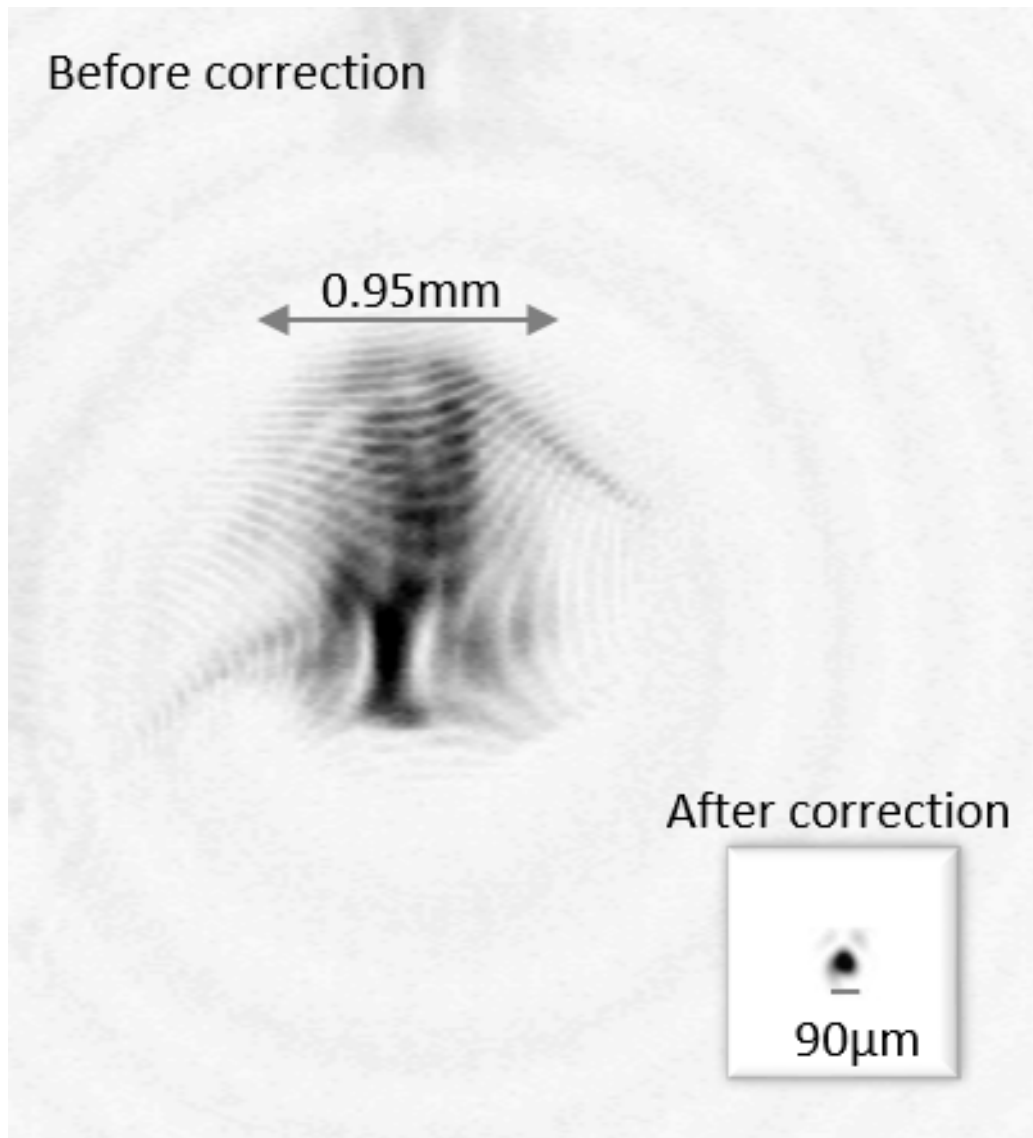


Figure 4.21: Initial beam and beam after correction at the focal point for the wavelength $\lambda = 632.8$ nm.

4.4 Results - wavelength characterization

4.4.1 Study of the beam waist as a function of the focal length

In this part, the behaviour of the beam after correction of the optical aberrations are summarized. The beam size as a function of the defocus is measured. Figure 4.22 (top) shows the evolution of the horizontal and vertical beam widths as a function of the defocus amplitude. Figure 4.22 (bottom) shows the RMS spot width, defined as $\sqrt{\frac{1}{2}(W_x^2 + W_y^2)}$ with W_x and W_y the horizontal and vertical beam widths that are derived from the horizontal standard devi-

ation σ_x and the vertical standard deviation σ_y ($W_{x/y} = 2 \times \sigma_{x/y} \times p_c$ with $p_c = 4.65 \mu m$ the size of the camera pixel).

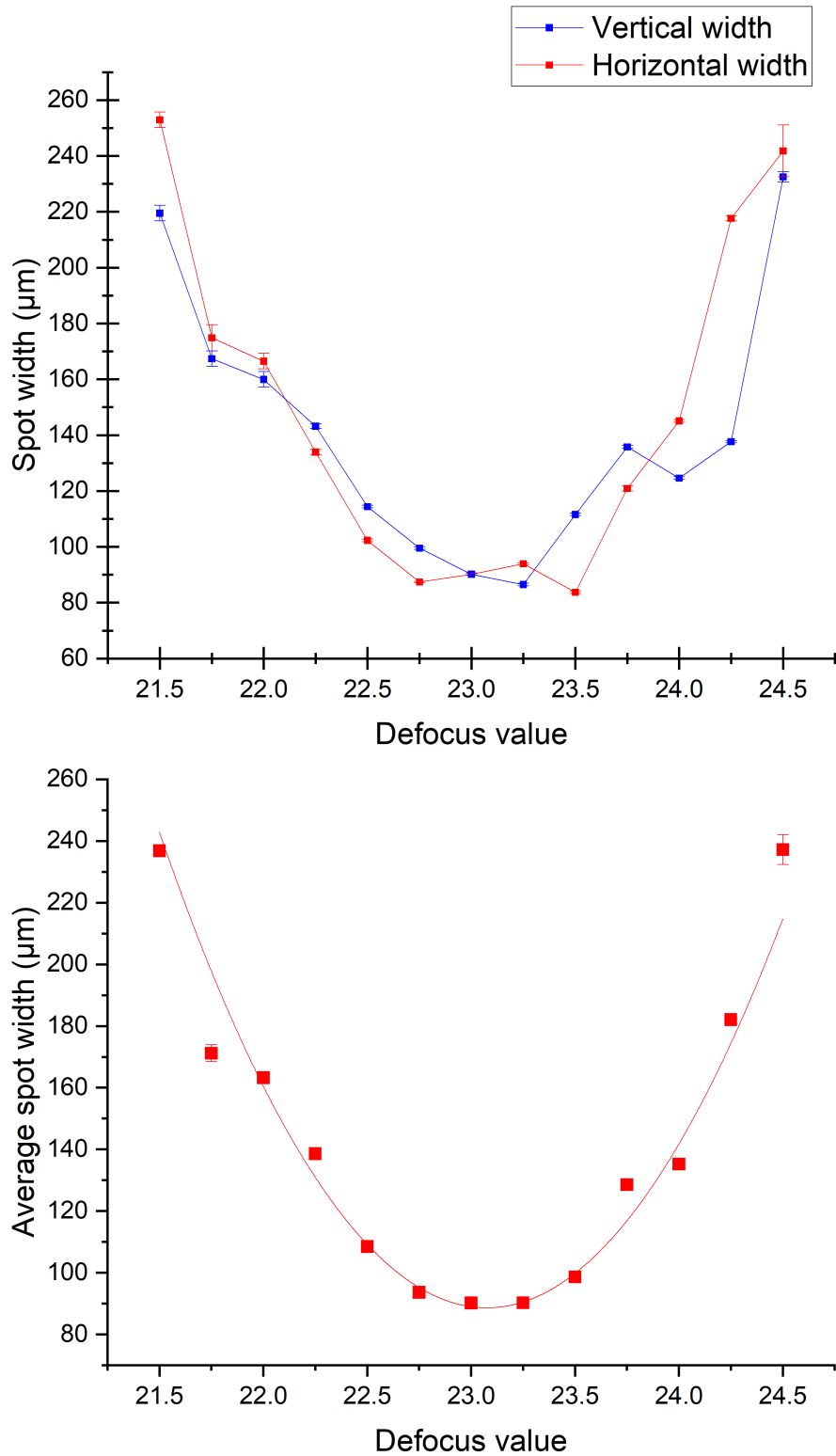


Figure 4.22: (top) Vertical and horizontal spot width as a function of the defocus value. (bottom) Average of both beam widths.

The focal point is determined to be for a defocus value of $R4=23.05 \pm 0.01$ at a wavelength

$\lambda = 632.8$ nm. The average spot width in term of the FZP focal length can also be illustrated as shown in figure 4.23 based on the conversion factor found in part 4.1.4.

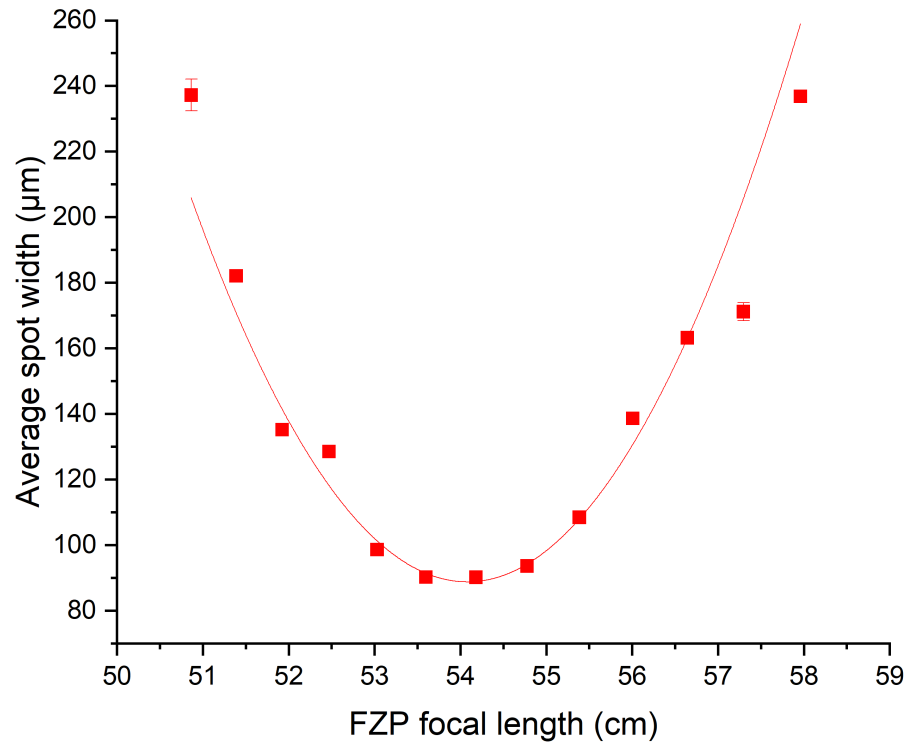


Figure 4.23: Average spot width as a function of the FZP focal length for a laser wavelength $\lambda = 632.8$ nm.

Moreover, Figure 4.22 gives a parabola around the focal point, which indicates a correction of the astigmatism if compared to the previous beam evolution (see figure 4.16). However, the figure also shows that some aberration is left close to the focal point as it is illustrated in figure 4.24. One of the reasons that can explain these leftover aberrations is that our algorithm is based on peak intensity measurement and as such doesn't always guarantee that the most fitting Zernike mode amplitude is found. Nevertheless, our corrective algorithm shows very promising results and a more in depth comparison with a theoretical model is shown in the next part.

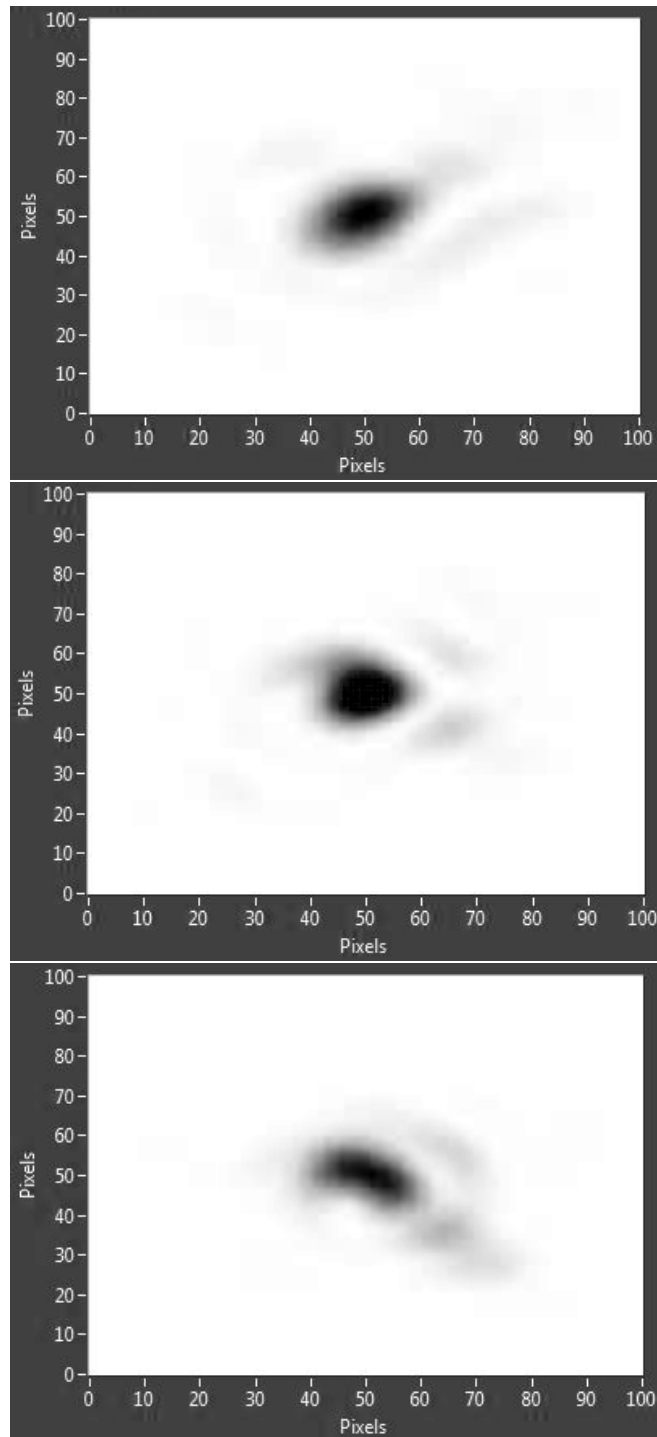


Figure 4.24: Evolution of the beam shape around the focal point at defocus values $R_4=22.6, 23$ and 23.4 .

4.5 Discussion - experimental beam waist determination

The previous results showed that the algorithm developed with the Zernike polynomials is able to improve the beam size at the focus. In this part, an analysis of the theoretical beam waist is added to check the validity of our results.

From Fig.4.22, the beam waist is measured at $44 \pm 0.1 \mu m$. This uncertainty is calculated based

on different measurements: the vertical and horizontal beam waists and their respective inaccuracy as well as the camera pixel size. The theoretical beam waist is given by:

$$\omega_0 = \frac{\lambda f}{\pi r_{max}} = 20.8 \pm 0.1 \mu m \quad (4.21)$$

The experimental beam waist is 2.1 times bigger than the diffraction limited beam waist for a wavelength of 632.8 nm. To add consistency to these results, the experiment is reproduced with two additional distances camera/DMD. First, at a distance camera/DMD equal to 30 ± 0.2 cm and then at a distance equal to 76 ± 0.2 cm. The new experiments give respectively 2.5 and 2.7 times the diffraction limited beam waist. The results are consistent over the different focal lengths. Moreover, compared to the paper [60] from 2018 which measured 6 times the diffraction limited beam waist for a focal length of 25 cm, these new results show that the experiment was reproduced and improved with the correction of some optical aberrations.

4.6 Conclusion

In this chapter, an algorithm in 3 steps was developed to correct the optical aberrations created by the DMD based laser detection system. Fifteen Zernike polynomials normalised on a rectangular surface were used to create the FZP pattern but also to correct those aberrations. I reproduced the experiment of Mohagheghian and Sabouri [60] and showed that the algorithm is working and does improve the beam shape at the focal point. Indeed, the analyse of the beam waist size gives better results when compared to the theoretical ones which would imply that the DMD aberrations, that would normally have impacted the focus, are partially corrected. The paper from Mohagheghian and Sabouri however did not explicit a wavelength resolution from their wavelength characterization, but in consequence to our correctional algorithm, an improved wavelength resolution should be expected. The wavelength resolution will be calculated more in details in the next chapter where several laser wavelengths will be studied with the DMD based detection system. Finally, the parabola found in figure 4.22 confirms that the major astigmatism has been corrected. However, some minor astigmatism is still present in the beam. This might be negligible for now as the results are still promising.

Chapter 5

Wavelength characterisation with the DMD based detection system

In this chapter, a single channel setup for the DMD system was implemented with the use of an optical fibre. Four laser wavelengths and one LED source are analysed. The algorithm developed in the previous chapter is used to characterise each laser and both rectangular and circular polynomial patterns are used to compare their efficiency. The use of the optical fibre would allow different lasers to have the same input channel and ensures consistent beam delivery to the DMD, which then would reduce the risk of additional aberrations when different wavelengths are compared. As a consequence of the use of the optical fibre, the field of view is restricted. However, this chapter is focused in the characterisation of wavelengths and the extension of the field of view for this system is to be researched in a future work. Moreover, this setup allows the use of two lasers simultaneously, with the condition that they both enter the camera frame – which is possible at a short camera-DMD distance, this is studied in details in the next chapter.

The aim of this chapter is to characterise laser wavelengths and to determine wavelength resolutions of the system as well as to highlight the laser discrimination principle behind the DMD based detection system with the use of a LED source on the system. The first part of this chapter summarizes the resolution of known laser detection systems that were studied in more details in chapter 2. This part also looks into the coherence characteristics behind the DMD technology when combined with a FZP pattern. In the second part, the new setup implemented is explained as well as the optical characteristics of the four lasers. In the third part, the characterisation of the four lasers is analysed and both types of polynomials

(circular and rectangular) are compared. In the final part, the LED is studied against a laser at equivalent wavelength and the laser discrimination principle behind the DMD is shown. A first set of results regarding this single channel setup was published in 2020 [122]. Another publication is under consideration.

5.1 Background study

5.1.1 Resolution of wavelength measurement systems

I have explored in the first chapter the different types of laser detection system and the wavelength resolution they can reach. I will now have a brief summary of the possible wavelength resolution from laser detection systems and compare them with other types of wavelength measurement systems.

In terms of the coherent detection systems, Fabry-Perot, Michelson and diffraction gratings based systems were able to reach a relative wavelength uncertainty of respectively 2×10^{-9} [49], 6.4×10^{-9} [55] and 10^{-5} [61]. However, other diffraction grating based systems were generally having an absolute wavelength accuracy of 10 nm or more [58, 41] which corresponds to around 2×10^{-2} in relative resolution. In terms of spectrum recognition systems, CW lasers were detected to an accuracy of 5 nm and up to 10 nm in outdoor conditions [3] so a relative uncertainty of respectively 8×10^{-3} and 2×10^{-2} .

Now, to have a more general idea of how good a resolution one system can achieve, I need to look at other wavelength measurement systems and their resolution [123]. An optical spectrum analyser can for example achieve a relative resolution of 10^{-6} [124] while optical beating methods can get down to 10^{-11} in relative accuracy. However, unlike the laser warning receivers previously mentioned, optical beating methods are restricted by the measuring range and correcting for this is extremely expensive. OSA systems are also highly expensive. To get in our price range, wavelength dependent material systems are more interesting. That includes use of the light polarization, optical fibres or photo-detectors and they achieve a relative resolution of 10^{-7} . Of course, all these wavelength measurement systems are not meant to discriminate laser light from background light and as such are not of interest for us. However, knowing resolution of different measurement systems is important in this case, as they can be compared to the newly developed system resolution.

5.1.2 Coherence properties of the DMD

One aspect behind the DMD combined with the FZP pattern that I have yet to study is the impact of different coherent sources on it and the total phase contribution from this system. Two different phase contributions are present in the system: the phase difference from each pixel at position (x,y) and the phase difference across each mirror. Benton studied the total phase contribution [62] and I will be here highlighting only the phase contribution across each mirror as this is the contribution that has a major impact in the difference of phase between the horizontal and vertical axis.

Let's consider the phase difference across each mirror, the initial problem is illustrated in figure 5.1 where two rays at opposite end of the DMD and their optical path difference are shown.

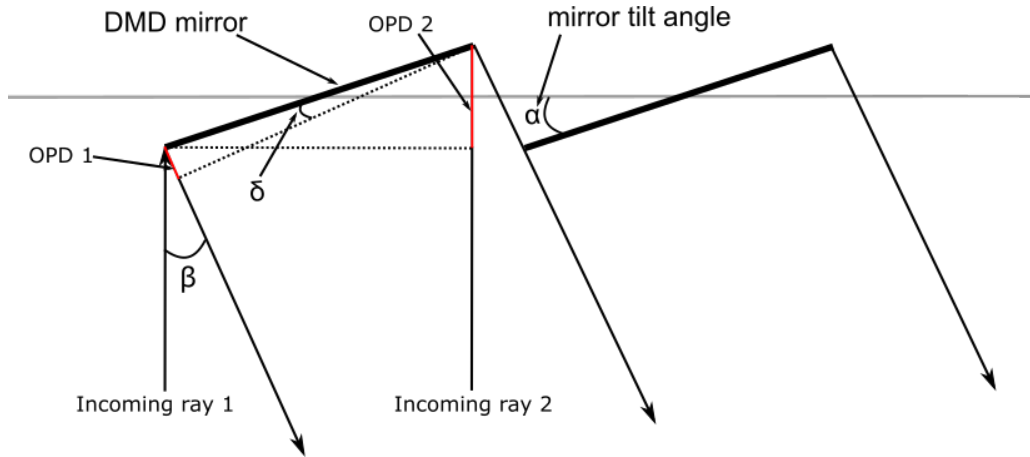


Figure 5.1: Path difference between two rays across one mirror.

With w the DMD mirror width, the optical path difference between two rays at the opposite end of the mirror can be expressed as:

$$OM = OPD2 - OPD1 = w \sin \alpha - w \sin \delta \quad (5.1)$$

Where δ and α are defined as in figure 5.1.

Moreover, with trigonometry and the intercept theorem, we find that:

$$\delta = \beta - \alpha \quad (5.2)$$

β is the angle between the incoming ray and the outgoing ray and is relatively the same for rays across the mirror (the difference is negligible for a mirror as the focal length $F \gg w$) but β

changes with the mirror position on the DMD as the DMD pattern focuses light towards the focal point P.

Using geometry from figure 5.2, the angle β can be written as:

$$\beta(x) = \arctan \left[\frac{f \sin \chi - x}{f \cos \chi} \right] \quad (5.3)$$

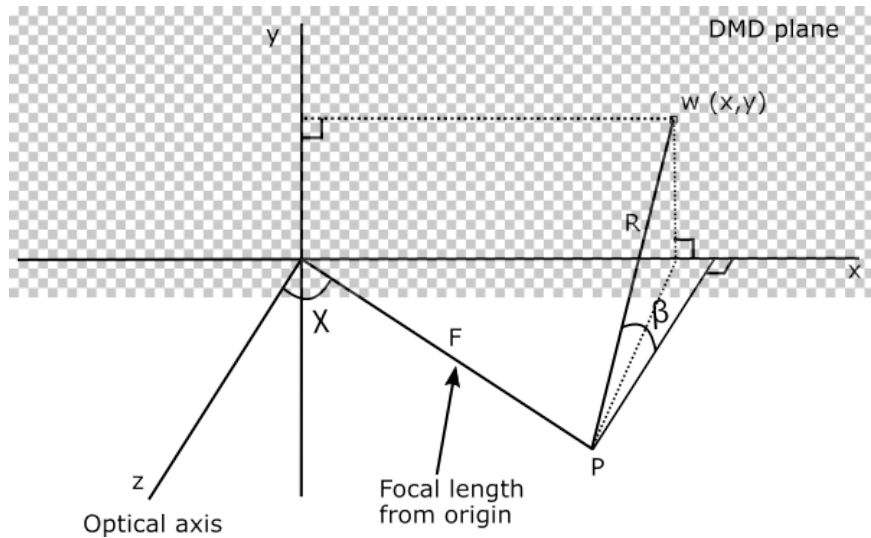


Figure 5.2: Geometry of a DMD mirror focussing light at a point P at an angle χ to the optical axis.

Thus, the optical path difference across each mirror is written as:

$$\phi_m = \frac{2\pi}{\lambda} w (\sin(\alpha) - \sin(\beta(x) - \alpha)) \quad (5.4)$$

Inserting formula 5.3 in equation 5.1 and then in equation 5.2, we can calculate the optical path difference OM across one mirror. With a mirror width of $w = 13.68\mu\text{m}$, a mirror tilt angle of $\alpha = 12^\circ$, an angle $\chi = 2\alpha$ when the incoming light is at normal incidence, a focal length of 46 cm and a DMD dimension of 768 pixels for the circular polynomials, the optical path difference across one mirror is equal to $5.6\mu\text{m}$ or around 9 wavelengths at 633 nm. It implies that over a certain amount of mirrors, the path difference can become so important that it will not allow interference for low coherent sources. However, this is only true on the axis where the mirrors are tilted (the horizontal axis for us), as the tilt creates the additional optical path difference. On the vertical plane, the mirrors are not tilted in this direction ($\alpha = 0^\circ$) and as such the path difference across mirrors is negligible.

For the vertical plane, let's consider the FZP first ring radius R_0 . The path difference at the first ring radius is equal to $\lambda/2$ and the FZP formula gives us the first ring radius R_0 for the

HeNe laser at a focal length $f = 46\text{cm}$ at : $R_0 = \sqrt{\lambda f} = \sqrt{0.46 * 633 * 10^{-9}} = 540\mu\text{m}$. This corresponds to 39 pixels. So it gives the path difference for each pixel at around $\lambda/78 = 8\text{nm}$. So, to obtain the same path length difference in the vertical and horizontal directions, the vertical plane requires 700 mirrors while the horizontal plane requires only 1 mirror. This is due to the DMD behaving as both a blazed diffraction grating and a focusing lens. Thus, the DMD based detection system is actually a differential coherence system, implying that some low coherent sources might focus well on the vertical axis, but won't interfere well in the horizontal plane. This will be highlighted in part 5.4.1 where the horizontal and vertical beam widths as a function of the focal length for four lasers are studied, the difference in widths for low coherent sources (blue and green laser) would imply the beam is elliptical and thus would confirm a differential coherence system. This will also be discussed in part 5.4.2 with the study of a LED source (low coherence) against a HeNe laser (high coherence).

5.2 Single channel for the DMD based laser detection system

5.2.1 Implementation of the single channel system

The system involves the use of an optical fibre, two mirrors and a focusing lens. The laser is focussed into an optical fibre and then direct towards the DMD. A beam splitter is added to allow the use of two wavelengths simultaneously however in this chapter, only one laser is turned on at a time for a consistent analysis of the results. Figure 5.3 illustrates the setup of the single channel system. The camera-DMD distance is at 46cm. The single mode fibre used is a SM600 patch cable for 633-780nm.

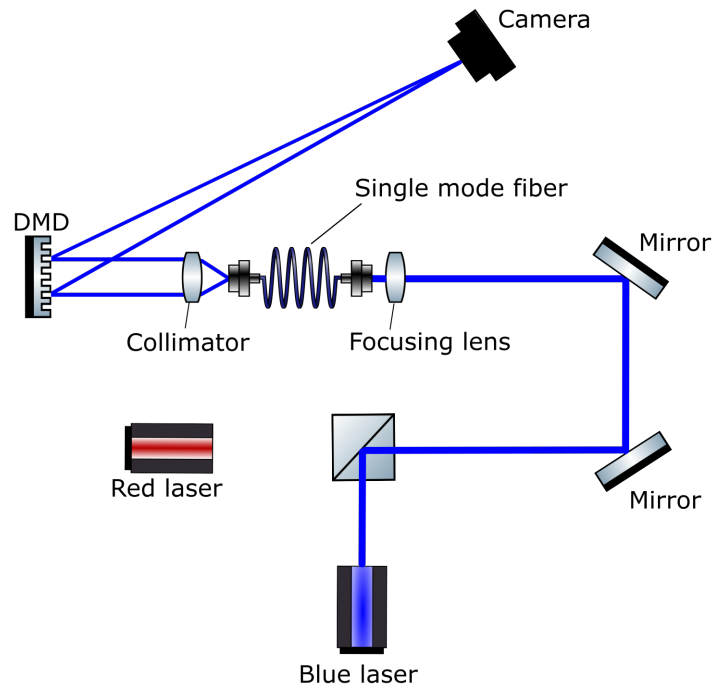


Figure 5.3: Single channel setup for the DMD based laser detection system.

In this chapter, four different wavelengths are characterized (405 nm, 532 nm, 633 nm and 760 nm) and the possible difference between two surface types of Zernike polynomials is analysed. The two surface types of Zernike polynomials are those normalised on a rectangular surface and the ones normalised on a circular surface, named respectively rectangular polynomials and circular polynomials for simplification. For the circular polynomials, the DMD surface has been programmed to be circular and at a radius of 384 pixels, thus the pattern is smaller for the circular polynomials than for the rectangular polynomials. The rectangular polynomials pattern has a radius of 640 pixels as it uses the whole DMD surface. Due to the lack of online information on rectangular Zernike, only 15 modes are used while 40 modes are used for the circular Zernike. However, mainly the first 11 modes are useful as it was found in the previous chapter so it can be assumed that the additional modes will not have a noticeable impact on the aberration correction.

5.2.2 Optical characteristics of the four lasers

Four different lasers are used with this setup:

- a green laser diode (CPS532) at 532 nm and power at 4 mW;
- a blue laser diode (CPS405) at 405 nm and power at 4 mW;

- a red HeNe laser (HNLS008L-EC) at 632.8 nm and power at 0.8 mW.
- a red DFB Single Mode laser (RLS/EP760) at 760 nm and power at 2.5 mW

Three of the four laser beams exiting the single mode fibre are shown individually in figure 5.4.

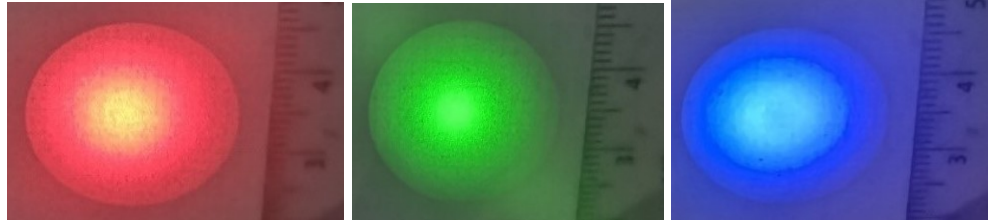


Figure 5.4: 633 nm, 532 nm and 405 nm laser beams exiting the single mode fibre.

The diameter for the beams, around 2.5cm, is bigger than the DMD diagonal, around 1.8cm: each laser beam covers the whole DMD detection area so the lens radius size considered for our experiment will depend on the DMD surface size only; this will be interesting when the diffraction limited beam size will be calculated in this chapter.

Each of these lasers has a different spectral bandwidth, the DFB laser has the highest spectral purity and its coherence length is estimated at around 66 m. The HeNe laser has the second largest coherence length at typically 10-30cm. The blue and green laser diodes have the worst spectral bandwidths and their typical spectra is illustrated in figure 5.5.

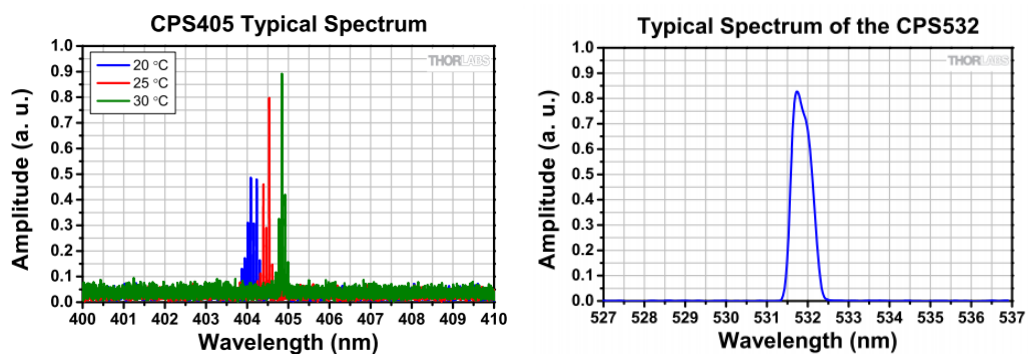


Figure 5.5: Typical spectrum of the CPS405[125] and CPS532[126] diode lasers.

A major difference can be seen on these two laser diodes, the blue laser has an important temperature dependency and its wavelength varies widely depending on it. This is an important characteristic that will be helpful in our results and analysis section. On the other hand, the green laser is not impacted by temperature variation however it has a typical bandwidth of 0.6 nm, or a coherence length of 0.2 mm.

The algorithm developed in chapter 4 is used to correct the beam shape and results in a

smaller and more circular focus spots for each wavelength. The average spot radius is studied as a function of the defocus amplitude, for both the rectangular and circular polynomials. The average spot radius is calculated as in subsection 4.4.1 and is based on the vertical and horizontal standard deviation of the beam on camera.

5.3 Experimental results

5.3.1 Beam size and defocus amplitude comparison for circular and rectangular polynomials at each laser wavelength

The graph showing the average measured beam radius as a function of the defocus amplitude is shown in figure 5.6. In this graph, the circular and rectangular polynomials are named respectively rect and circ for simplification.

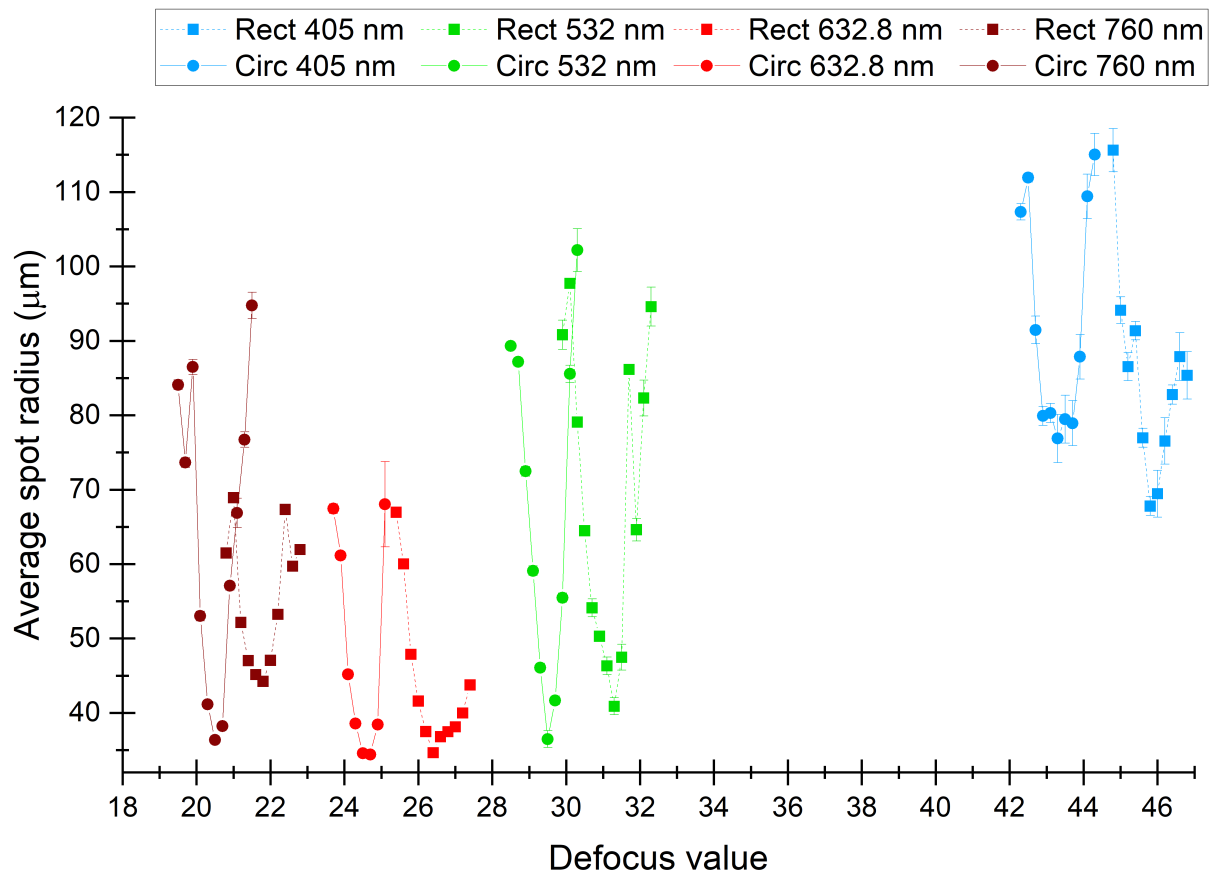


Figure 5.6: Evolution of the beam size as a function of the defocus value for circular and rectangular polynomials at each laser wavelength.

A first look at these results clears out two major aspects of this experiment. First, concerning the spot radius, the blue laser beam size is notably bigger than the other wavelengths. As

mentioned in part 5.2.2, the blue laser has the worst spectral bandwidth among our lasers with an important temperature dependency and as such, the beam measurements would be impacted. The large uncertainty measurements at each defocus amplitude for the blue laser compared to the other lasers also gives reason to this explanation. Secondly, the defocus value is clearly different for each wavelength, which implies that laser wavelengths can be characterised easily with this experiment.

Moreover, the defocus value can be converted as the FZP focal length with the use of equation 4.17 and 4.19 for respectively the circular and the rectangular polynomials. Figure 5.7 has one graph for each wavelength and each graph gathers the data for the two different types of Zernike surface polynomials.

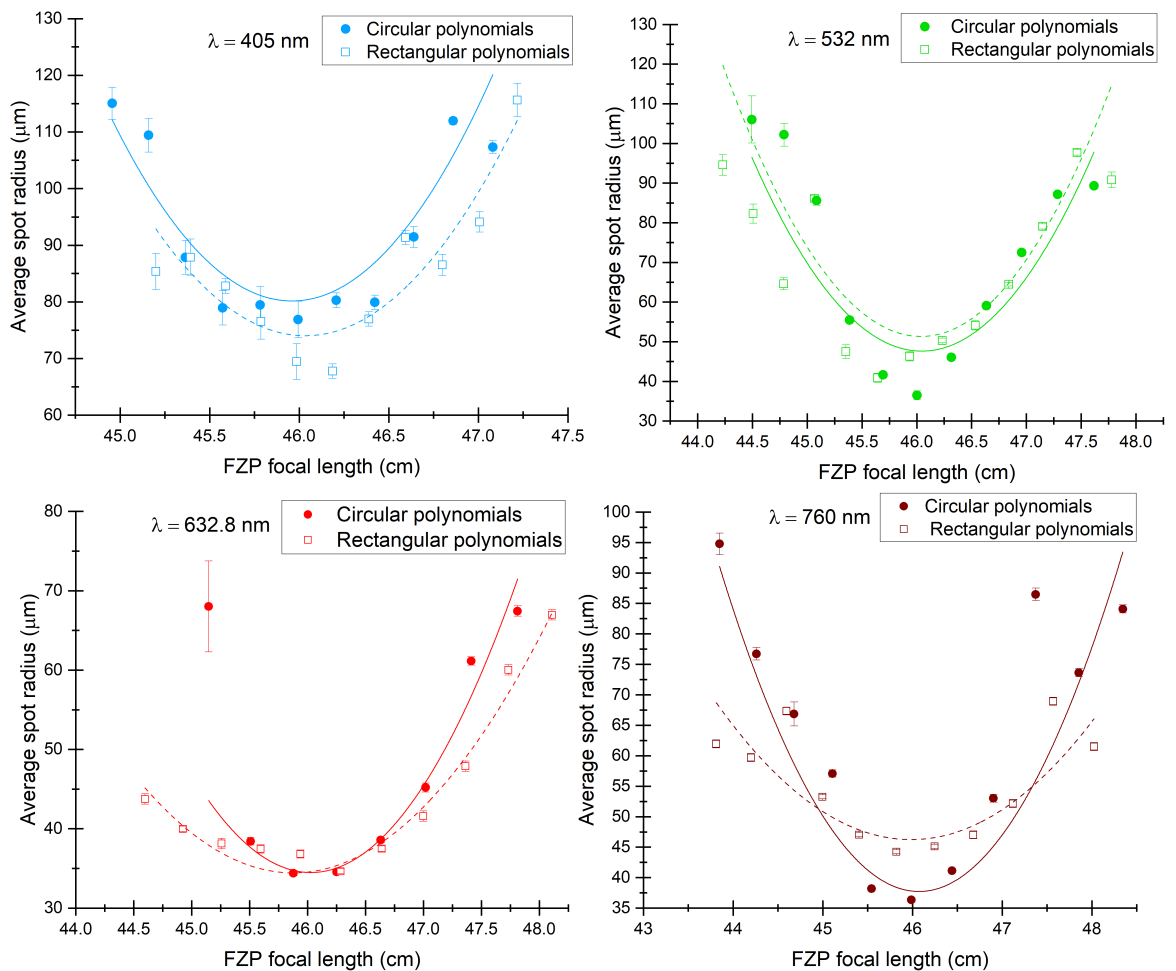


Figure 5.7: Evolution of the beam size as a function of the FZP focal length for the circular and rectangular Zernike types.

The beam waist will be studied in part 5.3.2, in here I am interested at the shape of the evolution of the beam size in term of the FZP focal length. If I model the evolution of a

Gaussian beam size for both Zernike surface types based on the following equation:

$$\omega(z) = \omega_0 \sqrt{1 + \left(\frac{z}{z_R}\right)^2} \quad (5.5)$$

With the Rayleigh distance $z_R = \frac{\pi\omega_0^2}{\lambda}$ and the beam waist radius $\omega_0 = \frac{\lambda f}{\pi r_{max}}$, $f=46$ cm is the focal length, λ the wavelength, and r_{max} the radius of the DMD for which the polynomials are written on. I find out that the beam size evolution for the rectangular polynomials has a larger curvature than the circular polynomials' evolution as r_{max} is smaller for the circular polynomials. However, on our graphs, the curvature of the circular and rectangular polynomials are similar for both the blue and the green lasers. This can be explained again by their large spectral bandwidth since the wavelength impacts the focal length, their curvature would be the least predictable. On the other hand, for the red lasers at 633 nm and 760 nm, the curvature for the two circular and rectangular polynomials slopes are different. Their spectral bandwidth was shown to be the purest so seeing a distinction between the two slopes is a good indicator. However, the rectangular polynomials for both lasers have a slowest slope than for the circular polynomials and this goes against what would be expected. This result is mostly due to the size difference between the two circular and rectangular FZP patterns. One pattern uses the whole DMD window (rectangular polynomials) while the other uses only a restricted area (circular polynomials). As could be seen from figure 4.13 in chapter 4, the DMD window creates important aberrations at the border, which indicates that the rectangular polynomials would intrinsically have more aberrations to correct than the circular polynomials. Thus, the evolution of the size would be impacted by it.

To get into a more detailed study, a second order polynomial fit is applied to each plot of figure 5.6. Two important pieces of information is then extracted: the circle of least confusion and the corresponding defocus amplitude. A comparison of experimental and theoretical values of the beam waist is illustrated in table 5.1 as well as the corresponding defocus value. The diffraction limited beam waist is calculated based on equation 4.21 where r is the radius of the DMD surface for which the spot lights reflect on, r is equal to 384 pixels for the circular polynomials and 640 pixels for the rectangular polynomials.

From table 5.1, two elements can be studied and this will be looked into in the two next sections. First, the beam waist for different wavelengths for both types of polynomials is studied. Then, the accuracy on the wavelength characterization is looked at.

Table 5.1: Comparison of experimental and theoretical values of defocus value and beam waist with wavelengths at 405 nm, 532 nm, 632.8 nm and 760 nm for the circular and rectangular polynomials at a focal length of 46 cm.

Wavelength	Circular polynomials			
	405 nm	532 nm	632.8 nm	760 nm
Defocus value	43.34±0.25	29.48±0.11	24.62±0.09	20.49±0.06
Experimental beam waist $\omega_{0,exp}$ (in μm)	79.7±2.3	47.1±0.6	34.3±0.3	37.7±0.2
Diffraction limited beam waist $\omega_{0,theory}$ ($\pm 0.1\mu m$)	11.3	14.8	17.6	21.2
$\omega_{0,exp} / \omega_{0,theory}$	7.1	3.2	1.9	1.8

Wavelength	Rectangular polynomials			
	405 nm	532 nm	632.8 nm	760 nm
Defocus value	45.96±0.26	31.05±0.16	26.65±0.13	21.75±0.13
Experimental beam waist $\omega_{0,exp}$ (in μm)	73.8±1.9	51.1±1.2	34.2±0.3	46.4±0.3
Diffraction limited beam waist $\omega_{0,theory}$ ($\pm 0.1\mu m$)	6.8	8.9	10.6	12.7
$\omega_{0,exp} / \omega_{0,theory}$	10.9	5.7	3.2	3.6

5.3.2 Evolution of beam waist with wavelength

The evolution of the beam waist as a function of the wavelength can be analysed based on table 5.1 and it is plotted in figure 5.8.

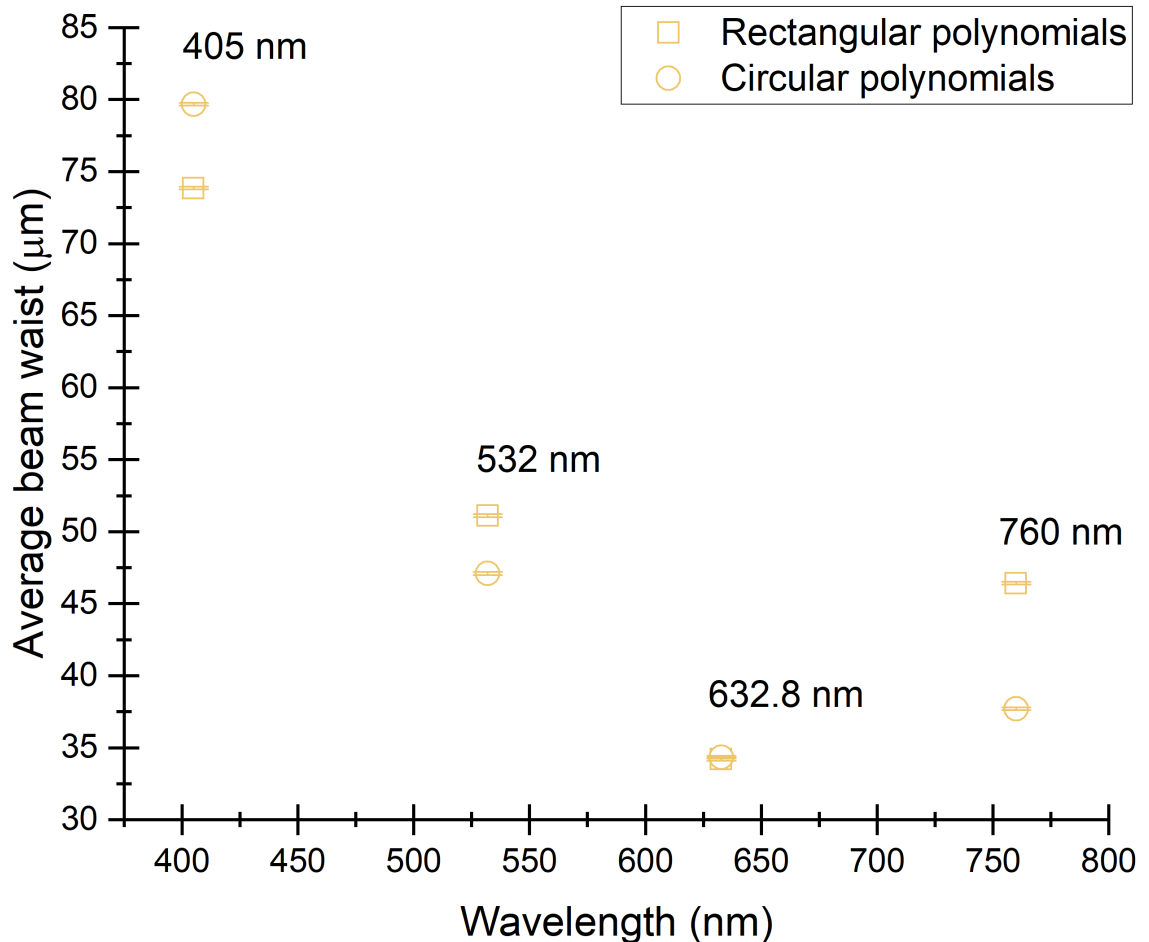


Figure 5.8: Evolution of the beam size as a function of wavelength for the circular and rectangular Zernike types.

The radius of the circle of least confusion for the circular polynomials is smaller than for the rectangular polynomials for most lasers except the 405 nm laser. As explained before, the behaviour of the blue laser is the least predictable as the temperature impacts its wavelength and thus the beam size. So in regards to the beam size comparison between the two different polynomials types, the blue laser can be ignored. However, for the three other lasers, the circular polynomials perform better. This is explained as the circular polynomials are written on a smaller DMD surface than the rectangular polynomials, so some of the aberrations caused by the DMD window at the border do not appear with the circular modes and thus the beam arriving on the camera is less aberrated for the circular polynomials.

Moreover, if we compare the diffraction limited beam waist with the experimental beam waist

for both circular and rectangular polynomials, the 633 nm and 760 nm laser performs better in both cases (circular and rectangular): their experimental beam waist is around 2 times their diffraction limited beam waist for the circular polynomials and around 3 times for the rectangular polynomials. The 532 nm laser follows behind with a factor 3 for the circular polynomials and around 6 for the rectangular polynomials. And finally the blue laser with a factor 7 for the circular polynomials and around 11 for the rectangular polynomials. To explain these results, I need to look at the spectral bandwidth of each laser again. Each laser ability to focus is depending on the purity of their spectral bandwidth as the FZP focuses light at a specific focal length related to the light wavelength. So, knowing that the two red lasers had the purest spectral bandwidth, these results agree with the expected behaviour between the four different wavelengths.

Overall, these two Zernike surface modes can both be interesting to use on the DMD depending on the application of the system one wants. If a good sensitivity is demanded, then the circular modes are to be prioritized. However, the rectangular polynomials are still performing well in term of the focusing ability and they can be interesting to use. More specifically, if the rectangular polynomials is used then all of the DMD window space will be taken advantage of, unlike with the circular polynomials. Another important aspect to consider before one can decide to use the rectangular over the circular polynomials however, is the wavelength accuracy for each wavelength. This is discussed in the following session.

5.3.3 Wavelength characterization and resolution

In this part, first, the evolution of the defocus amplitude is studied as a function of the wavelength. Figure 5.9 shows this evolution. A second order polynomial is used to fit the two sets of data.

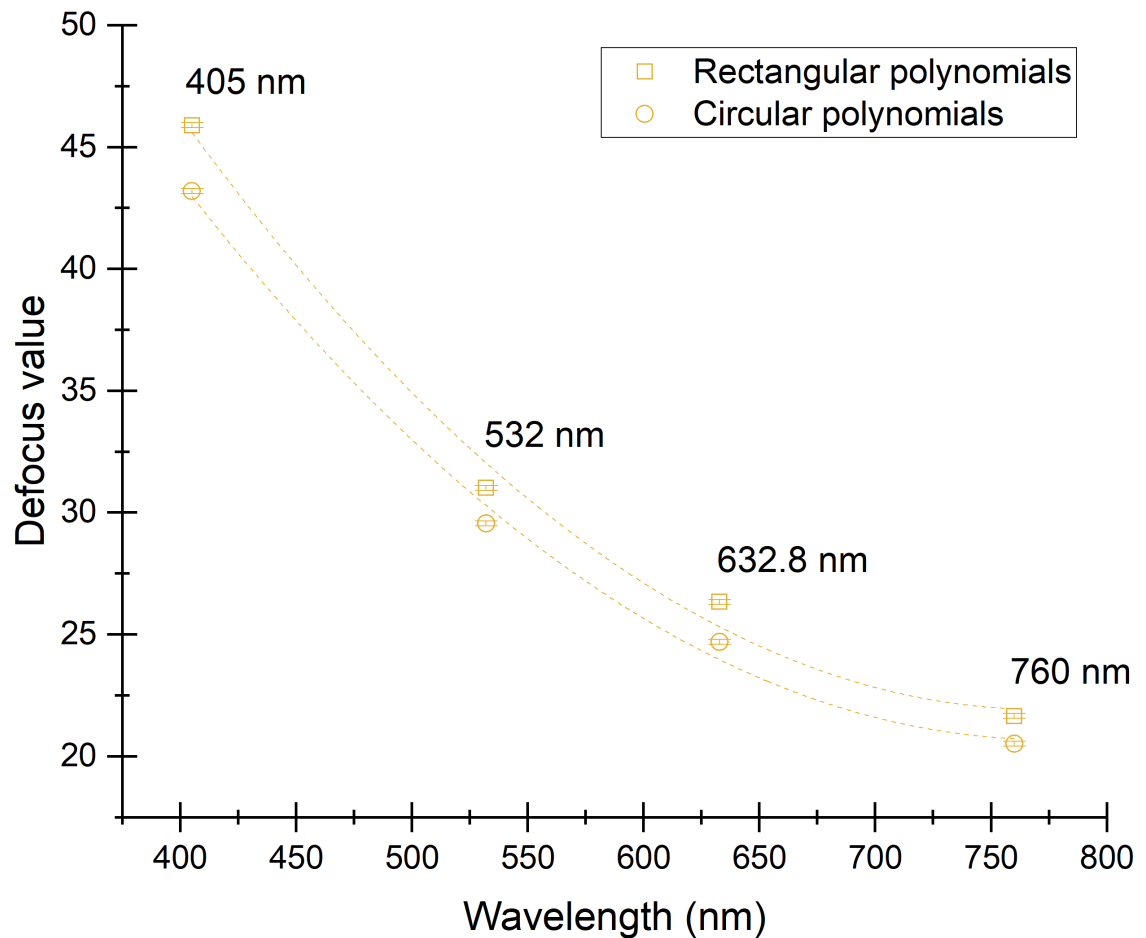


Figure 5.9: Evolution of the defocus amplitude as a function of wavelength for the circular and rectangular Zernike types.

Both fitting functions have an R^2 over 0.99. This graph implies that once the defocus amplitude is known from the experimental algorithm, the input wavelength can then be characterised. Now, an important criteria that can be extracted from this graph is the system wavelength resolution, i.e the confidence interval of the wavelength measurement. For these measurements, the confidence interval of the defocus value is used. The confidence interval of the defocus value is estimated from the confidence interval of the beam waist which itself is measured on LabView from the variation of the standard deviation associated with the two Gaussian fits. Based on the confidence interval of the defocus value, the confidence interval for each wavelength can be estimated by using a derivation of equations 4.17 and 4.19 for respectively the circular and rectangular polynomials. These accuracy measurements are gathered in table 5.2.

A clear difference can be seen between the circular and rectangular polynomials for the wavelength resolution. As stated in part 5.3.2, this difference can be explained from the pattern size on the DMD window and the additional presence of aberration in the rectangular

Table 5.2: Wavelength resolutions of the DMD based detection system for the circular and rectangular polynomials.

Laser wavelength (nm)	405	532	632.8	760
Absolute resolution with the circular polynomials (nm)	2.3	1.9	2.2	2.1
Relative resolution with the circular polynomials	5.7×10^{-3}	3.6×10^{-3}	3.5×10^{-3}	2.8×10^{-3}
Absolute resolution with the rectangular polynomials (nm)	2.3	2.7	3	4.4
Relative resolution with the rectangular polynomials	5.7×10^{-3}	5.1×10^{-3}	4.7×10^{-3}	5.8×10^{-3}

polynomials case. However, overall the relative wavelength resolution is found to be at around 10^{-3} . Compared to most of the laser detection systems based on diffraction grating, our system achieves better results. Indeed, previous systems have shown absolute resolution of 10 nm at best while the DMD system is able to get down to 2 nm for the circular polynomials. However, this statement is not true for this technology also using the DMD with a FZP pattern [60]. They achieved a relative resolution of 10^{-5} with a HeNe laser. The main difference with our situation is that their relative resolution is different than the one I measure. Their relative uncertainty is based on a repetition of measurement and the standard deviation associated with them. For a large number of measurements their repetition accuracy is good, but this is not the resolution or the accuracy with which they could determine an unknown wavelength. What I am assessing is the uncertainty with which an unknown wavelength could be identified, not a well known one. They use the laser input as an unknown value and estimate its value with the FZP focal length evolution around the focus. In my case, I am using Zernike polynomials to draw the FZP pattern and I chose the laser as a known value and estimate the relative resolution based on the accuracy around the defocus value.

Moreover, even if the rectangular polynomials achieved an overall worse resolution, it is actually still very promising with an absolute resolution of around 3-4 nm. This result is significant, it implies that the rectangular polynomials can be used over the circular polynomials if one needs to use the whole surface of the DMD for a specific application that requires it.

5.4 Study of different coherent sources on the DMD based detection system

In this second experimental part, I look at how different spectral bandwidths are impacted by the DMD based detection system.

5.4.1 Impact of the four laser spectral bandwidths in the system

As mentioned in the previous parts of this chapter, the difference of spectral widths between the four lasers is important enough and should be detectable by our system. Figure 5.6 showed the average beam size evolution around the focal point however, I now need to look at the beam widths in the vertical and horizontal directions to see if the beams are overall circular or not. As no significant difference was seen for the beam width difference between the rectangular and circular Zernike surface types, I show only the results for the circular surface types for simplicity. Figure 5.10 illustrates the vertical and horizontal beam widths as a function of the FZP focal length for the 4 lasers. It can be seen from figure 5.10 that the two red lasers have an overall similar widths in the vertical and horizontal directions. This implies that the beam was circular along the optical axis. However, the green and blue lasers show a major difference in the two directions. Indeed, for both lasers, the beam width in the horizontal direction is wider than in the vertical direction. This is an interesting result, as these two lasers have the largest spectral bandwidth with a coherence length less than 1 mm. This shows that the DMD based laser detection is indeed a differential coherent system as was discussed in part 5.1.2 and that low coherent sources are detected by our system. To confirm these results, the impact of a LED source on the system is studied in the next part.

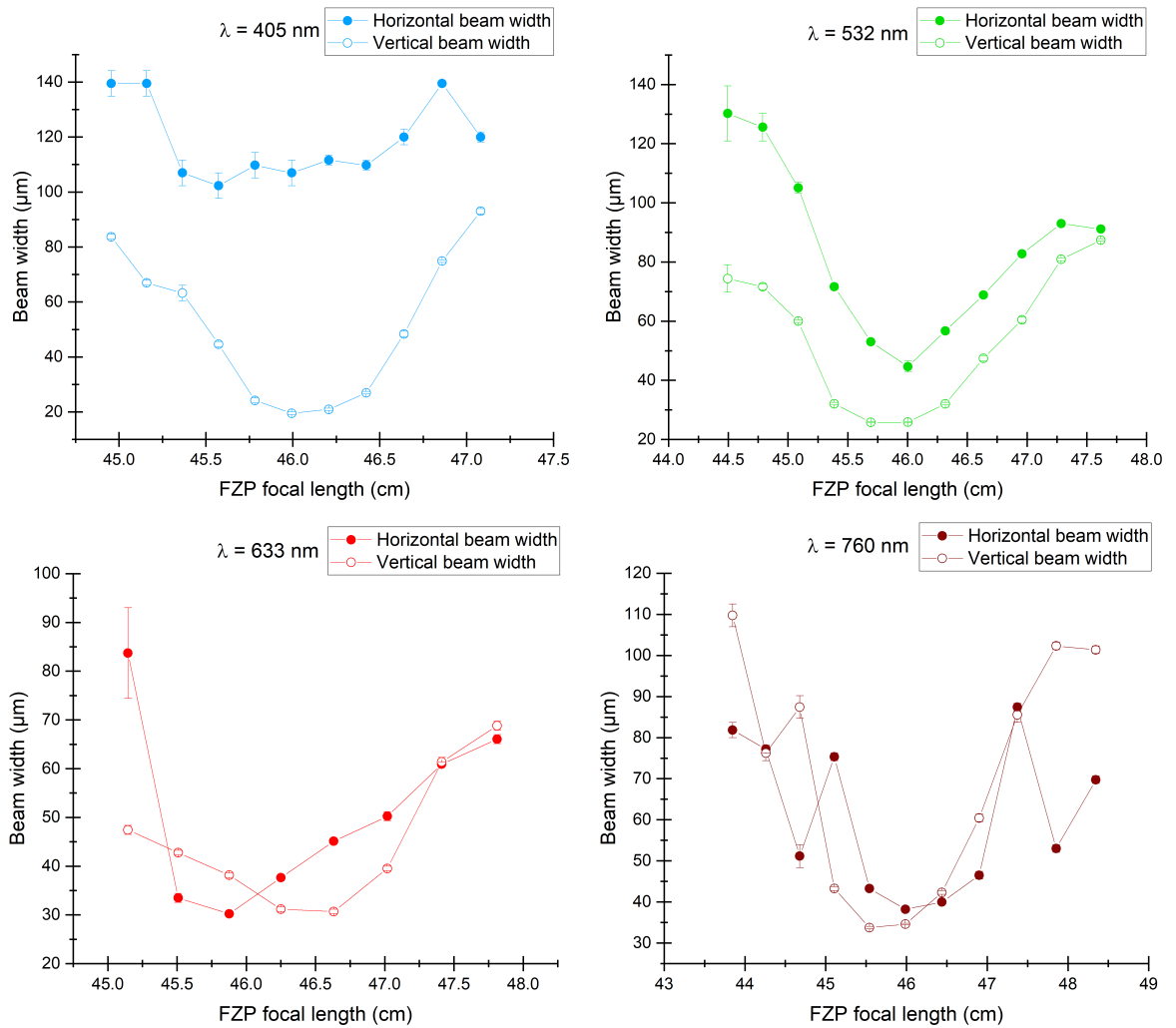


Figure 5.10: Comparison of the vertical and horizontal beam widths for 4 wavelengths at 405, 533, 633 and 760 nm for the circular polynomials.

5.4.2 Comparison between the HeNe laser and an LED around the focal point

In this part, a LED source behaviour is studied against the HeNe laser source with the circular polynomials pattern on the DMD. Both the HeNe laser and the LED have equivalent wavelength. The first set of data gathered in figure 5.11 corresponds to the HeNe beam on camera while the defocus amplitude is varied.

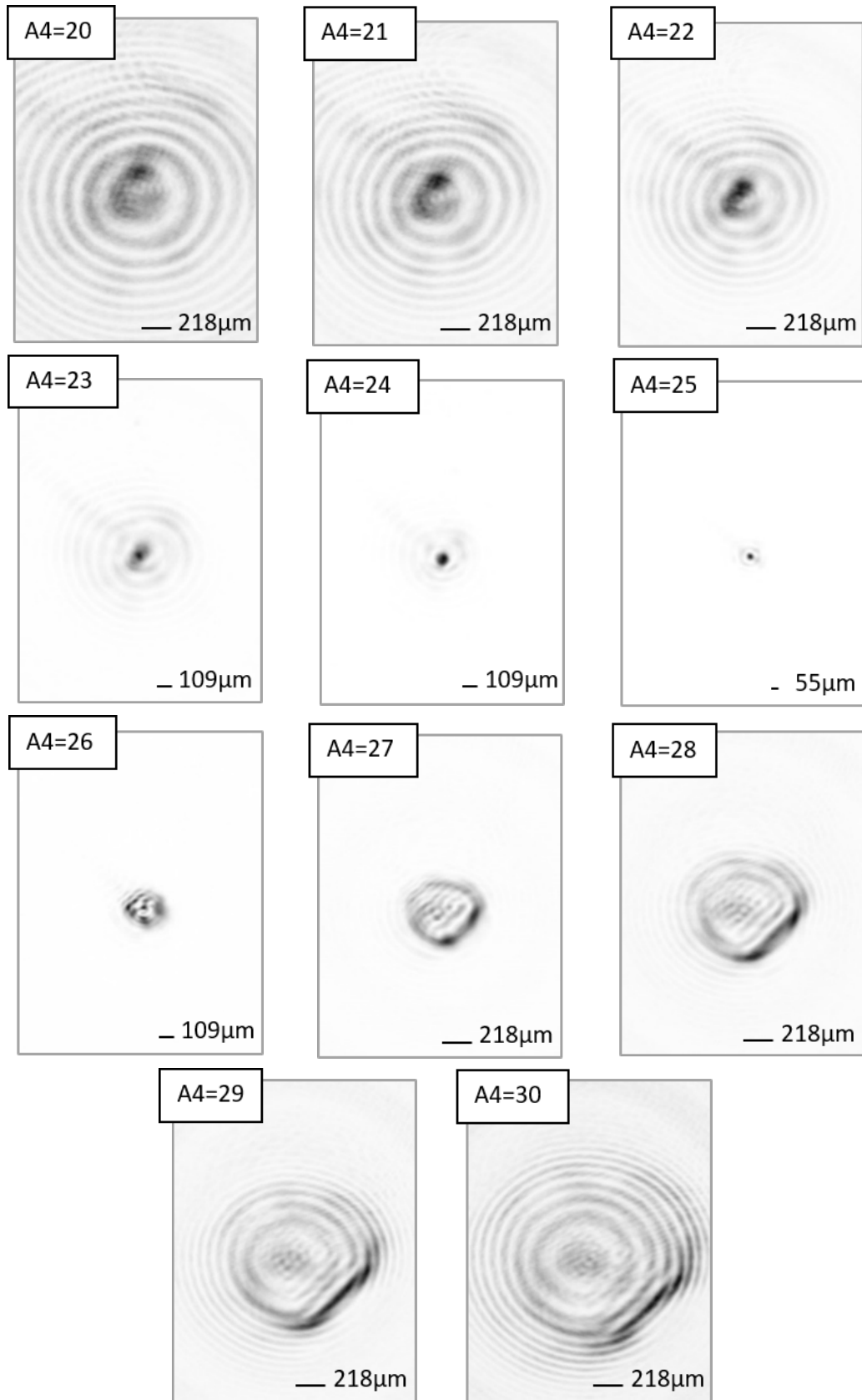


Figure 5.11: Evolution of the HeNe laser beam around the focal point.

The HeNe beam is acting as expected from a focusing lens, the beam size is decreasing around the focal point ($70 \mu\text{m}$ at $A4=25$) and increasing when getting away (around $400 \mu\text{m}$ at $A4=20$).

However, out of focus, the FZP pattern becomes too noticeable against the focus spot to separate them. As such, the measurement of the beam size becomes difficult when the beam is too far away from the focus thus the restrictions of our measurements to few centimetres only around the focal point. Nevertheless, this doesn't modify our findings, it only restricts the evolution of the beam size to a certain range.

Let's now look at the impact of a LED source on the system. The LED has a 617 nm nominal wavelength and a coherence length of $38 \mu\text{m}$.

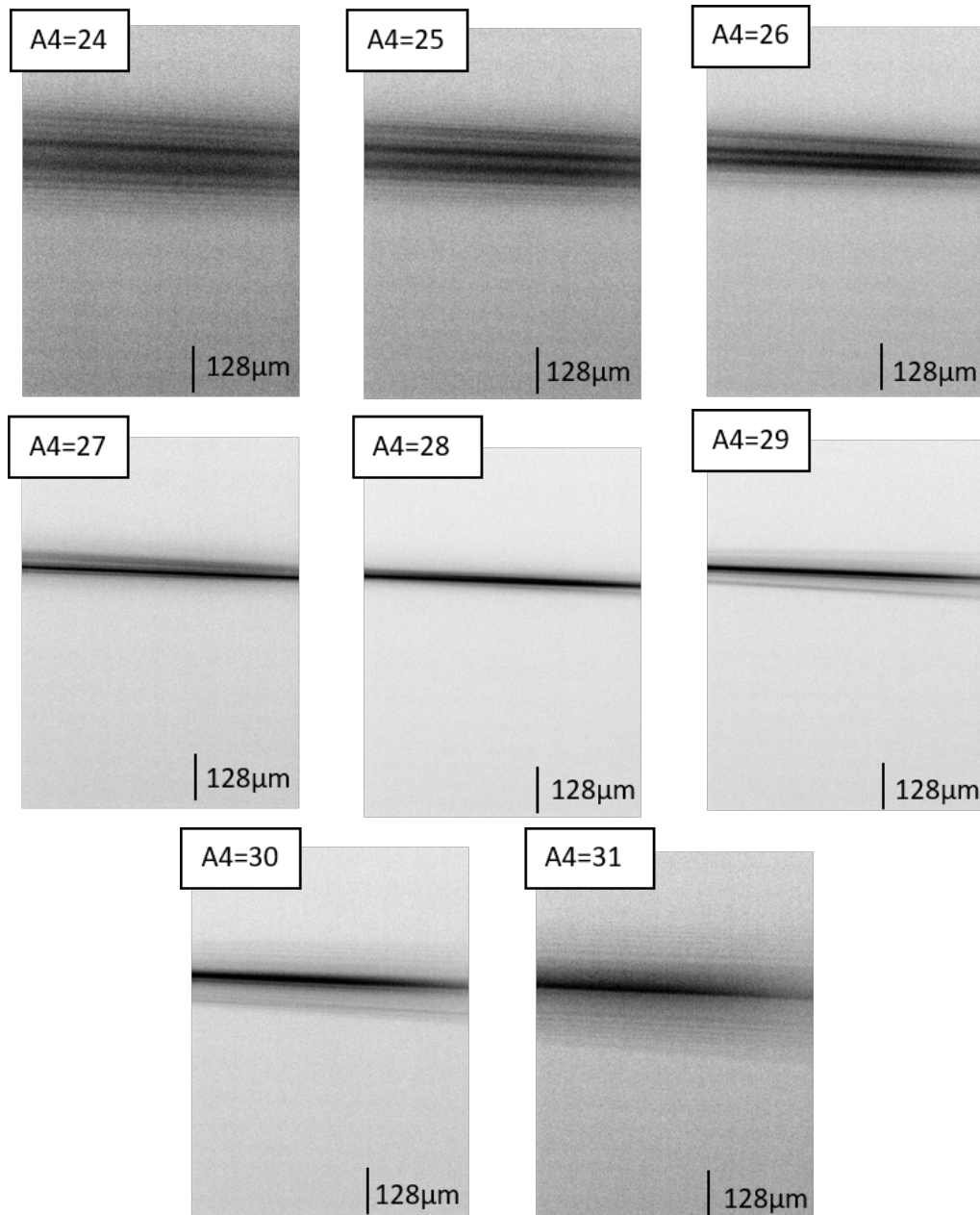


Figure 5.12: Evolution of the LED beam at different defocus values.

The LED source on the system reacts very differently from the HeNe laser. For the LED, the beam is focusing on the vertical plane but not the horizontal plane as can be seen from the

horizontal line on each images of figure 5.12. This result is due to the variation of optical path length differences between neighbouring mirrors of the DMD between the vertical plane and the horizontal plane. As explained in part 5.1.2, the vertical plane has a smaller path length difference (around $6\mu m$) than the coherence length of the LED ($38\mu m$), thus it allows interference and the ability to focus on the vertical plane. However, the horizontal plane has a higher path difference and only 6 mirrors can create interference before the path length becomes too important against the LED, so it will prevent the LED light from focusing on this plane. These results are highly significant: it confirms that the DMD based detection system is able to differentiate low coherence light from laser light.

5.5 Conclusion

In this chapter, four visible laser wavelengths were characterized with the DMD based detection system. Circular and rectangular polynomial patterns were compared and it was shown that they both give wavelength resolutions down to 2.8×10^{-3} , better than most of the laser detection systems based on diffraction grating. Although other types of detection systems do have a better resolution (10^{-9} for both Fabry-perot and Michelson type of detectors for example), they are not the best adapted for our applications. Indeed and as discussed in part 2.4 of chapter 2, Fabry-Perots are restricted in the wavelength range while Michelson interferometer have moving parts which can affect the practicality of this system in an unsteady environment.

Moreover, it was demonstrated in this chapter that the rectangular polynomials loses in sensitivity due to additional optical aberration in the DMD window but its wavelength resolution is similar to the circular polynomials. So one can decide to use the rectangular polynomials over the circular polynomials if the application suits it better.

The four lasers were also analysed in terms of their beam shape as a function of the focal length, it was found that the low coherent lasers (green and blue) behaved in an elliptical fashion, implying that the DMD system distinguish lower coherent sources from higher coherent sources. To confirm this result, a LED source with a $38\mu m$ coherence length was studied against a HeNe laser and the LED behaviour in the system shows again that low coherence sources can be discriminated over higher coherent sources. Thus, I have demonstrated the ability of the DMD system to differentiate laser light against background noise.

This chapter however studied each laser on its own, and no other light sources were used simultaneously. Hence, the next chapter is focus on the use of this detection system with two laser sources at the same time. The high resolution associated with the rectangular polynomial pattern makes it an easy choice to use for this application, as the DMD window will be split in four parts in the next chapter.

Chapter 6

Dynamic use of the DMD window

In chapter 5, it was concluded that the rectangular polynomial pattern allows a good wavelength resolution for laser detection. In this new chapter, I use this advantage to build a new DMD pattern composed of four independent Fresnel zone plates, each located on one fourth of the DMD rectangular window. The idea is to use each of the 4 FZPs with a different defocus value to identify the wavelength quickly. For each FZP, the algorithm developed in chapter 4 is used independently to correct the beam and to allow each of the four focuses on the camera. In this chapter, I am interested in the possibility of using multiple lasers sources at once and two visible lasers were used for that purpose. The first part of this chapter will look at the different technology using several FZPs. In the second part, I introduce the experimental setup, similar to the previous chapter, and in the last part, I present and discuss the results for each laser at a time then for two lasers turned on simultaneously.

6.1 Existing multi-focal Fresnel zone plates

Since I have in mind to use multiple FZPs in a dynamic manner in this chapter, it is interesting to look at other ways the FZP has been used in the past as a multi-focal device and whether some of the use could be of interest for our DMD system.

Two different approaches are used to realize multi-focal FZP. The more conventional way divides the area of the FZP into several sections [127, 128], the division can be done in the azimuthal or the radial direction. Each section is then producing a different focal point. But problems are created by these methods. An azimuthal approach of division implies polarization issues. While a radial division implies a decrease in the foci efficiency as less surface is

used so less light is transmitted.

The second approach to create a multi-focal FZP uses a pixelated phase pattern which normally requires a complicated fabrication process if the FZP were not digital [129]. However, Mohagheghian and Sabouri recently created such pattern with the use of a DMD device [130] and obtained promising results.

There is however no paper that splits the pattern in different identical sections for which each focus could be dynamically changed. This is an interesting aspect to study, as the implementation is simple on the DMD and our correctional algorithm could still be used on this system. For this chapter, the pattern is split in four parts for a first approach of study.

6.2 Implementation of the four Fresnel zone plate on the DMD based laser detection system

In this experiment, four FZPs are written on the DMD to dynamically find out the wavelengths of multiple lasers at once. Two lasers are used, the HeNe laser (HNLS008L-EC) at 632.8 nm and the green laser diode (CPS532) at 532 nm, both mentioned in the previous chapter.

The experimental setup used here is mostly the same as the setup used in chapter 5. The first difference is the pattern written on the DMD. Here, I divide the DMD surface into four FZP patterns to detect four focal spots on the camera. Each FZP surface is identical, their size is 512x384 pixels. As such, the second difference is the distance between the camera and the DMD as the system is diffraction grating based and diffracts the light at different angles depending on their wavelength. To enable the camera to observe two different laser wavelengths, the new camera-DMD distance is set to 9.5 ± 0.2 cm.

To clearly analyse the results for each FZP, the FZPs are numbered from 1 to 4 and their position relative to the DMD surface is illustrated in figure 6.1.

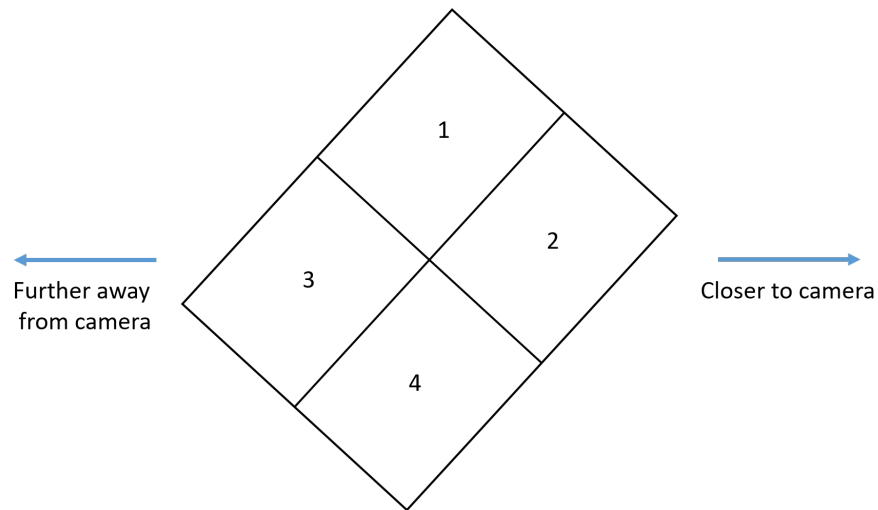


Figure 6.1: Number positions of the four FZP on the DMD window.

Additionally, to gather the four beams on the camera, the center of each FZP is shifted towards the center of the DMD as can be seen in figure 6.2 where an example of four FZPs written on the DMD with the same defocus value for each FZP is illustrated. The center of each FZP is at a distance of 0.8 mm from the center of the DMD.

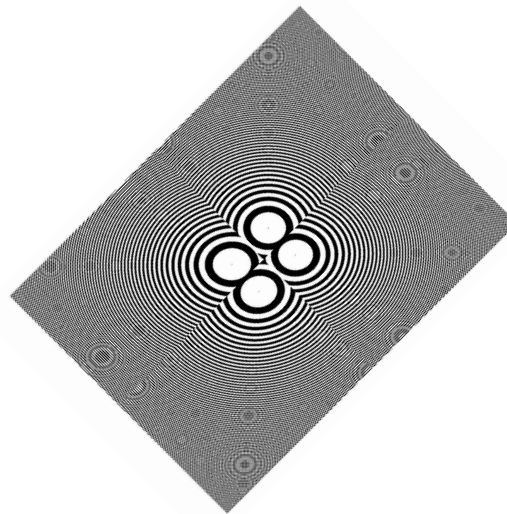


Figure 6.2: Example of a four FZP pattern written on the DMD window.

Finally, to avoid each FZP affecting the beam intensity from the other FZPs, this experiment is done so that each focus for each FZP is found when the 3 other FZPs are either off or already at focus. If this is not done, then the other beam intensities would be important enough to alter the steps of the correctional algorithm.

6.3 Experimental results

6.3.1 Red laser and green laser individually corrected and focused

In this first part, I look at the variation of the beam waist as a function of the Zernike defocus value for the HeNe and the green lasers separately. This implies that only one laser is turned on at a time.

Figure 6.3 and figure 6.4 each gather the results respectively for the HeNe laser and the green laser with a graph depicting the beam size evolution for each FZP as well as the camera image of the four focused and corrected beams. The spots are located in one area of the camera and are not centered on the camera to allow both lasers to appear on the camera as in the next session, I will be studying both lasers turned on simultaneously. The beam size variation around the focal point is plotted for the four FZPs. Each FZP number is linked to the position of the FZP in the DMD window as defined in figure 6.1. For example, FZP 1 in the legend graph corresponds to the diffracted beam of the FZP at the emplacement number 1 in figure 6.1. Additionally, the evolution of the beam size when only one FZP was used on the whole DMD window at a DMD-camera distance of 46 cm - taken from chapter 5 - is added for comparison. Finally, the miniature camera images of each beam are taken so that all the beams have the same peak intensity, however each beam at their focus had different peak intensity on the whole camera image of figure 6.3 and figure 6.4, this is mostly due to the beam not being perfectly centered on the DMD window. The first item that can be analyzed from these graphs is the shape of the beam size evolution for each FZP. In term of the red laser, the shape is relatively similar among each FZP. This is to be expected as the wavelength being the same and the size of each rectangular FZP being identical, only a major change in the focal length would impact this beam evolution. But if the distances between each FZP centers is considered, it is at max of 0.6 mm which is very negligible in term of focal length variation and thus in term of beam size variation. On the other hand, the green laser has one noticeable difference between the four shapes. FZP 1 has its evolution around the focal point slower than for the three other FZPs. However, as it was stated in the previous chapter, the bandwidth of the green laser is significant enough to impact the beam evolution. Although the experience was done on the same day, the recording of the data was not automated, and that implies a delay of few minutes between each data set recorded, which would then impact

the laser wavelength and thus the beam evolution around the focal point.

The second item that can be looked at is the results between the single FZP when written on the whole DMD surface at the DMD-camera distance of 46 cm and the four FZPs when written on smaller surfaces of the DMD at the DMD-camera distance of 9.5 cm. For both red and green lasers, the four FZPs beam evolution is slower than for the evolution from the bigger FZP. Dividing the surface in four implies that the intensity at each focus will be one fourth of the intensity of the big FZP focus if there were at the same distance. However, the initial focal length was also divided by almost 5 (from 46 cm to 9.5 cm) so it increases the amount of light reaching each of the four focuses by 1.5 compared to the initial distant single focus. This value is found out when the beam waist formula $w_0 = \frac{\lambda f}{\pi r}$ is combined with the intensity at the center of the beam waist for a Gaussian beam $I_0 = \frac{2P_0}{\pi w_0^2}$ where P_0 is the initial power of the beam. So more intensity reaches each of the four focuses than the single FZP focus. Implying that the intensity change and thus the beam size will be slower around the focal point for the 4 FZP focuses than for the focus from the 1 single FZP, just as observed in the graph. In other words, using a bigger DMD array gives better wavelength resolution as would be expected.

Moreover, two pieces of information can again be taken out from these two graphs after a second order polynomials is fitted to each data set: the beam waist for each FZP and their corresponding defocus values. The new data are gathered in table 6.1.

Table 6.1: Comparison of experimental and theoretical values of Zernike defocus and beam waist with wavelengths at 532 nm and 632.8 nm for each FZP at a focal length of 9.5 cm.

HeNe laser					
	FZP 1	FZP 2	FZP 3	FZP 4	Big FZP
Zernike defocus value	26.34±0.25	27.62±0.28	26.13±0.21	27.69±0.23	26.65±0.13
Experimental beam waist $\omega_{0,exp}$ (in μm)	18.9±0.3	23.1±0.4	21.8±0.3	23.4±0.3	34.2±0.3
Diffraction limited beam waist $\omega_{0,theory}$ ($\pm 0.1\mu m$)			4.4		10.6
$\omega_{0,exp}/\omega_{0,theory}$	4.3	5.3	5.0	5.3	3.2

Green laser					
	FZP 1	FZP 2	FZP 3	FZP 4	Big FZP
Zernike defocus value	30.65±0.32	32.34±0.19	31.02±0.19	31.86±0.20	31.05±0.16
Experimental beam waist $\omega_{0,exp}$ (in μm)	29.2±0.4	23.1±0.3	28.1±0.4	21.3±0.6	51.1±1.2
Diffraction limited beam waist $\omega_{0,theory}$ ($\pm 0.1\mu m$)			3.7		8.9
$\omega_{0,exp}/\omega_{0,theory}$	7.9	6.2	7.6	5.8	5.7

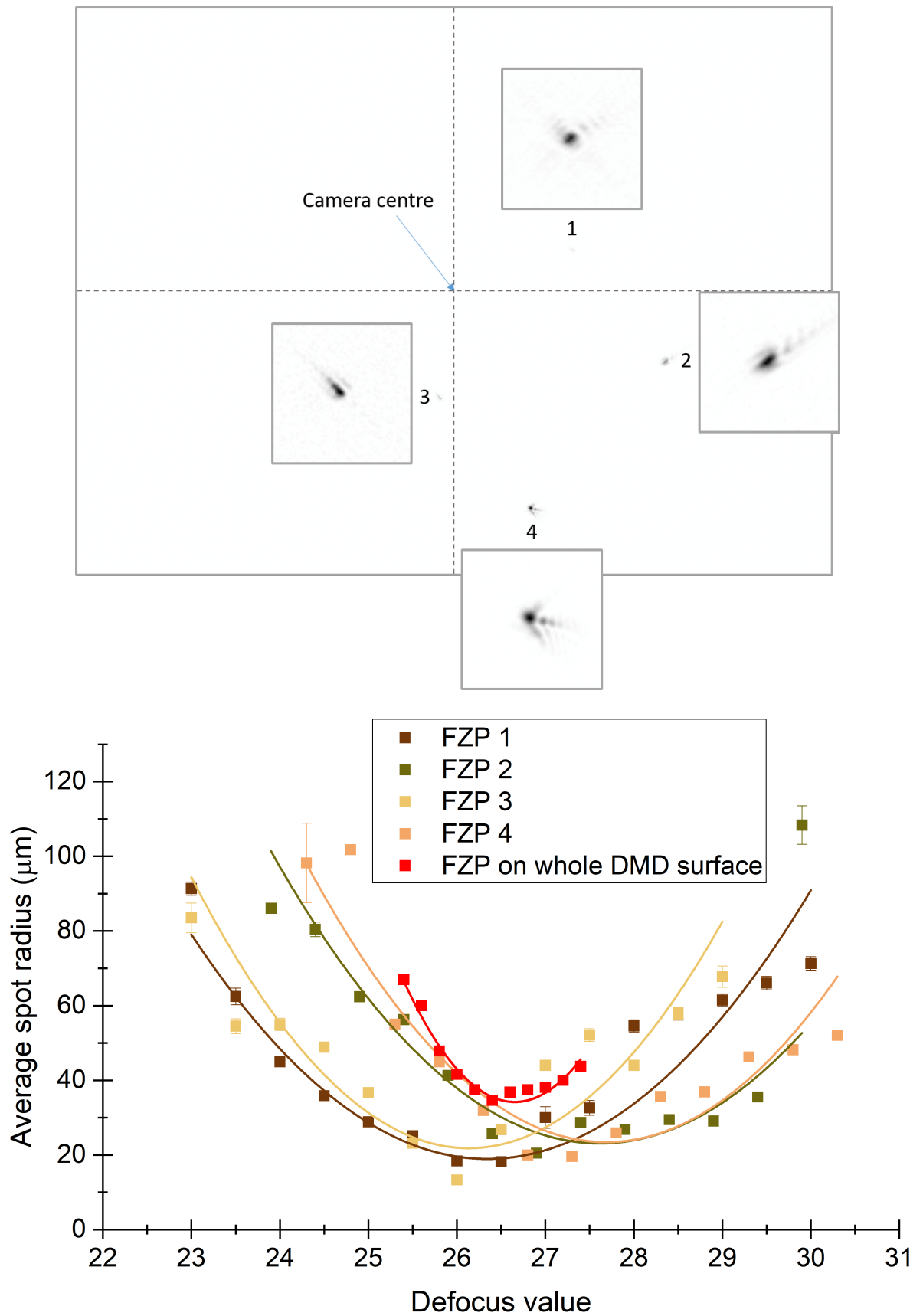


Figure 6.3: (top) Four HeNe laser beams focusing on camera after correction. (bottom) Evolution of the HeNe laser beam size for each of the four FZPs with a distance DMD-camera of 9.5 cm (FZP 1, 2, 3 and 4) and evolution of the HeNe laser beam size for one single FZP on DMD with a distance DMD-camera of 46 cm (FZP on whole DMD surface).

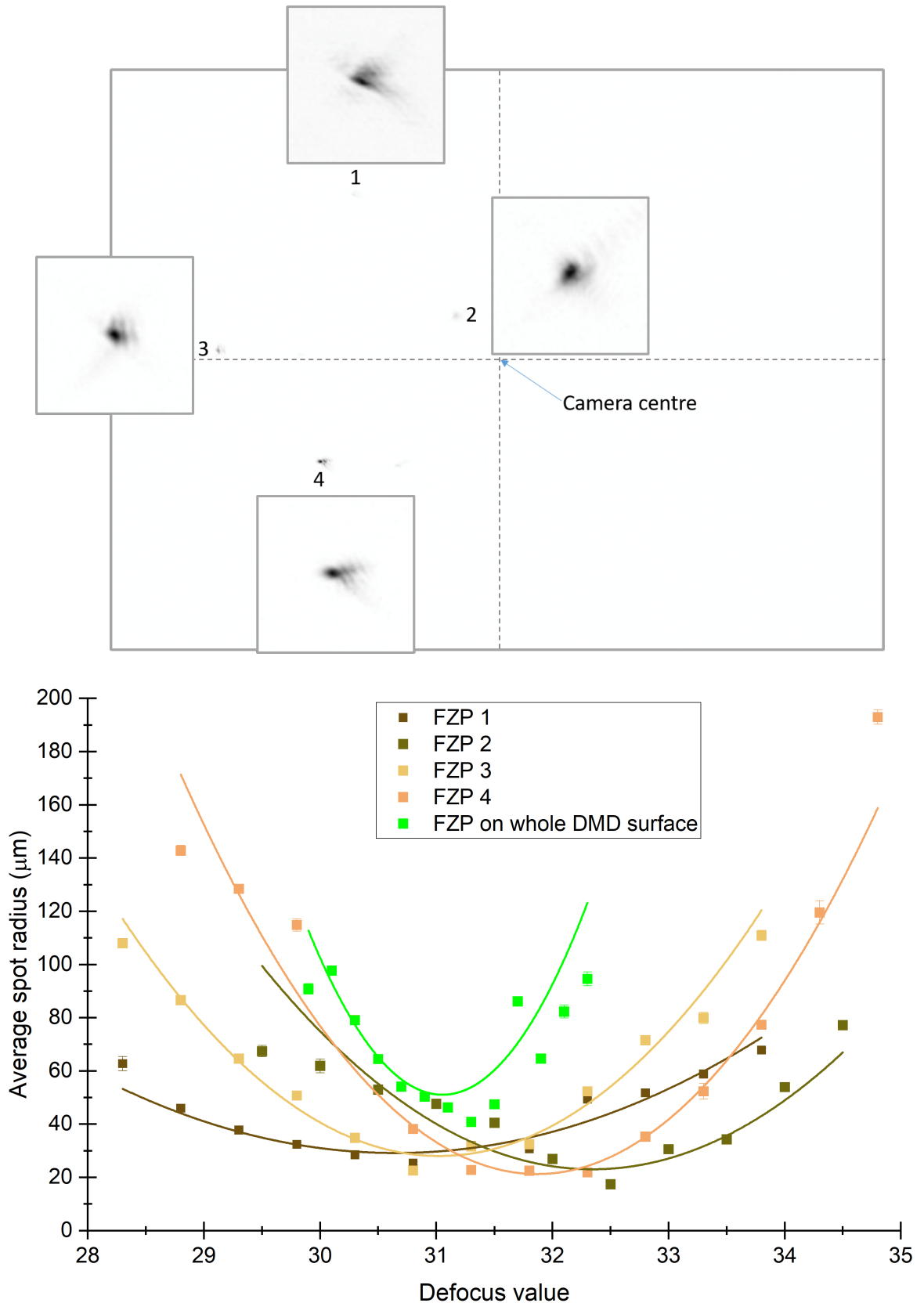


Figure 6.4: (top) Four green laser beams focusing on camera after correction. (bottom) Evolution of the green laser beam size for each of the four FZPs with a distance DMD-camera of 9.5 cm (FZP 1, 2, 3 and 4) and evolution of the green laser beam size for one single FZP on DMD with a distance DMD-camera of 46 cm (FZP on whole DMD surface).

If the results between the red and the green lasers for each FZP are first compared, it can clearly be seen a distinction between the defocus values. The HeNe laser has a defocus value ranging from 26.13 ± 0.21 to 27.69 ± 0.23 while the green laser has a defocus value ranging from 30.65 ± 0.32 to 31.86 ± 0.20 . This corresponds to a maximum difference of defocus between the four FZP of 1.5 for the red laser, and of 1.2 for the green laser. This discernible difference implies that the focal length from the center of each FZP to their corresponding spots on the camera is different enough to be detected by our system.

Now, among the HeNe results, it can be seen that two groups are formed between the FZPs based on their defocus value: the FZPs 1 and 3 and the FZPs 2 and 4. FZPs 1 and 3 have a lower defocus values than the FZPs 2 and 4, which should translate with FZPs 1 and 3 having a bigger focal length than FZPs 2 and 4. To explain this observation, let's use figure 6.3 which shows the position of each four spots in comparison to the middle of the camera, where the DMD center is normally aligned to. It can be seen that FZPs 1 and 3 are the closest to the center of the camera while FZPs 2 and 4 are further away. This implies that FZP couple 1 and 3 and FZP couple 2 and 4 are indeed closer in focal length which would then explain the difference in defocus values. This difference however is still too important compared to the focal length changes among the FZPs, of few micrometres. But an important inaccuracy measurement at the defocus value is also noticeable, an average among the four FZPs of 0.24, it is double the amount of the single FZP defocus value. These inaccuracies are caused by the optical aberrations present on each four of the beams and more difficult to correct than when one single FZP was used on the whole DMD surface.

For the green laser data, it becomes more difficult to analyse the observation, as was stated earlier the FZP number 1 is not acting as expected with its beam size evolution being slower than the three other FZPs. The reason being that the focal length varies importantly for the green laser due to its bandwidth.

For both lasers however, the measured beam waists for each FZP can be looked at and they can be compared to the beam waist when one single FZP was used on the whole DMD. For the HeNe laser, the experimental beam waist between the four FZPs is from $18.9 \mu\text{m}$ to $23.4 \mu\text{m}$ while it was at $34.2 \mu\text{m}$ when the whole DMD window was used in the previous chapter. For the green laser, the experimental beam waist between the four FZPs is from $21.3 \mu\text{m}$ to $29.2 \mu\text{m}$ while it was at $51.1 \mu\text{m}$ for the single FZP on the DMD. In this experiment, both the focal length and the window of the reflected beams were shorten compared to the previous

chapter. The ratio value of the focal length and the surface radius between the 4 FZPs pattern and the single FZP pattern is: $(f/r)_{1FZP} = 2.4 * (f/r)_{4FZP}$. This experimental ratio is at 1.6 for the HeNe laser and 2 for the green laser when the value for the 4 FZP is averaged. Any difference between the two ratios for each laser can be explained from the correctional algorithms, although the results with this algorithm were conclusive in the previous chapter, they are not flawless. All the aberration correction outside of the astigmatism is based on the peak intensity and its best value, but this doesn't always imply the best correction. This should be taken into account for any future work on this detection system.

6.3.2 Overlap use of red and green laser

In this second part, I look at the DMD based laser detection system when two lasers are superposed and directed into the optical fibre and shone over the DMD surface. The Zernike defocus value related to a specific FZP number and that corresponds to the focus of one laser on camera is used from table 6.1. The four FZP pattern is implemented so that FZPs number 1 and 2 are focusing the green laser while FZPs 3 and 4 are focusing the red laser. Figure 6.5 shows a camera image of the green and red laser beams corrected and focused on the camera. Four focused beams are shown as well as the FZP numbers used to focus each of those beams.

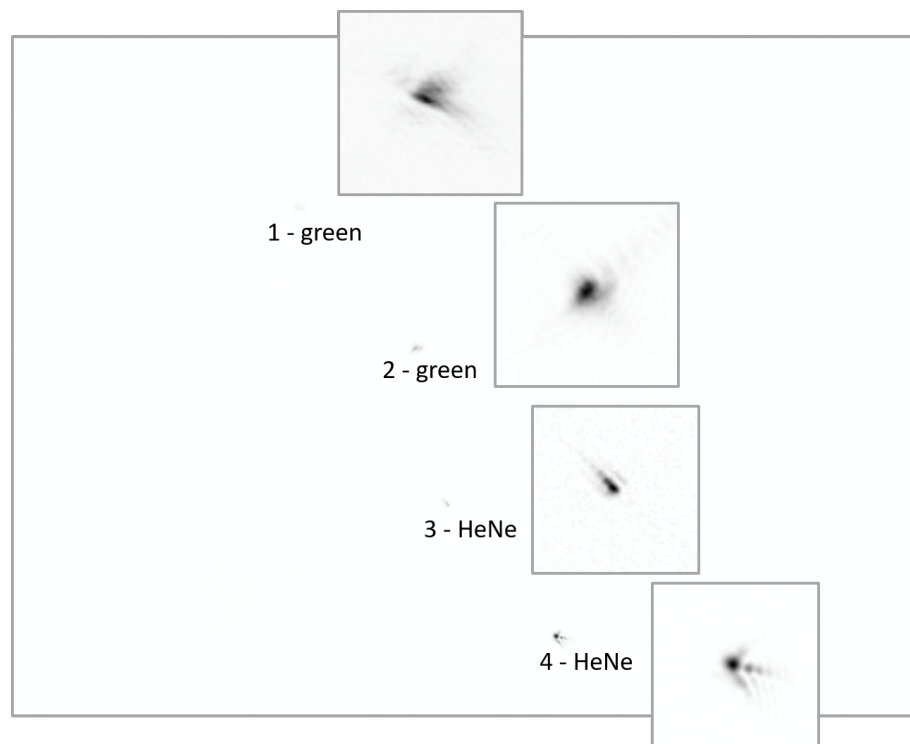


Figure 6.5: Two green focused laser beams and two red focused laser beams diffracted from the four FZPs pattern and the corresponding FZP number for which each beam is focusing from.

In this instance, the position of each FZP can clearly be identified depending on the laser used when we compare with the camera images of figures 6.3 and 6.4. This implies that the two lasers shone on the DMD based laser detection can be distinguished and moreover their wavelength can be found out as it was first characterized previously. If the wavelength is unknown and not previously characterised, an estimation of the wavelength could be done by using the 4 FZPs dynamically with 4 different defocus values. Repeating this with several defocus values would then allow us to plot a graph similar to figure 4.22 so that the defocus value corresponding to the beam at focus can be found out. From this, using the wavelength characterisation figure 5.9, the wavelength can be estimated. If two or more wavelengths are used on the system, this should be detectable; if only one wavelength was used, the distances between beams 1 and 4 and beams 2 and 3 would be the same. If these distances are not the same, this implies several wavelengths are used. In this case, only 1 FZP pattern at once can be used to characterise each wavelength instead of the 4 FZPs, which would delay the characterisation but not make it impossible.

All four spots are detectable, and the distance between beams spots 1 and 2 (or 3 and 4) is defined from the distance of the FZPs centers on the DMD pattern, defined as 1.3 mm on the DMD width. The DMD acting as a 2D diffraction grating brings the two lasers at two different area on the camera. The distance between the two laser area centers is measured at 1.7 mm on camera while in theory I calculated a length of 1.4 mm if mode number 2 is considered for the red and green lasers. This is the interesting aspect of the DMD device combined with FZPs, the diffraction pattern will be a convolution of the DMD micromirrors with the focii of the 4 FZPs. This will lead to four focused beams repeated at a distance $D = \frac{f \times \lambda}{w}$ on the vertical and horizontal axis for each wavelength λ at a focal length f and a mirror width w . With the width of the camera equal to 4.76 mm, if the current setup is considered for the DMD, the extreme wavelengths seen by the camera would be 685 nm.

6.4 Conclusion

In this chapter, the red and the green lasers were characterised with a four FZP pattern on the DMD. The defocus value corresponding to the focus on camera was found for each of the four FZPs and for each laser separately. Moreover, it was confirmed that the DMD based laser detection system is able to detect the two lasers together. The distance camera-DMD

was chosen so that both lasers appear on camera, two additional wavelengths could be added and still be detected at this distance as long as their corresponding FZP located on the DMD is chosen coincidentally with the focused beam location on camera. Indeed, the four focused beams are 1 mm away from each other, so this needs to be taken into account to have all beams at different wavelengths on camera. Finally, the four beams were detectable for each laser, so although the sensitivity worsen when dividing the DMD surface in four parts, this didn't affect the detection. This implies that it could be possible to increase the amount of FZPs on the DMD to increase the amount of wavelength detectable by the system.

Chapter 7

Discussion and future work

7.1 Review of the research challenges and objectives

This thesis presents the design and development around laser detection systems for various industrial applications. However, this work is mainly focused in applications for defense. The first objective of this thesis was to implement a wider field of view of a modified Mach-Zehnder interferometer. I implemented a cone mirror to extend the horizontal field of view of the system from $\pm 3^\circ$ to 360° with a possibility to determine the laser direction with an angular inaccuracy of $\pm 5^\circ$.

The second objective was to develop a laser detection system with requirements defined in the introduction of this thesis. The system in question uses a FZP pattern written on a DMD. The experimental development of this system happened in three phases. In the first phase, I developed an algorithm on LabView to correct astigmatism aberrations due to the system output angle of deviation and additional aberrations present in the DMD system. With this correctional algorithm, I reduced the beam size at the focus to 1/10th of the initial beam size. In the second development step, I characterized several laser wavelengths and found the relative wavelength resolution of the system at 10^{-3} , better than most of the low-cost laser detection systems using diffraction gratings. In the third development phase, I studied the impact of different coherence lengths in the system, including a LED source. What I found confirms the theory, the DMD-FZP system has a coherence difference between its vertical and horizontal axis. This difference in coherence implies that low coherent sources are distinguishable from higher coherent sources, thus our system achieves laser discrimination against background light. The DMD kit was the expensive part of the system, around £1500,

but overall the system is relatively low-cost with the only additional need for a CCD camera. However, one aspect of the requirements is not achieved in this system and it is the wide field of view. This is something important to study next as extending the field of view often implies decreasing the sensitivity of a system. But this task could be given to engineers, as it would only require practical development of the system and not altering its principle. With this setup, the response time is relatively low once the wavelengths are characterized. Only few defocus values could be used to find the corresponding laser wavelength. However, I also investigated the possibility to shorten the time detection of lasers by dividing the DMD pattern in four independent FZPs. This would allow to find the wavelength in a single DMD pattern instead of going through several consecutive frames. This type of detection makes it almost instantaneous.

7.2 Future work

Several criteria could be added to expand the practicality of the DMD based detection system: a wider field of view, a wider wavelength detection range, pulsed laser detection and the resolution improvement through a better correctional algorithm.

7.2.1 Field of view development

The DMD window is a flat surface that directs normal input light towards two directions: $+24^\circ$ and -24° . As such, the input direction is restricted to the normal of the DMD if the camera is fixed in the system. It could be thought of using the cone mirror used in chapter 3 to extend the horizontal field of view, however the output light of the cone mirror is widely distributed in an arc shape and this might be problematic. If only a part of the FZP pattern is illuminated, then the focus will be difficult or impossible to obtain depending on the size of the arc. A better way to widen the field of view of the system would be with the use of optical fibres in a similar fashion to what was done in reference [54]. They used two lenses combined with a fibre bundle and reached 45° field of view. This however is relatively expensive to implement as the lenses are specially made and a fibre bundle can cost as much as £500. However, the use of such a system would work really well with the flat surface of the DMD window, and therefore might be a good investment for future works.

7.2.2 Pulsed lasers

For pulsed lasers, two aspects of the system need to be studied before consideration: the thermal resistance of the DMD related to the incident power and the camera frame rates. For high power lasers, the current DMD is not adequate. A specific DMD was developed to take high power and NIR sources into account: the DLP650LNIR. The price of only the chip is at £1,044. It can take up to 160 W in incident light. But the thermal time for which the micromirrors can endure high temperature is low, at around 30 μ s so it implies that "pulsed lasers with low average power but very high peak power can possibly damage the micromirrors since the thermal mass of an individual mirror is low and heating will occur rapidly" [131]. So this DMD should be used for low power pulsed lasers preferably. Another issue that needs to be considered is the camera frame rates. If the 4 FZP pattern is used, then the short pulsed duration will not be as much of a problem in the detection process. The major problem would be with the camera, the repetition rate of the current camera is 24 frames per second. This implies that high repetition rate lasers would require higher integration time thus prolonging the initial detection time. It is also possible to change to a camera with higher frame rates, but with the downside of an increased cost. However, the current camera should work for a low repetition rate of the order of 10 Hz and this could be interesting to study in a future work.

7.2.3 NIR light detection

Currently the wavelength range is favorable for visible light due to the DMD window anti-reflective coating and the visible range camera. The anti-reflective coating reduces reflection and increases transmission efficiency with a typical transmittance of 97% in the visible wavelength range. With the visible anti-reflective coating, the transmittance in the NIR range is down to 70% from 1250 nm and upwards [132]. However, if one wanted to look at pulsed lasers as discussed in the previous part, the DLP650LNIR should be used. Additionally, this DMD chip is meant for NIR lights with a transmittance of 93% between 850 nm and 2000 nm. With this chip, the transmittance in the visible range is down to 80% but can be as high as 90% depending on the wavelength. This amount is still relatively high, and would allow a good amount of visible light to reach the camera. Another problem however comes from the current camera as it is detecting visible light only. To fix this issue, a second camera in the NIR

wavelengths could be added to detect a wider range of wavelengths. Since the DMD system diffracts the input light in two directions and only one direction was used in this research, the second channel could be used for NIR wavelength characterization.

7.2.4 Algorithm development

The current correctional algorithm uses Zernike polynomials to correct optical aberrations. The next important work would be the improvement around the detection of the peak intensity for the Zernike polynomials numbers 7 to 15. As said before, although this gave interesting results, looking at the peak intensity can lead to an inaccurate correction of the aberration. It could be more accurate to use a function that would take the ratio of the average intensity in a predefined disk against the average energy in the rest of the image as done by Popoff in reference [119]. Another way to improve this algorithm is to combine Zernike polynomials with the Gerchberg–Saxon (GS) algorithm for example. The GS algorithm is a phase retrieval algorithm and would be used as a second step correction after the Zernike polynomials correction. Scholes et al. used this system recently and they seemed to have obtained a more accurate correction of the beam [120].

7.2.5 Field trial

One aspect that needs to be investigated in the future is the impact of real life conditions on the system and for this a field trial should be considered. There are two real life conditions that should be considered: the atmosphere impact on the laser beam and the maximum laser-DMD distance for which the laser is still detectable by the system. In the case of the atmosphere impact, several aspects of the beam are affected. The atmosphere disturbances are due to changes in pressure, temperature or composition which implies that the refractive index of the air is not constant. This causes important and random changes of the shape, the quality and the intensity of the beam. As such, the sensitivity level of the DMD system should be investigated. Concerning the maximum detectable distance between the DMD and the laser, one aspect to consider is the divergence of the beam over distances. This depends on the type of laser of course, but this needs to be investigated and determined for several lasers in outdoor conditions.

References

- [1] *Civil Aviation Authority*. World Wide Web page. 2018. URL: <https://www.caa.co.uk/Data-and-analysis/Safety-and-security/Datasets/Laser-incidents/>. (accessed: 31.05.2021).
- [2] *Laser Incidents*. World Wide Web page. 2021. URL: <https://www.faa.gov/about/initiatives/lasers/laws/>. (accessed: 31.05.2021).
- [3] S. M. Tipper and al. “Low-cost camera-based continuous-wave laser detection”. In: *Optical Engineering* 59.5 (2020), pp. 1 –13. DOI: 10.1117/1.0E.59.5.057107.
- [4] J. Pietrzak. “Laser warning receivers”. In: *Proc. of SPIE* 5229 (2003).
- [5] J. Zhang et al. “A Review of Laser Warning Receivers Based on Spectral Discrimination and Coherent Detection”. In: *Journal of test and measurement technology* 56 (2006).
- [6] D.M. Benton. “Low-cost detection of lasers”. In: *Opt. Eng.* 56 (2017).
- [7] M. Zandi, S. Sugden, and D.M. Benton. “Low-cost laser detection system with a 360-deg horizontal field of view”. In: *Optical Engineering* 60.2 (2021), pp. 1 –11. DOI: 10.1117/1.0E.60.2.027106.
- [8] J.C. Russell. “Coherent laser warning system”. Pat. 6,151,114. 2000.
- [9] A.D. Mcaulay. “Detecting modulated lasers in the battlefield and determining their direction”. In: *Proc. of SPIE* 7336 (2009).
- [10] *ComponentLibrary by Alexander Franzen is licensed under a Creative Commons Attribution-NonCommercial 3.0 Unported License*.
- [11] A. E Siegman. *Lasers*. United states of America: University Science Books, 1986. Chap. 1: An introduction to lasers, pp. 1–79.
- [12] Peter W. Milonni and Joseph H. Eberly. *Laser physics*. United states of America and Canada: John Wiley & Sons, 2010. Chap. 1: Introduction to laser operation, pp. 1–15.

- [13] William T. Silfvast. *Laser fundamentals, second edition*. United states of America: Cambridge University Press, 2004. Chap. 6: Radiation and thermal equilibrium, pp. 199–222.
- [14] Jeff Hecht. *Understanding Lasers: An Entry-Level Guide, third edition*. Ed. by Lajos Hanzo et al. United states of America and Canada: John Wiley & Sons, 2012.
- [15] Anil Kumar Maini. *Lasers and optoelectronics : fundamentals, devices, and applications*. United Kingdom: John Wiley & Sons, 2013.
- [16] F. Graham Smith, Terry A. King, and Dan Wilkins. *Optics and Photonics: An introduction*. England: John Wiley & Sons, 2007.
- [17] Coherent inc. *Lasers: Understanding the Basics*. URL: https://www.photonics.com/a25161/Lasers_Understanding_the_Basics.
- [18] Bahaa E. A. Saleh and Malvin Carl Teich. *Fundamental of Photonics, third edition*. United states of America and Canada: John Wiley & Sons, 2019.
- [19] Rüdiger Paschotta. *RP Photonics Encyclopedia - Coherence*. World Wide Web page. URL: <https://www.rp-photonics.com/coherence.html>. (accessed: 31.05.2021).
- [20] Ministry of Defence and Defence Safety Authority. *DSA03.OME part 5: Military Laser Safety*. World Wide Web page. URL: <https://www.gov.uk/government/publications/dsa03ome-part-5-military-laser-safety>. (accessed: 10.11.2021).
- [21] *The effects of laser illumination of aircraft*. World Wide Web page. URL: <https://ifalpa.org/media/2053/12medb101-the-effects-of-laser-illumination-of-aircraft.pdf>. (accessed: 09.11.2021).
- [22] *Types of Lasers*. World Wide Web page. URL: <https://www.newport.com/n/laser-types>. (accessed: 08.11.2021).
- [23] Washington State University – Health Sciences Campuses. *Laser Safety Program*. World Wide Web page. URL: <https://spokane.wsu.edu/research/documents/2020/07/laser-safety-program.pdf/>. (accessed: 10.11.2021).
- [24] Oregon State University. *Laser Biological Hazards-Eyes*. World Wide Web page. URL: <https://ehs.oregonstate.edu/laser/training/laser-biological-hazards-eyes>. (accessed: 10.11.2021).
- [25] J. Lein. “Spectral linewidth and coherence”. PhD thesis. University of Oslo, 2010.

- [26] Eugene Hecht. *Optics, fifth edition*. United Kingdom: Pearson Education Limited, 2017.
- [27] J Dubois and F Reid. "Detecting laser sources on the battlefield". In: *Photonics North 2007, SPIE 6796* (2007).
- [28] E Linton and al. "Retinal burns from laser pointers: a risk in children with behavioural problems". In: *Eye* 33 (2019), 492–504.
- [29] *Never aim laser pointers at aircraft*. World Wide Web page. 2017. URL: http://www.laserpointersafety.com/laser-hazards_aircraft/laser-hazards_aircraft.html. (accessed: 31.05.2021).
- [30] Marek Zygmunt and Krzysztof Kopczynski. "Laser warning system as an element of optoelectronic battlefield surveillance". In: *Radioelectronic Systems Conference 2019*. Ed. by Piotr Kaniewski and Jan Matuszewski. Vol. 11442. International Society for Optics and Photonics. SPIE, 2020, pp. 1–7. DOI: 10.1117/12.2565139.
- [31] Inc. B.E. Meyers & Co. *GLARE LA-9/P*. World Wide Web page. URL: <https://bemeyers.com/glare-la-9-p>. (accessed: 10.11.2021).
- [32] Katerina Margariti and Thomas Kamalakis. "Coherent Optical Wireless: An Alternative Technology for Broadband Indoor Communications". In: *International Conference on Transparent Optical Networks* (2017).
- [33] David J T Heatley et al. "A review of Optical Wireless". In: *British Telecom Engineering* 17 (1999).
- [34] K. Kikuchi. "Coherent Optical Communications: Historical Perspectives and Future Directions". In: *High Spectral Density Optical Communication Technologies*. Ed. by M. Nakazawa et al. Berlin: Springer, 2010.
- [35] H. Kaushal and G. Kaddoum. "Optical Communication in Space: Challenges and Mitigation Techniques". In: *IEEE Communications Surveys and Tutorials* 19 (2017).
- [36] Morio Toyoshima. "Recent Trends in Space Laser Communications for Small Satellites and Constellations". In: *J. Lightwave Technol.* 39.3 (Feb. 2021), pp. 693–699.
- [37] David N. Amanor, William W. Edmonson, and Fatemeh Afghah. "Inter-Satellite Communication System based on Visible Light". In: *IEEE Transactions on Aerospace and Electronic Systems* (2018).

- [38] F.J.Duarte. "Secure interferometric communications in free space". In: *Optics Communications* 205 (2002).
- [39] F. J. Duarte et al. "N-slit interferometer for secure free-space optical communications: 527 m intra interferometric path length". In: *J. Opt.* 13 035710 (2011).
- [40] S. Mohammad Nejad, H. Arab, and N. Ronagh Sheshkelani. "Analysis of new laser warning technologies to propose a new optical subsystem". In: *Iranian Journal of Electrical and Electronic Engineering* 14 (2018).
- [41] L. Wang et al. "Optimum design of wide angle laser detecting system based on fish eye lens and sinusoidal amplitude grating". In: *Optics Communications* (2014).
- [42] D.M Benton, M. Zandi, and K. Sugden. "Laser detection utilizing coherence". In: *Technologies for Optical Countermeasures XVI*. Ed. by David H. Titterton, Robert J. Grasso, and Mark A. Richardson. Vol. 11161. International Society for Optics and Photonics. SPIE, 2019, pp. 139 –144. DOI: 10.1117/12.2532058.
- [43] D. A. Solomakha and A. K. Toropov. "Laser wavelength measurements". In: *Sov. J. Quantum Electron* 7.929 (1977).
- [44] R. Crane Jr. "Laser Detection by Coherence Discrimination". In: *Optical engineering* 18 (1979).
- [45] R. Crane Jr. "The angle-scanned interferometer". In: *Optical engineering* 18.2 (1979).
- [46] E.T. Siebert. "Analyzer for coherent radiation". Pat. 4,309,108. 1982.
- [47] W.T. Krohn, M.J. McNally, and R. Abreu. "Coherent radiation detectin apparatus". Pat. 4,600,307. 1986.
- [48] V.A. Manasson, L.S. Sadovnik, and J.H. Parker Jr. "Laser Warning Receiver Based on Coherence Discrimination". In: *IEEE* (1996).
- [49] T. J. Scholl et al. "Broadband precision wavelengthmeter based on a stepping Fabry–Pérot interferometer". In: *Review of Scientific Instruments* 75 (2004).
- [50] D. Hickman. "An optical sensor based on temporal coherence properties". In: *J. Phys.* 21 (1988).
- [51] C. J. Duffy and D. Hickman. "An imaging system based on temporal coherence differences". In: *J. Phys.* 21 (1988).

- [52] P. Sutton. "A novel electro-optical remote-sensing technique based on bandpass coherence processing". In: *J. Phys.* 22 (1989).
- [53] R.C. Coutinho et al. "Detection of Coherent Light in an Incoherent Background". In: *IEEE* (1999).
- [54] L. Xiao et al. "A New Design for Laser Warning System". In: *Proc. of the 7th WSEAS International Conference on Signal, Speech and Image Processing* (2007).
- [55] M. Wakim et al. "Highly accurate laser wavelength meter based on Doppler effect". In: *Optics Communications* 262 (2006).
- [56] E. Loewen. *Diffraction grating handbook*. New York, USA: Newport Corporation, 2005.
- [57] J. L. Zhang, E. M. Tian, and Z. B. Wang. "Research on coherent laser warning receiver based sinusoidal transmission grating diffraction". In: *Journal of Physics: Conference Series* 48 (2006).
- [58] L. Fu and Z. G. Hong. "Design of laser warning receiver based on DSP". In: *IEEE* (2009).
- [59] D. Dudley, W. Duncan, and J. Slaughter. "Emerging Digital Micromirror Device (DMD) Applications". In: *Proc. of SPIE* 4985 (2003).
- [60] M. Mohagheghian and S. G. Sabouri. "Laser Wavelength Measurement Based on a Digital Micromirror Device". In: *IEEE photonics technology letters* 30 (2018).
- [61] H. Partanen, J. Turunen, and J. Tervo. "Coherence measurement with digital micromirror device". In: *Optics letters* 39 (2014).
- [62] D.M. Benton. "Multiple beam steering using dynamic zone plates on a micromirror array". In: *Opt. Eng.* 57 (2018).
- [63] J. Dubois. "Very high angular resolution laser beam rider detector having a gated image intensifier and a video camera". Pat. US 5,280,167. 1994.
- [64] C.E. Nourcier. "Low-cost laser range finder system architecture". Pat. US 5,638,163. 1997.
- [65] G. Bolander and K. Nissborg. "Laser warning device providing a direction of laser radiation". Pat. US 5,440,116. 1995.
- [66] S. Kumar et al. "Design of a laser-warning system using an array of discrete photodiodes—part I". In: *Journal of battlefield technology* 14.1 (2011).

- [67] M. Jurba et al. "Extended spectral range laser receiver". In: *Optoelectronics and advances materials - rapid communications* 6 (2012).
- [68] A. F. El-Sherif et al. "The design and implementation of photoacoustic based laser warning receiver for harsh environments". In: *Opt. Laser Technol.* (2017).
- [69] A. Beche, B. Forestier, and L. Perruchotma. "Panoramic device for detection of laser pulses". Pat. US 9,784,823. 2017.
- [70] B. Chen and W. Zhang. "Study on warning radius of diffuse reflection laser warning based on fish-eye lens". In: *Proc. of SPIE* 8907 (2013).
- [71] J. Ying and Z. Zhou. "Study on Image Processing Technology in Imaging Laser Detection System". In: *IEEE* (2010).
- [72] J. Ying, Y. He, and Z. Zhou. "Analysis on Laser Spot Locating Precision affected by CMOS Sensor Fill Factor in Laser Warning System". In: *IEEE* (2009).
- [73] M. Dabrowski et al. "Laser Warning Receiver LWR-H". In: *Proc. of SPIE* 6598 (2007).
- [74] D. Li and G. Xiong. "The design for the laser detection and warning optical system". In: *Proc. of SPIE* 7382.10 (2009).
- [75] N. Roy and F. Reid. "Off-axis laser detection model in coastal areas". In: *Optical Engineering* 47.8 (2008).
- [76] E. P. Shettle and R. Fenn. *Models for the Aerosols of the lower atmosphere and the effects of humidity variations on their optical properties*. Tech. rep. Air force systems command, USAF, 1979.
- [77] Aquila et al. "MADE-in: a new aerosol microphysics submodel for global simulation of insoluble particles and their mixing state". In: *Geoscientific Model Development* 4 (2011).
- [78] Aquila et al. "Made-in: a new aerosol microphysics submodel for global simulation of potential atmospheric ice nuclei". In: *Geoscientific Model Development* 3.4 (2010).
- [79] Sausen R. et al. *High Performance Computing in Science and Engineering*. Berlin, Heidelberg: Springer, 2010. Chap. Wagner S., Steinmetz M., Bode A., Müller M. (eds) Global Chemistry-Climate Modelling with EMAC.
- [80] B. Björkman. "Laser warning method and apparatus". Pat. US 5,040,891. 1990.
- [81] B. Björkman. "Laser warning system". Pat. GB 2,187,355. 1987.

- [82] D. Goular et al. "Off-axis laser warning sensor". In: *Proc. of SPIE 7323.732314-1* (2009).
- [83] M. Zandi, D.M. Benton, and K. Sugden. "Developments in low-cost laser detection: wide field of view implementation and direction determination". In: *Technologies for Optical Countermeasures XVI*. Vol. 11161. SPIE, 2019, pp. 145–151. DOI: 10.1117/12.2532560.
- [84] S. Affan Ahmed, M. Mohsin, and S.M. Zubair Ali. "Survey and technological analysis of laser and its defense applications". In: *Defence Technology* (2020).
- [85] V.C. Coffey. "High-Energy Lasers: New Advances in Defense Applications". In: *Optics & Photonics News* (2014), pp. 30–35.
- [86] A.K. Maini. "Military Applications: Laser Instrumentation". In: *Lasers and Optoelectronics*. John Wiley & Sons, Ltd, 2013. Chap. 14, pp. 508–565.
- [87] P. Murphy. "Reducing hazards of consumer laser pointer misuse". In: *International Laser Safety Conference 2019.1* (2019), p. 603.
- [88] L. Fu and Z. G. Hong. "Design of laser warning receiver based on DSP". In: *2009 Asia Pacific Conference on Postgraduate Research in Microelectronics Electronics (PrimeAsia)*. 2009, pp. 325–328.
- [89] Alastair D. McAulay. "Detecting modulated lasers in the battlefield and determining their direction". In: *Signal Processing, Sensor Fusion, and Target Recognition XVIII*. Ed. by Ivan Kadar. Vol. 7336. International Society for Optics and Photonics. SPIE, 2009, pp. 585–592. DOI: 10.1117/12.819423. URL: <https://doi.org/10.1117/12.819423>.
- [90] M. B. Sinclair and W. C. Sweatt. "Laser warning receiver to identify the wavelength and angle of arrival of incident laser light". In: (2010), Pat. 7,683,310 B1.
- [91] Y. Deng and D. Chu. "Coherence properties of different light sources and their effect on the image sharpness and speckle of holographic displays". In: *Sci Rep* 7.5893 (2017).
- [92] Duanni Huang et al. "High-power sub-kHz linewidth lasers fully integrated on silicon". In: *Optica* 6.6 (2019), pp. 745–752. DOI: 10.1364/OPTICA.6.000745.
- [93] David M. Benton. "A Proposed Method for a Photon-counting Laser Coherence Detection System to Complement Optical SETI". In: *Publications of the Astronomical Society of the Pacific* 131.1001 (2019), p. 074501. ISSN: 1538-3873. DOI: 10.1088/1538-3873/ab1a46.

- [94] D.M. Benton. "Laser detection using liquid crystal polarization modulators". In: *Optical Engineering* 59.6 (2020), pp. 1–9. DOI: 10.1117/1.0E.59.6.064106.
- [95] Virendra N. Mahajan. *Aberration Theory Made Simple Second Edition*. SPIE, 2011. Chap. Optical Aberrations, pp. 1–18.
- [96] R. R. Shannon and J.C. Wyant. *Applied optics and optical engineering*. Vol. 11. New York, USA: Academic Press Inc, 1992. Chap. Basic wavefront aberration theory for optical metrology.
- [97] Peter R. Hall. *Handbook of Optical Metrology Principles and Applications, Second Edition*. Ed. by T. Yoshizawa. Taylor & Francis Group, 2009. Chap. Lenses, Prisms, and Mirrors.
- [98] Virendra N. Mahajan. *Optical Imaging and Aberrations: Part I. Ray Geometrical Optics*. SPIE, 1998. Chap. Chapter 1: Gaussian Optics.
- [99] Virendra N. Mahajan. "Teaching of optical imaging and aberrations". In: *Fifteenth Conference on Education and Training in Optics and Photonics: ETOP 2019*. Vol. 11143. Society of Photo-Optical Instrumentation Engineers (SPIE) Conference Series. July 2019, 111430F, 111430F. DOI: 10.1117/12.2523698.
- [100] E. L. Dereniak and T.D. Dereniak. *Geometrical and Trigonometric Optics*. Cambridge University Press, 2008. Chap. Aberrations in optical systems, pp. 292–327. ISBN: 978-0-521-88746-5.
- [101] Daniel Malacara. In: *Optical Shop Testing*. John Wiley & Sons, Ltd, 2007. ISBN: 9780470135976. DOI: <https://doi.org/10.1002/9780470135976>. URL: <https://onlinelibrary.wiley.com/doi/abs/10.1002/9780470135976>.
- [102] H. Gross et al. *Handbook of Optical Systems, Volume 3: Aberration Theory and Correction of Optical Systems*. Wiley, 2007. ISBN: 9783527403790.
- [103] W.J. Smith. "Aberrations". In: *Modern optical engineering - 3rd edition*. McGraw-Hill, 2000. Chap. 3, pp. 61–90.
- [104] Virendra N. Mahajan. "Zernike Polynomials and Optical Aberrations". In: *Appl. Opt.* 34.34 (Dec. 1995), pp. 8060–8062. DOI: 10.1364/AO.34.008060. URL: <http://ao.osa.org/abstract.cfm?URI=ao-34-34-8060>.

- [105] Virendra N. Mahajan. "Orthonormal aberration polynomials for anamorphic optical imaging systems with rectangular pupils". In: *Appl. Opt.* 49.36 (Dec. 2010), pp. 6924–6929. DOI: 10.1364/AO.49.006924.
- [106] Vasudevan Lakshminarayanan and Andre Fleck. "Zernike polynomials: a guide". In: *Journal of Modern Optics* 58.18 (2011), pp. 1678–1678. DOI: 10.1080/09500340.2011.633763. eprint: <https://doi.org/10.1080/09500340.2011.633763>. URL: <https://doi.org/10.1080/09500340.2011.633763>.
- [107] V. N. Mahajan and G. Dai. "Orthonormal polynomials in wavefront analysis: analytical solution". In: *J. Opt. Soc. Am.* 24.9 (2007).
- [108] S. Deng et al. "Carbon Nanotube Array Based Binary Gabor Zone Plate Lenses". In: *Sci Rep* 7.15256 (2017). DOI: <https://doi.org/10.1038/s41598-017-15472-9>.
- [109] T. D. Beynon and R. M. R. Strange. "Computational study of diffraction patterns for near-field Fresnel and Gabor zone plates". In: *J. Opt. Soc. Am. A* 17.1 (Jan. 2000), pp. 101–106. DOI: 10.1364/JOSAA.17.000101.
- [110] David Attwood. *Soft X-Rays and Extreme Ultraviolet Radiation: Principles and Applications*. Cambridge University Press, 1999. DOI: 10.1017/CB09781139164429.
- [111] Milton Sussman. "Elementary Diffraction Theory of Zone Plates". In: *American Journal of Physics* 28.4 (1960), pp. 394–398. DOI: 10.1119/1.1935811.
- [112] Daniel J. Stigliani, Raj Mittra, and Richard G. Semonin. "Resolving Power of a Zone Plate*". In: *J. Opt. Soc. Am.* 57.5 (May 1967), pp. 610–613. DOI: 10.1364/JOSA.57.000610.
- [113] D. Williams, J. P. Kardach, and J. Posamentier. "Reconfigurable zone plate lens". Pat. US 7,420,737. 2005.
- [114] Melvin H. Horman. "Efficiencies of Zone Plates and Phase Zone Plates". In: *Appl. Opt.* 6.11 (Nov. 1967), pp. 2011–2013. DOI: 10.1364/AO.6.002011. URL: <http://ao.osa.org/abstract.cfm?URI=ao-6-11-2011>.
- [115] M. Young. "Zone Plates and Their Aberrations". In: *J. Opt. Soc. Am.* 62.8 (Aug. 1972), pp. 972–976. DOI: 10.1364/JOSA.62.000972.
- [116] Yu-Xuan Ren, Rong-De Lu, and Lei Gong. "Tailoring light with a digital micromirror device". In: *Annalen der Physik* 527.7-8 (2015), pp. 447–470. DOI: <https://doi.org/10.1002/andp.201500111>. eprint: <https://onlinelibrary.wiley.com/doi/pdf/10.1002/andp.201500111>.

- andp.201500111. URL: <https://onlinelibrary.wiley.com/doi/abs/10.1002/andp.201500111>.
- [117] *DLP Technology and Products*. URL: <https://www.ti.com/lit/ml/dlpb010e/dlpb010e.pdf>. (accessed: 31.05.2021).
- [118] Sergey Turtaev et al. "Comparison of nematic liquid-crystal and DMD based spatial light modulation in complex photonics". In: *Opt. Express* 25.24 (2017), pp. 29874–29884. DOI: 10.1364/OE.25.029874. URL: <http://www.opticsexpress.org/abstract.cfm?URI=oe-25-24-29874>.
- [119] *Spatial Light Modulators*. URL: <https://www.wavefrontshaping.net/tutorials>. (accessed: 31.05.2021).
- [120] Stirling Scholes et al. "Structured light with digital micromirror devices: a guide to best practice". In: *Optical Engineering* 59.4 (2019), pp. 1–12. DOI: 10.1117/1.0E.59.4.041202. URL: <https://doi.org/10.1117/1.0E.59.4.041202>.
- [121] Ufuk Ceyhan et al. "Inspection of aspherical lenses by wavefront analysis". In: *Optical Measurement Systems for Industrial Inspection VI*. Ed. by Peter H. Lehmann. Vol. 7389. International Society for Optics and Photonics. SPIE, 2009, pp. 1095–1105. DOI: 10.1117/12.834224.
- [122] D.M. Benton, S. Sugden, and M. Zandi. "Coherence imaging for laser detection". In: *Electro-Optical and Infrared Systems: Technology and Applications XVII*. Ed. by Duncan L. Hickman and Helge Bürsing. Vol. 11537. International Society for Optics and Photonics. SPIE, 2020, pp. 131–138. DOI: 10.1117/12.2573194.
- [123] Marek Dobosz and Mariusz Kożuchowski. "Overview of the laser-wavelength measurement methods". In: *Optics and Lasers in Engineering* 98 (2017), pp. 107–117. ISSN: 0143-8166. DOI: <https://doi.org/10.1016/j.optlaseng.2017.06.006>.
- [124] T. Saitoh et al. "Optical spectrum analyzer utilizing MEMS scanning mirror". In: *IEEE Photonics Technology Letters* 18.6 (2006), pp. 767–769. DOI: 10.1109/LPT.2006.871677.
- [125] *Collimated Laser Diode Module 405 nm, 4.5 mW, Elliptical Beam*. URL: https://www.thorlabs.com/_sd.cfm?fileName=QTN004380-S01.pdf&partNumber=CPS405. (accessed: 31.05.2021).

- [126] *Compact Laser Diode Module*. URL: https://www.thorlabs.com/_sd.cfm?fileName=22442-S01.pdf&partNumber=CPS532. (accessed: 31.05.2021).
- [127] S. H. Tao et al. "Sequence of focused optical vortices generated by a spiral fractal zone plate". In: *Applied Physics Letters* 89.3 (2006), p. 031105. DOI: 10.1063/1.2226995.
- [128] M.J. Simpson and A.G. Michette. "Imaging Properties of Modified Fresnel Zone Plates". In: *Optica Acta: International Journal of Optics* 31.4 (1984), pp. 403–413. DOI: 10.1080/713821522.
- [129] M. Khorasaninejad et al. "Achromatic Metalens over 60 nm Bandwidth in the Visible and Metalens with Reverse Chromatic Dispersion". In: *Nano Letters* 17.3 (2017), pp. 1819–1824. DOI: 10.1021/acs.nanolett.6b05137.
- [130] Maryam Mohagheghian and Saeed Ghavami Sabouri. "Multifocal binary diffraction lens with arbitrary focal lengths and number of foci". In: *Appl. Opt.* 58.27 (Sept. 2019), pp. 7531–7537. DOI: 10.1364/AO.58.007531. URL: <http://ao.osa.org/abstract.cfm?URI=ao-58-27-7531>.
- [131] *DLP Products Thermal Design Guide: Focus on High Power NIR Laser Illumination*. URL: https://www.ti.com/lit/an/dlpa104/dlpa104.pdf?ts=1622616529035&ref_url=https%253A%252F%252Fwww.ti.com%252Fproduct%252FDLP650LNIR. (accessed: 31.05.2021).
- [132] *Wavelength Transmittance Considerations for DLP DMD Window*. URL: https://www.ti.com/lit/an/dlpa031e/dlpa031e.pdf?ts=1622640204833&ref_url=https%253A%252F%252Fwww.google.com%252F. (accessed: 31.05.2021).